

UC Irvine

UC Irvine Electronic Theses and Dissertations

Title

BREAST DENSITY QUANTIFICATION USING STRUCTURED-LIGHT DIFFUSE OPTICAL TOMOGRAPHY

Permalink

<https://escholarship.org/uc/item/8qx3v6tv>

Author

Ruiz, Jessica

Publication Date

2016

Copyright Information

This work is made available under the terms of a Creative Commons Attribution License, available at <https://creativecommons.org/licenses/by/4.0/>

Peer reviewed|Thesis/dissertation

UNIVERSITY OF CALIFORNIA,
IRVINE

BREAST DENSITY QUANTIFICATION USING STRUCTURED-LIGHT DIFFUSE
OPTICAL TOMOGRAPHY

DISSERTATION

submitted in partial satisfaction of the requirements
for the degree of

DOCTOR OF PHILOSOPHY

in Biomedical Engineering

by

Jessica Ruiz

Dissertation Committee:
Professor Gultekin Gulsen, Co-Chair
Professor Lydia Min-Ying Su, Co-chair
Professor Jered Haun

2016

DEDICATION

To my family and friends
for their endless support and encouragement.

To Carlos,
my husband,
who inspired me to always do my best
and provided a constant stock of caffeinated drinks.

TABLE OF CONTENTS

LIST OF FIGURES	vi
LIST OF TABLES.....	xii
ACKNOWLEDGMENTS	xiii
CURRICULUM VITAE	xv
ABSTRACT OF THE DISSERTATION.....	xviii
Chapter One: Introduction	1
<i>1.1 Background and motivation</i>	<i>1</i>
1.1a. Anatomical Breast Density	2
1.1b. Functional Breast Density	2
<i>1.2 Current methods of measuring breast density</i>	<i>3</i>
1.2a. Qualitative assessment of mammographic density	3
1.2b. Quantitative measurements from mammograms	4
1.2c. Three-dimensional images and segmentation	5
1.2d. Measurement of background parenchymal enhancement (BPE).....	5
<i>1.3 Optical methods to image and quantify breast density.....</i>	<i>6</i>
1.3a. Current research in imaging and quantifying breast density using optical methods	8
<i>1.4 Structured-light based diffuse optical tomography.....</i>	<i>10</i>
1.4a. Measuring breast density with structured-light	11
<i>1.5 Innovations and contributions.....</i>	<i>13</i>
Chapter Two: Theoretical basis of diffuse optical tomography.....	15
<i>2.1 Photon interactions with biological tissue.....</i>	<i>15</i>
<i>2.2 Photon propagation model.....</i>	<i>19</i>
2.2a. Modeling Near-infrared Light Propagation in Biological Tissue	19
2.2b. Solving the photon diffusion equation.....	21
<i>2.3 Image reconstruction in diffuse optical tomography.....</i>	<i>23</i>
2.3a. Inverse problem	24
2.3b. Construction of the Jacobian sensitivity matrix.....	26
2.4b. Recovering chromophore concentrations.....	27
<i>2.4 Structured-light based DOT.....</i>	<i>28</i>
2.4a. Conversion of point sources to patterned sources.....	28
2.4b. Integration of the flux on detection side	29
Chapter Three: Measuring breast density using structured-light – simulation studies	31

3.1 <i>Simplistic geometry phantoms</i>	31
3.1a. Methods: Mesh creation	31
3.1b. Generation of synthetic measurements.....	32
3.1c. Image reconstruction and analysis	33
3.2c. Results.....	36
3.2 <i>Numerical breast phantoms</i>	38
3.2a. Methods: Building the numerical breast phantoms	39
3.2b. Methods: Simulation of SL-DOT measurements	40
3.2c. Methods: Image reconstruction and analysis.....	41
3.2d. Results	42
3.3 <i>Chromophore reconstruction and analysis</i>	45
3.3a. Methods: Breast numerical phantom generation.....	45
3.3b. Methods: Simulations.....	46
3.3c. Chromophore map analysis	47
3.3e. Results	49
Chapter 4: Benchtop instrumentation	58
4.1 <i>Initial setup: Source DMD & CCD camera</i>	58
4.1a. Laser Source Fiber	60
4.1b. CEL-5500 DMD	60
4.1c. CCD camera.....	61
4.2 <i>Final Setup: Source DMD & Detection DMD</i>	61
4.2a. Laser Source Fiber	63
4.2b. Source DMD.....	64
4.3c. Detector DMD and PMT	65
4.3 <i>Control software for the system</i>	69
4.3a. CELconductor Control Software	69
4.3b. DLP LightCrafter Control Software	70
4.4c. LabVIEW control software	71
Chapter five: Characterizing and optimizing the structured-light DOT system	74
5.1 <i>System stability and measurement reproducibility</i>	74
5.1a. Stability of measurements over time.....	74
5.1b. Reproducibility of measurements over time.....	76
5.2 <i>Signal levels and signal-to-noise ratio</i>	76
5.2a. Signal evaluation throughout system	77
5.2a. Number of samples to average	81
5.3 <i>Structured-light pattern optimization</i>	82
Chapter six: Phantom studies	86
6.1 <i>Agar phantoms creation</i>	86
6.1a. Creation of agar mixture	87
6.1b. NIR absorbing dyes.....	88
6.2 <i>Size-dependency of recovering inclusion volume and absorption coefficients</i>	90
6.2a. Phantoms.....	91

6.2b. Experimental setup, image reconstruction and analysis	92
6.2a. Results	93
<i>6.3 Size-dependency of multiple chromophores.....</i>	<i>97</i>
6.3a. Phantoms.....	97
6.3b. Experimental setup, image reconstruction and analysis	98
6.3c. Results.....	99
<i>6.4 Recovering contrast between the inclusion and background.....</i>	<i>101</i>
6.4a. Phantoms.....	101
6.4b. Experimental setup, image reconstruction and analysis	103
6.4c. Results.....	104
Chapter seven: Conclusions and future work	109
<i>7.1 Conclusions.....</i>	<i>109</i>
<i>7.2 Future Work.....</i>	<i>110</i>
References.....	113

LIST OF FIGURES

Chapter One: Introduction

1.1 Current methods of measuring breast density

Figure 1. The four different types of breast density BI-RADS categories as seen on mammograms. The images highlight the amount of bright, fibroglandular tissue found in high density cases. Reprinted from Mayo Clinic Proceedings, Vol 89 Issue 4, Wang, Amy, *et al.*, *Breast Density and Breast Cancer Risk: A Practical Review*, Page No 548-557. Copyright (2014), with permission from Elsevier. [8]..... 4

Figure 2. The four categories of background parenchymal enhancement (BPE) seen in contrast-enhanced MRI. The marked case shows the most intensity enhancement of the fibroglandular tissue within the breast. Reprinted from Radiology, Vol 260 Issue 1, King, Valencia, *et al.*, *Background Parenchymal Enhancement at Breast MR Imaging and Breast Cancer Risk*, Page No 50-60. Copyright (2011), with permission from RNSA. [14] 6

1.4 Structured-light based diffuse optical tomography

Figure 3. (a) Diagram of SLP-DOT for breast imaging. A laser is collimated onto an array of DMDs, which control and shine arbitrary patterns of light. Light travels through the breast, and is collected by another DMD, which integrates the signal according to a pattern and sends the light into a photomultiplier tube (PMT). Sample patterns are shown in (b) and (c), where white represents where light is illuminated or collected and black is un-projected or rejected signal..... 12

Chapter Two: Theoretical basis of diffuse optical tomography

2.1 Photon interactions with biological tissue

Figure 4. Illustration of photon interaction with biological tissue, where scattering changes the directions of the photons (indicated by arrows) and absorption extinguishes photons (indicated by star). Photons escaping the tissue on the same side of the source are reflected light and photons escaping on the opposite side of the source are transmitted light. 16

Figure 5. The absorption spectrum in the near-infrared spectral window are shown for water [66], lipid [67], oxy- and deoxyhemoglobin [68]..... 18

Chapter Three: Measuring breast density using structured-light – simulation studies

3.1 Simplistic geometry phantoms

Figure 6. (a) The pattern set used for the simulations of spherical inclusions. Patterns consist of vertical and horizontal stripes as well as checkerboards. The white area represents where light is illuminated or detected and the black area represents where light is neither illuminated nor detected. (b-d) Nodes of the FEM mesh with a 30mm diameter spherical inclusion (red). The black dots are the boundary nodes. The yellow circles outlined in red are the source ($x=1.67\text{mm}$) and detector ($x=60\text{mm}$) nodes. Shown are the source and detector pattern combinations (b) 2 & 4, (c) 6 & 5, and (d) 7 & 10. 33

Figure 7. Simulated measurements were performed on a phantom with homogeneous optical properties with the pattern set presented (a). Comparison of the different methods to

integrate the signal intensities on the detector side show that grid-based method performs the best, where the signals look smoother and symmetrical (b)..... 35

Figure 8. The real percent density of the spherical inclusions (blue) and the reconstructed percent volumes (red). With the exception of the 10mm diameter sphere case, the general trend of the segmented optical volumes increase as the sphere sizes increase, with more accurate results with larger objects..... 36

Figure 9. The central slice from the reconstructed 3D absorption maps for three different sphere sizes: (a) 10mm, (b) 30mm, and (c) 50mm diameter. The green contour outlined on each slice represents the segmentation at half-max of the recovered absorption values. n.. 37

Figure 10. The mean recovered absorption value also has a relationship with the true sphere size, where smaller objects have lower recovered absorption and larger objects have higher recovered absorption..... 38

3.2 Numerical breast phantoms

Figure 11. (a) Breast MR image is segmented to have the chest wall removed and is separated into a unilateral breast image. (b) The segmented breast MR slices separate the fibroglandular tissue from the breast volume. (c) Using the coordinates from the fibroglandular tissue geometries, the fibroglandular tissue was defined at specific nodes (red) with the FEM mesh. The green wiring represents the boundary elements. 40

Figure 12. Example of how the source (yellow circles) and detector (blue circles) nodes are placed onto the breast. The boundary of the breast is shown in green and the FGT is shown in red. Shown are source and detector pattern combinations (a) 7 & 10 and (b) 12 & 11.... 41

Figure 13. (a-c) The 3D segmentations of the reconstructed absorption maps for three different cases. The segmented optical volume is shown in the blue wireframe with the MRI-generated FGT geometries shown in red. (d) The correlation between the optical percent density and the MRI-based percent density for six cases are shown. The low density cases are above the line of unity (dashed line), showing that they are overestimated, while the higher density cases are underestimated. 43

Figure 14. (a) Highly dense breast case where SL pattern FOI does not cover the entire breast volume. (b) The segmented optical volume (24.12%, blue wireframe) is underestimated compared to the true FGT density (33.31%, red). 44

3.3 Chromophore reconstruction and analysis

Figure 15. (a-c) Central breast MR slices are shown for three cases of increasing density. (d-f) All of the MRI slices for each case are segmented to separate the FGT from the breast volume. (g-i) These FGT volumes are then used to build numerical breast phantoms within a rectangular FEM mesh..... 46

Figure 16. The relationship between both %Volumes and MRI %BD are shown. Water volumes (blue squares, $r=0.89$, dashed-line) and lipid volumes (green circles, $r=0.85$, solid-line) both show correlation with the MRI %BD..... 50

Figure 17. The absolute error between %Vol_{water} and MRI %BD is shown. The horizontal line marks 0, or no, error. Cases above this line are overestimated while cases below this line are underestimated. Discrimination between centralized (blue squares) and intermingled (red triangles) FGT morphologies show that the most overestimated cases are the intermingled 51

Figure 18. (a-c) Three breast MRI cases of different densities and tissue morphologies are presented. (d-f) The reconstructed water maps are shown, where the green outline shows the MRI-generated FGT while the white dashed-line shows the contour of the %V_{water} segmentation. (g-h) The lipid maps are also presented, where the black solid line is the FGT and the blue dashed-line is the %V_{lipid} segmentation contour. 52

Figure 19. The mean water (blue) and lipid (green) concentrations within the segmented volume for each MRI case is shown. The plot shows that there is a dependency of the recovered chromophore concentrations on the MRI breast density, where high density cases have higher and lower recovered water and lipid, respectively. Lower density cases have higher recovered lipid and lower water concentrations. 54

Figure 20. The estimated breast densities from the regression model that uses the $\%V_{water}$ and C_{water} values show high correlation with the MRI %BD..... 55

Figure 21. The modified regression model that uses parameters from both water and lipid maps to estimate the %BD shows good agreement with the MRI %BD ($r=0.97$). 56

Figure 22. The absolute error between the estimated %BD and the MRI %BD is shown. The horizontal line marks 0, or no, error. The error for all the cases has been reduced compared the first approach and are all well distributed along this line for all the MRI %BDs..... 57

Chapter Four: Benchtop Instrumentation

4.1 Initial setup: Source DMD & CCD camera

Figure 23. First preliminary setup of the SL-DOT system. A DMD projector coupled with a fiber laser source (a) projects light onto an agar phantom (b) and a CCD camera (c) collected images of the other side..... 59

Figure 24. Schematic of the preliminary benchtop system. A computer controls which patterns the DMD projects and the settings of the camera. Images are collected when prompted through the computer. 59

Figure 25. CEL-5500 DMD projector used to spatially modulate the light source into structured-light patterns..... 60

Figure 26. PerkinElmer ColdBlue™ CCD camera. Filter wheel was not used..... 61

4.2 Final Setup: Source DMD & Detection DMD

Figure 27. The final benchtop SL-DOT setup. (a) A source DMD coupled with a light source projects SL patterns onto (b) an agar phantom and (c) a second DMD with a PMT collects measurements from the other side..... 62

Figure 28. Schematic of the final benchtop system. The source DMD sends light towards a phantom and a detection DMD integrates the signal into a PMT. The current output of the PMT is measured by a transimpedance amplifier that is then measured by a data acquisition card (DAQ) and the computer. The computer controls the DMDs' patterns and controls the sensitivity of the PMT through the DAQ..... 63

Figure 29. (a-1)The new DMD projector that is coupled with (a-2) a laser fiber source. Looking at (b) the opened projector, (b-1) a light source sends light towards a mirror and lens, which then illuminates (b-2) the DMD. The DMD then controls which pixels are projected, and sends the projected SL-pattern towards (b-3) the imaging lens. (c) A close-up of the DMD behind the lens is also shown..... 65

Figure 30. A view of the opened DMD system used for light collection is presented. Light from the agar phantom is collected with (1) the large imaging lens on the bottom left, the image of which is sent towards (2) a prism. Based on the angle of incidence, the prism reflects light towards (3) the DMD, where pixels are used to create the structured-light. The DMD reflects light back towards and passes through the prism, and is send towards (4) a mirror, which reflects the light towards (5) a focusing lens and to (6) the PMT. 66

Figure 31. The DMD system used to collect light and images. (a) The red laser light overlay over the image is used to determine where the field of view of the DMD is. Image used for example is shown in lower-right corner of (a). (b) A camera takes an image of the plane where

the PMT is positioned (red-dashed line, a). (c) A magnified image shows that the entire FOV can be seen. Please note that the image is reversed due to the lens system, but this is insignificant because all of the signal will be integrated into the PMT. (d-f) Another SL-pattern is demonstrated where only the DMD only reflects part of the image according to the pattern. 68

4.3 Control software for the system

Figure 32. CELconductor Control Software from DLInnovations to control the CEL-5500 DMD system. Software can be used to manually select patterns or store pattern sequences that can be externally triggered. 70
 Figure 33. DLP LightCrafter Control Software from Texas Instruments is used to control the DLP-3000 DMD system. The software allows for patterns to be manually selected or can store pattern sequences that can be controlled externally through voltage triggering. 71
 Figure 34. Graphical user interface created in LabVIEW to control the SL-DOT system. Parameters that are inputted include the voltage to apply to the PMT, the number of source and detector patterns, the number of samples to be averaged, and the sampling rate of the DAQ card. 72
 Figure 35. An overview of the LabVIEW code behind the GUI..... 73

Chapter Five: Characterizing and optimizing the structured-light DOT system

5.1 System stability and measurement reproducibility

Figure 36. (a) Single intensity measurements taken every minute and (b) every five minutes to test the system’s stability over time. The mean of the measurements taken every minute is $0.9083\mu\text{A}$ with a standard deviation of $0.0077\mu\text{A}$. The mean of the measurements taken every five minutes is $0.9199\mu\text{A}$ with a standard deviation of $0.0035\mu\text{A}$. In both cases, the standard deviation is less than 1% of the mean, which is acceptable for our imaging studies..... 75
 Figure 37. Scatter plot of the 144 measurement set at $t = 0\text{min}$ and $t = 240\text{min}$ to visualize the correlation between the two. ICC analysis yielded a $r = 0.9799$ with a $p \ll 0.01$ for this particular pair-wise comparison..... 76

5.2 Signal levels and signal-to-noise ratio

Figure 38. Illustration of points of power loss throughout system. Beginning from the initial laser fiber power (a), 0.128 of the fiber power is transmitted through the source DMD (b). Based on a simulation with a 53mm thick phantom (c), the detected flux is 5×10^{-4} of the incident light. This light then goes through another drop in power while being collected by the detector DMD (d), where only 0.262 of the collected light reaches the PMT (e)..... 78
 Figure 39. The loss of power in a traditional contact DOT transmission-mode point source (a) and point detector (c) is illustrated. The main loss of photons is from the phantom (b). 78
 Figure 40. Illustration of points of power loss throughout system using smaller SL patterns. Beginning from the initial laser fiber power (a), 0.026 of the fiber power is transmitted through the source DMD (b). Based on a simulation with a 53mm thick phantom (c), the detected flux is 4.59×10^{-5} of the incident light. This light then goes through another drop in power while being collected by the detector DMD (d), where only 0.052 of the collected light reaches the PMT (e)..... 81
 Figure 41. (a) The signal (blue) and noise (red) levels and (b) the SNR of measurements collected with a different number of averaged samples. Measurements were taken on a solid

epoxy phantom with 560V applied to the phantom, with corresponds to a PMT dark current of 0.16nA. 82

5.3 Structured-light pattern optimization

Figure 42. Reconstructions (b, d) from using (a) pattern set # 1 and (c) pattern set # 2 as SL-patterns to collect measurements from a phantom with an inclusion that is 10% of the phantom’s volume. The red wireframe represents the reconstructed volume segmented at half-max and the blue isosurface represents the inclusion..... 83

Figure 43. Absorption map slice that was reconstructed from measurements using pattern set # 1. Slice is positioned at 5mm before the detection surface. The areas of high absorption match the appearance of the last pattern in pattern set # 1. 84

Chapter Six: Phantom studies

6.1 Agar phantoms creation

Figure 44. (a) An agar phantom with enclosed inclusions is made through layering the agar mixture into a mold. (b) A bottom layer in gray is allowed to solidify and (c) the inclusion (red) is centered on top. (d) Agar is then poured on top (gray) of the inclusion to encase it in the center. 88

Figure 45. Absorption spectrum of two dyes, NIR782E and NIR869A, in the near infrared region. Their isobestic point (where the absorption is the same for both dyes) is 801nm.... 89

Figure 46. Decay of the NIR782E (blue) and NIR869A (red) dyes over 6 days. Day 0 is the day the aqueous dye solution was created. Absorption measurements are taken at each dye’s peak absorption (782nm and 869nm, respectively) and normalized to Day 0’s measurement. 90

6.2 Size-dependency of recovering inclusion volume and absorption coefficients

Figure 47. Illustration of different inclusion sizes (1, 5, 10% by volume) within the 53x77x77mm³ agar phantom. 91

Figure 48. SL pattern set used for the illumination and detection of light from the phantom, forming 100 unique measurements. 92

Figure 49. SL-DOT measurements from the homogeneous (blue), 1% (yellow), 5% (green), and 10% (red) phantoms using pattern set shown in Figure 46..... 94

Figure 50. (a) Slices of the reconstructed absorption map for the 10% volume inclusion phantom are presented at x = 10, 20, 30, 40mm in depth. (b) A volume (red) is segmented at half-maximum of the recovered absorption range to represent the recovered inclusion..... 94

Figure 51. (a) The center slice of the image reconstruction for each phantom is presented in the top row. As the inclusion size increases, the higher the absorption is recovered. (b) The bottom row represents the 3D representation of the reconstructed volume. The red wireframe represents the contour of the volume segmented at half-max, V_{abs} , and the solid blue object represents the inclusion..... 95

6.3 Size-dependency of multiple chromophores

Figure 52. The center slice of the reconstructed dye (D1 and D2) concentrations are shown for phantoms with 5% and 10% inclusion sizes. The larger the inclusion, the more contrast between the inclusion and background is seen. 100

6.4 Recovering contrast between the inclusion and background

Figure 53. The geometry of the heterogeneous phantoms for this study. The background surrounds an inclusion that is 10% of the phantom's volume. The inclusions P1, P2, and P3 denote the specific dye concentrations used. 102

Figure 54. Center slices of the recovered dye (D1 & D2) concentrations for each phantom (P1, P2, & P3). 105

Figure 55. The dye contrast between the inclusion and background is shown for (a) D1 and (b) D2. The contrast for each phantom is calculated as the mean dye concentration of the inclusion divided by the concentration in the background. The contrast from simulated data is shown in red and the contrast from the experimental data is shown in green. 106

LIST OF TABLES

Chapter Three: Measuring breast density using structured-light – simulation studies

3.3 Chromophore reconstruction and analysis

Table 1. Concentrations of water, lipid, oxy- and deoxyhemoglobin chromophores chosen for both adipose and fibroglandular tissues.....	47
Table 2. Absorption coefficients for both adipose and fibroglandular tissue at five wavelengths. Absorption values were calculated from proposed chromophore concentrations from Table 2 using equation (3).....	47
Table 3. The parameters of the three cases presented in Figure 18.	52

Chapter Six: Phantom studies

6.2 Size-dependency of recovering inclusion volume and absorption coefficients

Table 4. Dimensions of the inclusions used in the phantoms.	91
Table 5. Optical properties of agar used for different inclusion sizes experiment. Values are given for 808nm.	92
Table 6. The recovered inclusion volume and mean absorption for each phantom.....	96

6.3 Size-dependency of multiple chromophores

Table 7. D1 and D2 concentrations used in both the background and inclusion.....	98
Table 8. The optical properties of the background and inclusion at 660, 785, 808 and 830nm.	98
Table 9. The recovered contrast between the inclusion and the background for both D1 and D2.	100

6.4 Recovering contrast between the inclusion and background

Table 10. The concentrations of NIR782E (D1) and NIR869A (D2) added to each agar mixture to form the phantoms.	102
Table 11. The dye concentrations inside the inclusions normalized to the background. This highlights the concentration contrast between the background and each inclusion.....	102
Table 12. Optical properties of the background and inclusions calculated at each wavelength.	103
Table 13. The recovered dye contrast between the inclusion and background for each phantom (P1, P2, & P3).....	105

ACKNOWLEDGMENTS

I am very thankful for the past four years that I have spent working at the Center for Functional Onco-Imaging. I feel extremely blessed that I was able to meet and work with so many wonderful, kind and brilliant people. Without their help, this dissertation would not have been possible.

Firstly, I would like to express my sincere gratitude to my advisors, Professor Gultekin Gulsen and Professor Min-Ying Lydia Su, both of whom are the kindest and most understanding advisors I could have hoped to work with. Over the past few years, it has been an amazing journey working on and developing my dissertation. From Dr. Gulsen's creativity and imaging expertise to Prof. Su's practicality and clinical insight, it has been a truly wonderful experience learning from them. Without their advice and persistent help, this dissertation would have not been possible.

I offer my humble appreciations to Dr. Farouk Nouizi, whose brilliant expertise has helped me tremendously in understanding diffuse optical tomography. He not only thoroughly explained a lot of the fundamental theory to me, but also found a way to explain it with creative examples. I am also grateful for his advice on navigating through the world of academia, which has helped me so much during my graduate studies.

I would also like to thank Dr. Jeon-hor Gordon Chen, whose experience as a radiologist was very insightful. With his help and advice, I began thinking of the dissertation not only from an engineering standpoint, but also from the patient's perspective. I also really appreciate his amusing anecdotes, most of which has helped guided me through my graduate career.

Additionally, I offer my deepest gratitude to Jaedu Cho, who has always amazed me with his knowledge of almost everything that I have asked him. Although I had a lack of experience with building hardware, I was able to build my first optical instrument thanks to his guidance. I also learned a lot of practical skills from him, most notably the *correct* way to solder.

I also want to thank Professor Jered Haun, for not only serving on my committee, but also for his advice and guidance. Additionally, I want to thank Prof. Bruce Tromberg and Prof. Yizhi Sun. They have all given me many things to consider about this project and have influenced its development.

Many thanks goes to Yifan Li, who worked very hard and tediously in segmenting the breast MR cases which are used in this dissertation. It was great sharing an office with her, and I have missed her since her graduation.

I also owe my thanks to numerous labmates that I have. Alex Luk and my unrelated "Kwong cousin" Tiffany Kwong have both made my graduate life experience much more fun when we were not diligently working. When we were in lab, they have

helped me so much even though I only meant to ramble about problems with my project. My labmate Jie Zheng entered the graduate program at the same time as I did, so we tackled a lot of the program requirements together. I greatly appreciate the team effort to pass our preliminary exam with our weekly study sessions (who also included fellow classmates Rachel Qu, Jessica Hsieh, Emon Heidari and Xiaolong Qiu); we all successfully passed our exams and the first milestone in the program. I would also like to thank Dr. Hakan Erkol, whose sense of humor and friendliness always brightened my day. Lastly, I want to thank the newcomers to our lab: Yang Zhang and Michael Marks, both of whom made a great new and fun addition to the lab.

I am grateful for the support that I have received from the Biophotonics across Energy Space and Time (BEST) IGERT program. They have not only provided me with financial aid, but also prepared great learning experiences through the workshops and courses they offered.

Lastly, I thank the Radiological Society of North America and Elsevier for permission to include copyrighted images that are featured in Chapter One of my thesis.

CURRICULUM VITAE

Jessica (née Kwong) Ruiz

Education

- 2010 B.E. in Biomedical Engineering, Stony Brook University
Stony Brook, New York
- 2011 M.S. in Biomedical Engineering, Stony Brook University
Stony Brook, New York
- 2016 Ph.D. in Biomedical Engineering, University of California, Irvine
Irvine, California

Honors and Awards

- 2006-2010 Women in Science and Engineering (WISE) Program
Stony Brook University
- 2013 Competitive Edge Summer Research Program
University of California, Irvine
- 2014 Association of Graduate Students (AGS) Travel Grant
University of California, Irvine
- 2014-2016 Biophotonics across Energy, Space and Time (BEST) IGERT
Traineeship
University of California, Irvine
- 2015 Newport Research Excellence Travel Award
SPIE Photonics West

Publications

Kwong, J., Nouizi, F., Cho, J., Zheng, J., Li, Y., Chen, J-H., Su, M-Y., Gulsen, G. (2016). Breast density quantification using structured-light based diffuse optical tomography simulations. *Applied Optics*. (*in review*)

Chen, J-H., Chan, S., Li, S., Chang, R., Yeh, D-C., Chang, R-F., Yeh, L-R., **Kwong, J.**, Su, M-Y. (2016) Evaluation of the association between quantitative mammography breast density and breast cancer occurred in different quadrants. *BMC Cancer*. (*in review*)

Conference Proceedings

Kwong, J., Nouizi, F., Li, Y., Chen, J., Su, M-Y., Gulsen, G. (2014). Simulation of optical breast density measurements using structured light illumination. Proc. SPIE, 8937, Multimodal Biomedical Imaging IX, 893717. <http://doi:10.1117/12.2058092>

Kwong, J., Nouizi, F., Cho, J., Zheng, J., Li, Y., Chen, J., Su, M-Y., Gulsen, G. (2015). Diffuse optical imaging of the breast using structured-light. Proc. SPIE 9319, Optical Tomography and Spectroscopy of Tissue XI, 93190K. <http://doi.org/10.1117/12.2079805>

Zheng, J., Nouizi, F., Cho, J., **Kwong, J.**, Gulsen, G. (2015). High resolution 3D fluorescence tomography using ballistic photons. Proc. SPIE 9319, Optical Tomography and Spectroscopy of Tissue XI, 93191V. <http://doi:10.1117/12.2077748>

Nouizi, F., Kwong, T.C., **Kwong, J.**, Cho, J., Chan, Y., Sampathkumaran, U., Zhu, Y., Alam, M.M., Gulsen, G. (2015). Proc. SPIE 9319, Optical Tomography and Spectroscopy of Tissue XI, 93190Y. <http://doi:10.1117/12.2080630>

Kwong, J., Nouizi, F., Cho, J., Zheng, J., Li, Y., Chen, J., Su, M-Y., Gulsen, G. (2016). Diffuse optical tomography with structured-light patterns to quantify breast density. Proc. SPIE 9689, Photonic Therapeutics and Diagnostics XII, 968942. <http://doi:10.1117/12.2213742>

Presentations

- | | |
|------|---|
| 2013 | Competitive Edge Summer Research Symposium
University of California, Irvine
“Simulating Temperature Changes for a Treatment Planning Tool based on Patient Magnetic Resonance Images” (oral) |
| 2014 | SPIE Photonics West BiOS conference
San Francisco, California
“Simulation of optical breast density measurements using structured light illumination” (poster) |
| 2014 | ISMRM-ESMRMB Meeting
Milan, Italy
“Simulation of Optical Breast Density Measurements Using Structured Light Illumination in A Patient-Specific Anatomical Breast Model Built from 3D MRI-Segmented Breast Density” (e-poster) |

- 2015 SPIE Photonics West BiOS conference
San Francisco, California
“Diffuse optical imaging of the breast using structured-light” (oral)
- 2016 SPIE Photonics West BiOS conference
San Francisco, California
“Diffuse optical tomography with structured-light patterns to quantify breast density” (oral)

ABSTRACT OF THE DISSERTATION

BREAST DENSITY QUANTIFICATION USING STRUCTURED-LIGHT DIFFUSE OPTICAL TOMOGRAPHY

By

Jessica Ruiz

Doctor of Philosophy in Biomedical Engineering

University of California, Irvine, 2016

Professor Gultekin Gulsen & Professor Lydia Min-Ying Su, Co-Chairs

Anatomical breast density is an independent risk factor for breast cancer, where women with larger amounts of dense fibroglandular tissue (FGT) are more likely to develop breast cancer. Clinical models that consider personal information about a woman (age, family history, and genetics) to predict her risk for breast cancer can help her customize their own screening options or consider preventative measures. Although magnetic resonance imaging (MRI) can be used to quantitatively measure the FGT volume, its high-cost makes it impractical to implement. Optical methods provide an appealing alternative, where the systems are low-cost and easily compactable, which makes clinical implementation easier. Optical tomography can spatially resolve and measure the concentration of relevant chromophores within the breast: water, lipid, oxy and deoxyhemoglobin. We have investigated the use of structured-light diffuse optical tomography (SL-DOT) in imaging the breast volume. In SL-DOT, spatially modulated light is illuminated and collected from the breast through the use of two digital micro-mirror devices (DMDs). Through both

simulations and phantom studies, we found that SL-DOT is suitable for predicting the percentage of FGT when taking into consideration both the volume segmented from the chromophore maps and the recovered chromophore concentrations. A second independent risk factor in which we are interested is the *functional breast density*. After intravenous injection of a MRI contrast agent, the intensity of the FGT is enhanced to varying degrees among patients, referred to as background parenchymal enhancement (BPE). It has been shown that BPE is also correlated with breast cancer incidence, most likely due to the higher perfusion of nutrients in blood to the FGT. Because BPE is an indication of blood flow, we believe the hemoglobin content measured from SL-DOT will be correlated to the BPE seen in MRI; therefore, our technique can potentially measure two independent risk factors for breast cancer. Once clinically translated, SL-DOT can be used to measure both the anatomical and functional breast density inexpensively and quickly, allowing women to make informed decisions about their breast cancer screening.

Chapter One: Introduction

1.1 Background and motivation

Breast cancer is the second leading cause of cancer-related deaths in women in the United States, with an estimated 247,000 new cases in 2016 according to the American Cancer Society [1]. Diagnosis of breast cancer in its earlier stages improves survival outcomes, emphasizing the importance of routine and appropriate breast cancer screening protocols for women. In 2009, the U.S. Preventive Services Task Force revised the mammography screening guidelines, recommending exams after the age of 50 every two years [2,3]. For women ages 40-49, it becomes a gray area where the decision to start screening for breast cancer becomes lies with the patient. The American Cancer Society has criticized this guideline change, with many professionals arguing that despite the lower incidence of cancer in this age group, delayed diagnosis and treatment will lead to a worse prognosis and outcome [4]. A recent development in the medical community is “risk-based screening,” where models can calculate a woman’s lifetime risk and recommend the appropriate screening method and frequency for her. This is extremely important as resources can be spent on high-risk women for the diagnosis of cancer at an early, curable stage or for preventive strategies. For example, the American Cancer Society recommends for women with a lifetime risk greater than 20-25% to undergo annual breast magnetic resonance (MR) screenings because the cost per quality-adjusted life year saved outweighs the cost of MR screening [5]. Meanwhile, false-positive findings, unnecessary procedures and anxiety for low-risk women can be avoided. Known risk

factors that have been already incorporated into the models included age, family history, hormonal/reproductive factors, and BRCA genetic mutation.

1.1a. Anatomical Breast Density

Breast density is another risk factor that has been heavily investigated in the past few decades. It refers to the amount of stromal and epithelial tissue, collectively known as fibroglandular tissue (FGT), within the breast volume. Several studies have found increased breast cancer risk associated with highest breast densities when compared to the lowest densities [6–8]. Unlike the other risk factors, breast density can be reduced through hormonal intervention and can be used as a preventative measure in particularly high-risk women [9]. Currently, qualitative assessment of breast density seen on mammograms is incorporated into only one risk model, the Breast Cancer Surveillance Consortium (BCSC) [10]. Expanding upon this, the Breast Cancer Prevention Collaborative Group has suggested that quantitative breast density should be incorporated into risk models to improve their accuracy. In mammography, the FGT attenuates the x-rays more than the surrounding adipose tissue, forming the image contrast. Mammographic density (MD) refers to the amount of bright FGT seen on the mammogram and it has been discovered that higher MD not only obscures tumors and lower specificity [11], but also correlates to a higher risk of breast cancer.

1.1b. Functional Breast Density

Another independent risk factor for developing breast cancer can be seen in contrast-enhanced magnetic resonance imaging (MRI). A contrast agent, such as

gadolinium, is intravenously injected into the patient, where it travels to the heart and is pumped throughout the body. During this time, images over a short amount of time are acquired. Due to the enhanced permeability and retention (EPR) effect, the gadolinium tends to localize and accumulate in tumors with leaky blood vessels [12]. The high intensity within the tumor is compared to the pre-injection images, and this difference is referred to as the contrast enhancement. While this technique has been used to determine the blood perfusion of a tumor and its malignancy [13], it has been observed that FGT also becomes enhanced to a lesser degree [14,15]. This is referred to as the background parenchymal enhancement (BPE). The BPE among different patients vary from a slight or mild enhancement to a large or marked enhancement [14]. Several studies have found that a marked increase in the BPE of the dense tissue observed after injection of the MRI contrast agent was associated with a higher risk of cancer [14,15]; because it involves blood perfusion, it can be considered as the *functional breast density*. This suggests that blood supply (*i.e.* hemoglobin content) may be a marker that can also be used for risk assessment. Although MRI is a rich source of information for risk assessment in terms of anatomical and functional breast density, as previously mentioned, its high-cost makes its wide-spread use impractical.

1.2 Current methods of measuring breast density

1.2a. Qualitative assessment of mammographic density

The relationship between breast density and breast cancer was first reported in 1967 by John Wolfe [16]. A decade later, Wolfe described a higher incidence of

breast cancer in high-risk patients that were stratified into four risk groups based on the amount of fibroglandular tissue seen on their mammograms [17]. Since then, categorizing mammograms into four categories (I-IV) became a standard known as the Breast Imaging Reporting and Data System (BI-RADS) for breast density (Figure 1). Trained radiologists assess and score each mammogram into quartiles; however, inter-operative variability in the scoring was found to be an issue [7]. This motivates the development of methods and algorithms to quantify breast density.

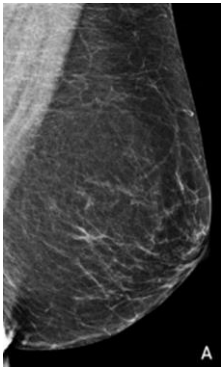
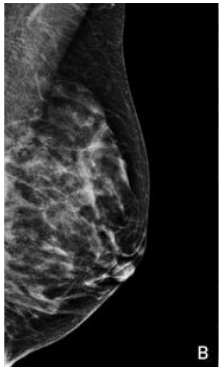
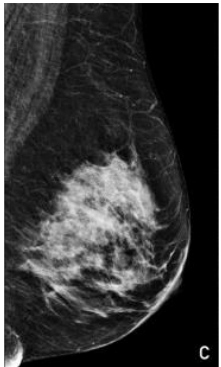
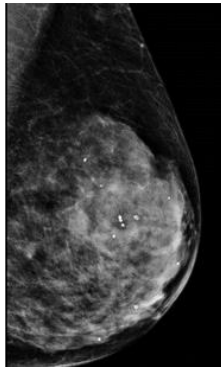
BI-RADS category	I	II	III	IV
Visual description	Almost entirely fatty	Scattered fibroglandular densities	Heterogeneously dense	Extremely dense
Examples				

Figure 1. The four different types of breast density BI-RADS categories as seen on mammograms. The images highlight the amount of bright, fibroglandular tissue found in high density cases. Reprinted from Mayo Clinic Proceedings, Vol 89 Issue 4, Wang, Amy, *et al.*, *Breast Density and Breast Cancer Risk: A Practical Review*, Page No 548-557. Copyright (2014), with permission from Elsevier. [8]

1.2b. Quantitative measurements from mammograms

The current methods to quantify breast density aim to measure the breast and fibroglandular tissue volumes. In addition, the percentage of FGT within the breast, known as the percent breast density (%BD), can be also calculated and reported. As

mammography is a popular imaging modality for breast cancer screening, several software programs have been developed to interpolate the volumes based on the 2D mammogram. VolparaDensity™ and Quantra™ are commercially available FDA-approved software packages for measuring volumetric density [18]. However, when compared to MRI, a 3D imaging modality, Volpara™ and Quantra™ underestimated the %BDs measured by MRI, due to inaccuracies in calculating the breast volume [19]. Additionally, breast density calculations based on mammograms requires women to have already undergone screening mammography; younger women interested in their lifetime risk will most likely have not done this yet.

1.2c. Three-dimensional images and segmentation

The use of MRI or computed tomography (CT) can provide accurate volumetric measurements due to the 3D nature of these imaging modalities. In previous work, segmentation algorithms on MR images defines the FGT and breast volume, which can be used to calculate the %BD (*anatomical breast density*) [20,21]. Although MRI is considered the gold standard for accurately measuring %BD, its high cost prevents its implementation as a simple, widespread risk assessment tool. Furthermore, the use of ionizing radiation in CT may not make it ideal for simple, routine risk assessment.

1.2d. Measurement of background parenchymal enhancement (BPE)

Like the quartile BI-RADS system for breast density, BPE can be assessed into four categories: minimal, mild, moderate and marked (Figure 2) [14]. As seen with the BI-RADS categorization, the qualitative assessment of BPE can also be subject to

discrepancies among raters. As an alternative, image analysis techniques can be applied to quantify the enhancement of the FGT. One method based on the segmentation of the FGT from the breast volume. MRI images are taken before and after the injection of the contrast agent into the patient. The percentage increase of the enhanced signal within the segmented tissue over the non-enhanced signals prior to injection can be calculated, referred to as the BPE [22]. This analysis can be further expanded by calculating the percentage of voxels within the FGT that is above the mean of the previously calculated BPE over the total number of voxels in the FGT, known as %BPE [23]. More studies on the link between breast cancer risk and BPE can elucidate which parameters are a better predictor for developing breast cancer.

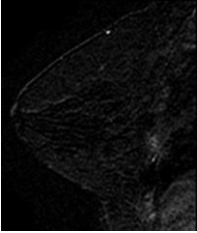
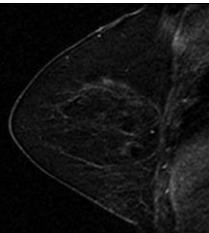
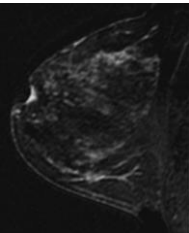
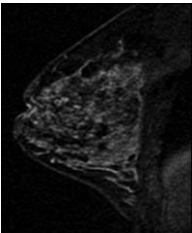
BPE description	Minimal	Mild	Moderate	Marked
Examples				

Figure 2. The four categories of background parenchymal enhancement (BPE) seen in contrast-enhanced MRI. The marked case shows the most intensity enhancement of the fibroglandular tissue within the breast. Reprinted from Radiology, Vol 260 Issue 1, King, Valencia, *et al.*, *Background Parenchymal Enhancement at Breast MR Imaging and Breast Cancer Risk*, Page No 50-60. Copyright (2011), with permission from RNSA. [14]

1.3 Optical methods to image and quantify breast density

Given the advantages and disadvantages of mammography and MRI to measure breast density, there is an opportunity for optical imaging to provide an inexpensive and safe alternative without non-ionizing radiation. Optical methods use a near-infrared (NIR) laser source to illuminate tissue, where photons in the NIR

spectral window, 600-1000nm wavelength range, can propagate through biological tissue on the order of several centimeters [24,25]. A photodetector can be placed on the opposite side of the tissue to collect transmitted photons, known as transmission mode [26,27]. Conversely, the detector can be placed on the same side of the tissue as the source to collect reflected photons, known as reflection mode [28–30]. These traveling photons may undergo absorption by a molecule or scattering, a change in the direction of the traveling photon. These events contribute to the light attenuation and phase delay of an intensity modulated signal, where absorption mainly affects intensity measurements and scattering mainly affects phase measurements. It is important to note that in order to extract scattering information, sinusoidal intensity modulation of the source (frequency-domain) or analysis of the temporal profile of arriving photons at the detector from a short-pulse of light (time-domain) techniques are necessary to obtain phase or photon time-of-flight measurements. In the simplest method of optical imaging, steady-state laser sources (continuous-wave) are used and only the light intensity attenuation is measured. With this method, scattering and absorption is difficult to separate; however studies have shown it is possible to minimize the cross-talk between absorption and scattering [31].

Absorption and scattering are important because of the underlying biological significance of these properties. Absorption is directly related to the molecular constituents of the tissue, where light-absorbing molecules called chromophores provide contrast between the adipose and FGT. Scattering is related to the size and density of these molecules, where FGT has been found to be highly scattering compared to adipose tissue [32–34]. By measuring these properties, several research

groups have been able to distinguish between adipose and FGT, as well as assess a patient's risk for breast cancer [34–40].

1.3a. Current research in imaging and quantifying breast density using optical methods

A research group from Politecnico di Milano in Italy uses a seven-wavelength time-domain optical mammography system to collect data in transmission mode along multiple points of the breast to investigate bulk concentrations of water, lipid, hemoglobin and collagen, as well as reduced scattering maps [41]. From the information they collect with their system, they have built a logistic regression model to determine a woman's BI-RADS IV breast density category based on her collagen content and scattering parameters [34]. Their recent work has found that the four different BI-RADS categories can be determined based on a collagen index they formulated as $CI = b[\text{Collagen}]$, where $[\text{Collagen}]$ refers to the concentration of collagen and b is the fitted scattering slope as a function of wavelength [42].

A group from the University of Toronto has developed their Transillumination Breast Spectroscopy system to categorize breasts into a BI-RADS rating. They use a broadband source coupled into a fiber to deliver continuous-wave (CW) light at a point along the breast and collect light with another fiber coupled into a spectrophotometer. They acquire spectral data from 550 to 1300nm and perform principle component analysis (PCA) with a training set to determine which spectra is accountable for the most variation in the data [43]. Based on these spectra and their weighting, also known as scores, they determine which breast cases are low, medium and high densities [43]. The group went further and used the spectra to estimate the

quantitative percent density and compared their predictions to the mammographic densities calculated by Cumulus, with good correlation [44].

The research group at Dartmouth College has used their diffuse optical spectroscopic tomography system with frequency-domain (FD) and CW measurements to quantify the chromophore concentrations within both the fibroglandular tissue and adipose tissue. Their recent system uses a set of point sources and detectors integrated into a breast MRI coil to collect optical data and MR images. They perform diffuse optical tomographic (DOT) image reconstruction constrained with anatomical information provided by MRI in order to improve the spatial resolution of DOT. They found differences in water, hemoglobin and scattering parameters between these two tissue types [38].

Lastly, the work at the Beckman Laser Institute (BLI) uses diffuse optical imaging to image and quantify the chromophore concentrations within healthy breast tissue to understand tissue composition. Their work using their frequency-domain photon migration (FDPM) technique with a hand-held probe measured water, hemoglobin and lipid content from hormone replacement therapy patients, pre- and postmenopausal women [45,46]. Their hand-held probe performs in reflection mode, allowing them to obtain superficial spectral data from the breast. The use of FD measurements at several wavelengths allows the determination of absorption and scattering, and subsequently chromophore quantification. Their results consistently showed that postmenopausal breasts had lower water and hemoglobin content, as well as higher adipose content, due to the loss of fibroglandular tissue after menopause [45,46]. The inclusion of a broadband light for CW measurements to the

FDPM instrument led to the development of their Diffuse Optical Spectroscopic Imaging (DOSI) system that can provide both absorption and scattering spectra (from 650-1000nm) at each measurement point [24]. With this information, they found differences between water and hemoglobin levels among the different BI-RADS groups [40]. They found that the use of an index, called the tissue optical index (TOI) as defined by $\frac{[\text{water}] \cdot [\text{deoxyhemoglobin}]}{[\text{lipid}]}$, enhances the contrast seen between breast density groups and normal tissue [40]. Most importantly, the changes in breast density seen in MRI from the administration of neoadjuvant chemotherapy was been correlated with DOSI measurements at various time points; after treatment they saw a decrease in water, hemoglobin and TOI, while the lipid content increased, demonstrating that optical measurements can characterize breast density [40].

1.4 Structured-light based diffuse optical tomography

As seen with recent work in optical imaging, there are various ways of manipulating light to collect information, such as controlling the wavelength of excitation light to get spectroscopic information, or with FD and TD techniques to be able to obtain the scattering parameters. Another way to modulate light is spatially: specifically, patterns of light can be shined onto a medium using a digital micro-mirror device (DMD). A DMD is an array of micro-mirrors where each mirror acts as a pixel and can be turned on, where light is projected onto an object, or turned off, where light is projected away from the object. This technique is referred to as structured-light, where the main advantage is wide-field illumination [47].

One notable technique that modulates light is structured-light with single pixel detection. Extensively researched at Rensselaer Polytechnic Institute (RPI), the technique spatially modulates both the illumination and detection of light [47]. A first DMD is used to project light in arbitrary patterns onto the tissue while a second DMD is used to spatially modulate the collected transmitted light and integrates the signal into a point detector, such as a photomultiplier tube (PMT) [47]. With multiple patterns used for both illumination and detection, every measurement is a unique combination of a given source-detector pattern pair. This technique can be used to tomographically reconstruct the optical properties within the volume of interest. Recent developments have been applied for fluorescence tomography [48] and time-resolved DOT [49].

1.4a. Measuring breast density with structured-light

Our group has adapted the structured-light technique from RPI and is applying it to measure breast density. Using structured-light DOT (SL-DOT), structured-light (SL) patterns can be illuminated onto a lightly compressed breast using the projection DMD, while the transmitted light is collected by a lens and projected towards a collection DMD (Figure 3a). This collection DMD sends the selected light pattern towards another lens, which focuses the light pattern into a PMT, thus integrating all of the collected photons from this particular light pattern. Therefore, each intensity measurement is a unique combination of the patterns used for each of the source and detection DMDs. Figure 1b-c shows two examples of SL pattern sets, where the white area of the patterns represents the region on the object where light is illuminated or detected, while the black areas represent where light is neither illuminated nor

detected. With the first pattern set (Figure 3b), 12 distinct patterns are used on both source and detector sites, resulting in a total number of 144 measurements. With the second pattern set (Figure 3c), 10 distinct patterns can be used in combination, totaling to 100 distinct measurements.

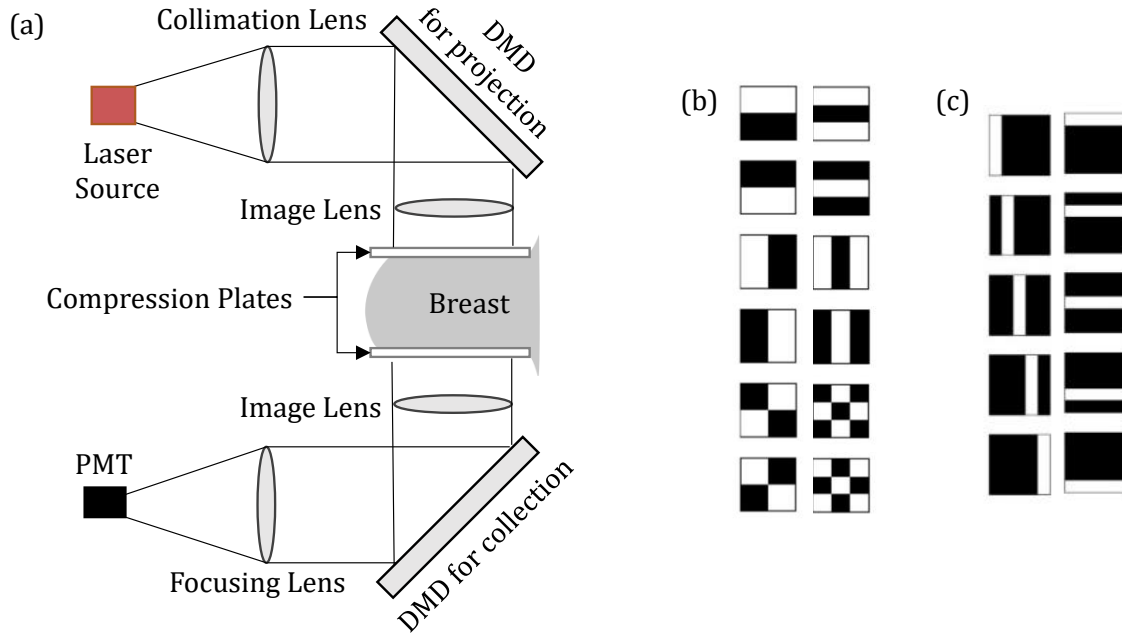


Figure 3. (a) Diagram of SLP-DOT for breast imaging. A laser is collimated onto an array of DMDs, which control and shine arbitrary patterns of light. Light travels through the breast, and is collected by another DMD, which integrates the signal according to a pattern and sends the light into a photomultiplier tube (PMT). Sample patterns are shown in (b) and (c), where white represents where light is illuminated or collected and black is un-projected or rejected signal.

Near-infrared light can easily propagate through a slightly compressed breast, allowing us to interrogate the entire breast volume with both wide-field illumination and detection. Another advantage of this technique is the rapid data acquisition made possible by the use of the second DMD and the PMT. The PMT is used to quickly integrate the collected light into a large signal measurement. This is advantageous, especially in situations with low signal levels, where traditional detectors such as

charged-couple device (CCD) cameras would require longer integration times to obtain a sufficiently large signal. The system's fast data acquisition makes it ideal as a risk assessment tool. This is an important aspect for its clinical implementation because multiple wavelengths of light are required for chromophore quantification. An additional detail to consider is that the spectral response range of a typical PMT goes up to 850nm. The absorption of light by oxy- and deoxyhemoglobin dominate in the 600-825nm range, making the detector only sensitive to these two chromophores. Water and lipid, which both dominate in the 850-1000nm range, would be very difficult to quantify with measurements from a standard PMT. The addition of a NIR-PMT, whose spectral response is 850-1000nm, would expand the wavelength window of our system and allow us to quantify all four chromophore concentrations. Typical CCD cameras are insensitive to longer wavelengths and cameras for NIR imaging are costly. By integrating the signal with the second DMD into a PMT allows us to quantify all of the relevant chromophores at a lower expense.

1.5 Innovations and contributions

This work has achieved several innovative contributions:

1. The application of optical tomography alone to image a volume, perform segmentation and quantify the %BD has not been done by the previously mentioned groups. Several groups measure and image the bulk chromophore concentrations from points along the breast [34,40,50]. Another group uses spectral information from data collected with transmission measurements to estimate the %BD without imaging the entire volume [44]. Another group combines DOT with MRI to

tomographically reconstruct the FGT distributions within the breast [38,39,51], but relies on MRI for structural a priori information. Considering all of the work that has been previously done, we have applied SL-DOT to tomographically reconstruct the 3D chromophore concentrations within the breast and based on this, we perform segmentation to recover the FGT volume and %BD.

2. Because our system provides 3D images of each of the chromophores within the breast, we can effectively use water and lipid for anatomical BD and use oxy- and deoxy-hemoglobin for functional BD, where anatomical and functional BD are independent risk factors for breast cancer. To our knowledge, none of the groups have pursued the measurement of a functional BD that correlates with the MRI-related BPE.

3. There have been no other groups that have applied SL-DOT to image and measure breast density. While there has been work done previously at RPI [47-49], their focus is on improving and enhancing the technique to measure fluorescence and incorporate TD measurements. We have also further pursued the recovery of 3D chromophore concentrations from the SL-DOT measurements.

Chapter Two: Theoretical basis of diffuse optical tomography

2.1 Photon interactions with biological tissue

In diffuse optics, the body is illuminated with an external light source. Light photons travel through tissue and exit the body, where they are collected by a photodetector [25,26,52-57]. In order to be able to extract information about the internal optical properties of the tissue from these external optical measurements, we need to understand how photons interact with and propagate through biological tissue [54]. During their propagation through the tissue, photons can be either absorbed or scattered by molecules in the tissue [25]. This results in a lower amount of measured light than the amount initially injected into the tissue [58]. The amount of absorption and scattering photons undergo is dependent on the molecular composition of the tissue, forming optical contrast between different tissue types. Therefore, from the attenuation of light seen at the boundary, we can infer the internal breast tissue composition [34,41,50,59-63]. In addition, collecting measurements at multiple boundary positions allows the tomographic recovery of the internal distribution of these different tissue types within the breast [52]. Based on this, we can visualize the fibroglandular tissue within the breast, which is the parameter of interest in this study.

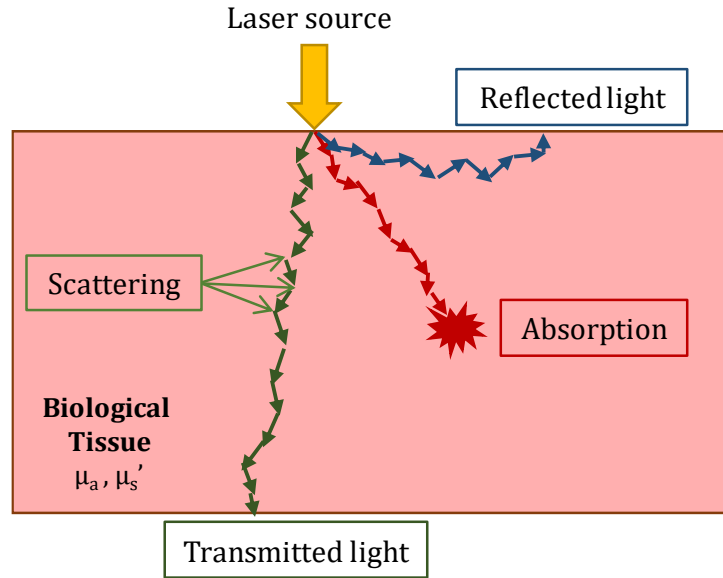


Figure 4. Illustration of photon interaction with biological tissue, where scattering changes the directions of the photons (indicated by arrows) and absorption extinguishes photons (indicated by star). Photons escaping the tissue on the same side of the source are reflected light and photons escaping on the opposite side of the source are transmitted light.

As previously mentioned, when traveling through tissue, photons can be absorbed by the medium. During this event, the photon is extinguished and can no longer propagate through the tissue; therefore, it cannot be detected at the boundary (Figure 4). The *absorption coefficient*, μ_a [mm^{-1}], represents the probability of a traveling photon to be absorbed. The inverse of μ_a ($\frac{1}{\mu_a}$ [mm]) refers to the average distance a photon will travel before being absorbed [64]. The decay of light by absorption when traveling through a tissue of thickness x is described by the modified Beer-Lambert law [65]:

$$\frac{I}{I_0} = \exp(-\mu_a \cdot x) \quad (1)$$

where I and I_0 are the measured and the initial intensities of light, respectively. The absorption coefficient of a given chromophore within a medium is dependent on its concentration C [M] and the wavelength of the light source used, λ :

$$\mu_a(\lambda) = \ln 10 \cdot \varepsilon(\lambda) \cdot C \quad (2)$$

where $\varepsilon(\lambda)$ [$M^{-1} \text{ mm}^{-1}$] is the wavelength-dependent extinction coefficient for a specific chromophore. When multiple chromophores are present within a given tissue, its total absorption coefficient is simply the sum of all the individual absorption coefficients of these chromophores:

$$\mu_a(\lambda) = \sum_i^N \mu_{a_i}(\lambda) = \ln 10 \sum_i^N \varepsilon_i(\lambda) \cdot C_i \quad (3)$$

where N is the number of chromophores. In the so called *therapeutic window* (650-1350nm), the most important absorbing chromophores found within the breast tissue are water, lipid, deoxy- and oxyhemoglobin [33,38,45,65], all of which have their own unique absorption spectrums (Figure 5) [66–68]. By taking measurements and estimating the μ_a at multiple wavelengths, equation (3) can be used to recover multiple chromophore concentrations. The fibroglandular and adipose tissue have different composition of these chromophores, which results in optical contrast between the two tissue types.

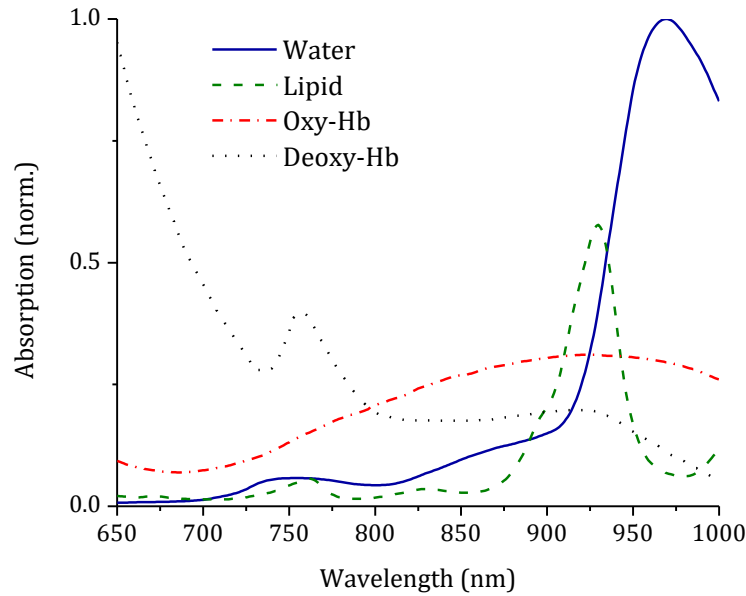


Figure 5. The absorption spectrum in the near-infrared spectral window are shown for water [66], lipid [67], oxy- and deoxyhemoglobin [68].

In addition to absorption, a photon can also undergo scattering while traveling through biological tissue. In a scattering event, a photon is not extinguished, but changes direction from its original line of path (Figure 4). Multiple scattering events result in high diffusion of light throughout the tissue. This will also cause a lower signal of light detected at a photodetector positioned directly across from source even if absorption is negligible. The *scattering coefficient*, μ_s [mm^{-1}], is similar to the absorption coefficient in which it represents the probability of a photon being scattered [64]. Biological tissue is highly scattering, where photons will travel very short distances before they are scattered. Not only is biological tissue characterized with a high scattering coefficient, but it is also highly forward scattering. This parameter is captured by the anisotropy factor, g , which is the average of the cosine of the scattering angle when a photon is scattered [69]. If g is close to 1, photon will

be scattered in the forward direction. Conversely, values close to 0.5 show no preference for direction. Because it is complex and impractical to estimate μ_s and g separately, they are combined into the *reduced scattering coefficient*, μ_s' [mm^{-1}], term:

$$\mu_s' = \mu_s(1 - g). \quad (4)$$

Scattering within tissue is not isotropic, meaning that the photons will not scatter in all directions equally. Instead, scattering within tissue is anisotropic and photons are more likely to be scattering forward, with values of g typically between 0.8 and 1 for tissue [70]. The inverse of the reduced scattering coefficient, called the transport-mean-free pathlength, describes the distance a photon will travel before becoming fully isotropic, where the original direction of the photon when it entered the tissue has been lost [64]. The extent to which a tissue will scatter light depends on the size and spatial distribution of molecules present in the medium:

$$\mu_s'(\lambda) = a \cdot \lambda^{-b} \quad (5)$$

with a and b as tissue-specific parameters [70].

2.2 Photon propagation model

2.2a. Modeling Near-infrared Light Propagation in Biological Tissue

The radiative transfer equation (RTE) is a derivation of Maxwell's equations that is an appropriate model for light propagation through tissue [64,71,72]:

$$\frac{1}{v} \frac{\partial L(r, \hat{\Omega}, t)}{\partial t} + \hat{\Omega} \cdot \nabla L(\vec{r}, \hat{\Omega}, t) = -\mu_t L(\vec{r}, \hat{\Omega}, t) + \mu_s \int_{4\pi} L(\vec{r}, \hat{\Omega}', t) p(\hat{\Omega}' \rightarrow \hat{\Omega}) d\hat{\Omega}' + Q(\vec{r}, \hat{\Omega}, t) \quad (6)$$

where v is the speed of light in tissue, $L(r, \hat{\Omega}, t)$ [$W \text{ mm}^{-2} \text{ sr}^{-1}$] is the light radiance at position r with $\hat{\Omega}$ directionality at time t , μ_t [mm^{-1}] is transport coefficient $\mu_a + \mu_s$, $p(\hat{\Omega}' \rightarrow \hat{\Omega})$ is the phase function that describes the probability of a photon scattering to direction $\hat{\Omega}$ given its original direction $\hat{\Omega}'$, and $Q(r, \hat{\Omega}, t)$ [$W \text{ mm}^{-3}$] is the light source. Solving the RTE is very complex due to the number of independent variables, specifically the directionality of the photons. The light radiance can be converted to photon density, $\Phi(\vec{r}, t)$ [$W \text{ mm}^{-2}$], by integrating the intensity of photons over all solid angles [64]:

$$\Phi(\vec{r}, t) = \int \int_{4\pi} L(\vec{r}, \hat{\Omega}, t) d\hat{\Omega} \quad (7)$$

where $\Phi(\vec{r}, t)$ is the photon density at position r and time t . When the scattering of a medium is predominant over the absorption. The photons become isotropic and the RTE can be simplified to the angle-independent photon diffusion equation under the assumption $\mu_s' \gg \mu_a$ [24,64]:

$$\frac{1}{v} \frac{\partial \Phi(\vec{r}, t)}{\partial t} - \nabla \cdot [D(\vec{r}) \nabla \Phi(\vec{r}, t)] + \mu_a \Phi(\vec{r}, t) = Q(\vec{r}, t) \quad (8)$$

where $D(\vec{r})$ [mm^{-1}] is the optical diffusion coefficient $\frac{1}{3(\mu_a(\vec{r}) + \mu_s'(\vec{r}))}$. Because

our system uses laser sources in continuous-wave (CW) mode, the photon diffusion equation can be further reduced to a time-independent form [27,52,53,73]:

$$[-\nabla \cdot D(\vec{r}) \nabla + \mu_a(\vec{r})] \cdot \Phi(\vec{r}) = Q(\vec{r}). \quad (9)$$

The Robin boundary condition was chosen to be the most appropriate method to model the photons behavior on the surface of biological tissue. The photon flux is obtained from the photon density as follow [74]:

$$\Phi(\vec{r}) + 2AD(\vec{r})\nabla\Phi(\vec{r})\cdot\vec{n} = 0 \quad (10)$$

where \vec{n} is the normal vector perpendicular to the surface and A is the boundary mismatch parameter that account for reflection at the boundary, based on Fresnel's reflections [71,74,75]. Therefore, the photon flux at the surface is calculated as:

$$\phi = -D(\vec{r})\frac{\partial\Phi}{\partial n} = \frac{\Phi}{2A} \quad (11)$$

where ϕ is the photon flux [$W\text{ mm}^{-2}$].

2.2b. Solving the photon diffusion equation

There are many different methods to solve the diffusion equation. An analytical solution can be formulated for specific conditions and quickly solved [54,76–87]; however, it is complex to solve, is limited to simplistic geometries and can only be used for mediums with homogeneous absorption and scattering distributions. Numerical methods offer a better solution for modeling photon propagation through complex geometries with heterogeneous optical properties. Monte Carlo is one numerical method that is widely implemented, where photon propagation is modeled based on the stochastic processes of absorption and scattering [88,89]. A number of photons are modeled through the medium, where a greater number of samples achieves more accurate results. While an advantage of Monte Carlo is that it can keep track of the path history of a traveling photon

throughout the medium, the need for large sample size makes it computationally long [90]. Alternatively, finite element method (FEM) can be used to solve the diffusion equation. Like Monte Carlo, it is geometrically flexible and can be used when the medium has heterogeneous optical properties. In FEM, the volume is discretized into small tetrahedrals connected by vertices known as mesh nodes [74,91]. The diffusion equation is solved over a short distance between these mesh nodes. FEM can be computed quickly and yields results as accurate as Monte Carlo [72]. For our photon propagation model, we chose FEM for its speed and its simple implementation.

In FEM, the diffusion equation, which is a partial differential equation (PDE), is solved by approximately solving its weak form, which is obtained by multiplying by an arbitrary weighting function φ and integrating over a volume of interest [92]. The weak form is formulated as [72,74,78]:

$$\int_{\Omega} \varphi \left[-\nabla \cdot D(\vec{r}) \nabla + \mu_a(\vec{r}) \right] \Phi(\vec{r}) d\Omega + \frac{1}{2A} \int_{d\Omega} \varphi \Phi(\vec{r}) d(d\Omega) = \int_{\Omega} \varphi Q(\vec{r}) d\Omega. \quad (12)$$

The solution to the PDE is assumed to be a linear combination of basis functions for each node j within a FEM mesh with N being the number of nodes, where:

$$\Phi = \sum_{j=1}^N \xi_j \varphi_j. \quad (13)$$

Additionally, the diffusion coefficient can be written as $D = \sum_{k=1}^N D_k \varphi_k$, the absorption

coefficient can be represented as $\mu_a = \sum_{k=1}^N \mu_{ak} \varphi_k$ and the arbitrary test function can

be rewritten as $\varphi = \sum_{x=1}^N \varphi_x$. The FEM representation of the photon diffusion equation

becomes [72]:

$$\begin{aligned}
 (A + B + C)\xi &= S \\
 A_{ij} &= \sum_{k=1}^N D_k \int_{\Omega} \varphi_k (\nabla \varphi_i \cdot \nabla \varphi_j) d\Omega \\
 B_{ij} &= \sum_{k=1}^N \mu_{ak} \int_{\Omega} \varphi_k (\varphi_i \varphi_j) d\Omega \\
 C_{ij} &= \int_{\partial\Omega} (\varphi_i \varphi_j) d(\partial\Omega) \\
 S_i &= \int_{\Omega} \varphi_i Q d\Omega \\
 \xi &= [\xi_1 \quad \xi_2 \quad \dots \quad \xi_N]
 \end{aligned} \tag{14}$$

Matrix algebra is used to solve for the expansion coefficients of the basis functions, which solves the FEM representation of the diffusion equation and thus providing the photon density at each node within the mesh. The boundary condition is applied where the photon flux is calculated at the surface nodes as discussed in equation (11). The calculation of the solution using FEM will be referred to as the *solution of the forward problem*.

2.3 Image reconstruction in diffuse optical tomography

There are many different techniques and algorithms to reconstruct the 3D internal optical properties from measurements performed at the boundaries of a volume [52]. For our study, we use a non-linear image reconstruction algorithm to

iteratively find the optical properties until convergence. Generally, the image reconstruction algorithm consists of generating predictions using a numeral model with a given set of optical properties, then comparing them with the experimental measurements. Our estimated optical properties are updated iteratively until the difference between the predictions and the measurements are minimized. This is referred to as *the solution of the inverse problem* [52].

2.3a. Inverse problem

The optimization scheme we employ minimizes the quadratic error between the experimental measurements and the prediction obtained using the current estimate of optical properties [27,52]:

$$\Omega = \min_{D, \mu_a} \|y_{s,d} - F(D_{s,d}, \mu_a)\|^2 \quad (15)$$

where Ω is the objective function being minimized based on D and μ_a , $y_{s,d}$ is a vector containing the measurements from using source s and detector d , and the operator $F(D, \mu_a)$ is the solution of the forward problem based on the current estimates for D and μ_a .

The main step in solving the inverse problem is the creation of a matrix which relates the variations of the internal absorption coefficient at any position within the medium to their induced perturbations in the measurements created using all the source-detector pairs. This matrix is commonly called the *sensitivity matrix* or *the Jacobian matrix*. This matrix can be obtained using the *perturbation theory*, which is based on the approximation stating that variations of μ_a will induce changes in measurements $y_{s,d}(\mu_a)$, which can be expressed by a Taylor series [52]:

$$y_{s,d}(\mu_{a1}) = y_{s,d}(\mu_{a0}) + \frac{\partial y_{s,d}(\mu_{a0})}{\partial \mu_a} [\mu_{a1} - \mu_{a0}] + \frac{1}{2!} \frac{\partial^2 y_{s,d}(\mu_{a0})}{\partial \mu_a^2} [\mu_{a1} - \mu_{a0}]^2 + \dots \quad (16)$$

The coefficients μ_{a0} and μ_{a1} respectively represent the initial and the perturbed state of the internal absorption coefficient μ_a .

Considering only the first order terms in equation (16), we obtain the following definition:

$$J_{s,d}(\mu_{a0}) = \frac{\partial y_{s,d}(\mu_{a0})}{\partial \mu_a} = \frac{y_{s,d}(\mu_{a1}) - y_{s,d}(\mu_{a0})}{\mu_{a1} - \mu_{a0}} \quad (17)$$

This matrix contains the amplitudes of variations in the measurements $y_{s,d}(\mu_a)$ caused by a variation in the internal absorption μ_a when source s and detector d are used. The full Jacobian describing all the variations for the whole set of source-detector pairs can be obtained by assembling all the individual Jacobians $J_{s,d}$. This full Jacobian is of size $M \times N$, where M is the number of measurements and N the number of mesh nodes.

From equation (17), we can write:

$$y_{s,d}(\mu_{a1}) - y_{s,d}(\mu_{a0}) = J_{s,d}(\mu_{a0}) [\mu_{a1} - \mu_{a0}] \quad (18)$$

Equation (18) shows that the updates of the absorption coefficient can be obtained by simply inverting the Jacobian $J_{s,d}$. However, the number of unknowns N is much greater than the number of measurements M , making the Jacobian a non-square matrix. Also, the Jacobian matrix is singular and its inversion is not a straightforward process. This limitation makes the inverse problem of DOT undetermined and strongly ill-posed. Hence, the pseudo inversion iterative algorithm of Levenberg-Marquardt is used to solve this problem [93,94]:

$$\Delta\mu_a = (J^T J + \lambda I)^{-1} J^T (y - F(D, \mu_a)) \quad (19)$$

where $\Delta\mu_a$ [Nx1] is the update to the absorption coefficient. μ_a is iteratively calculated and added to the current estimate of the absorption coefficient. I is defined as the identity matrix. The Hessian matrix, $J^T J$ [NxN] is known to be ill-conditioned. Several techniques exist to reverse this type of matrix [53]. The common one consists in adding a term to its diagonal for stabilization. $\tilde{\lambda} = \lambda \cdot \max(\text{diag}(J^T J))$ is the regularization factor used to improve the stability of the inversion of the Hessian matrix ($J^T J$) by making it diagonally dominant [95–100]. For every iteration, the residual error is calculated and is used to check for convergence. During this minimization, the iteration with the lowest residual is chosen as the correct set of μ_a values. The maximum number of iterations was set to 25 but if the residual has not changed more than 5% for 5 iterations, then the solution is accepted and the algorithm terminates.

2.3b. Construction of the Jacobian sensitivity matrix

As previously mentioned, the update to estimate our new optical properties is calculated using the Jacobian matrix J . Implementing the Jacobian matrix defined in equation (17) requires the resolution of the forward problem $N(N_S+1)$ times, with N_S being the number of sources. The first N_S times are solved to obtain the measurements $y_{s,d}(x)$ using the homogeneous set of optical properties $x=[\mu_a, \mu_s']$. Afterwards, the forward problem is solved after the sequential perturbation of x at every node of the mesh. Clearly, this method is very time consuming. Therefore, an alternative to computing the sensitivity matrix has been established, called the

adjoint method, which is based on reciprocity [52,91,101]. This method states that the influence of source s on detector d is the same as the influence of d on s when d is used as the source and s as the detector. Using this formulation, the Jacobian is simply obtained by solving the forward problem N_S+N_D times, where N_D is the number of used detectors. This adjoint method significantly reduces the Jacobian assembly time and the overall computation time [102].

For our initial studies, we focus on measuring the absorption coefficient only, and thus $x = \mu_a$ and μ_s' is considered constant and known. The Jacobian is thus constructed as:

$$J = \begin{vmatrix} \frac{d\Phi_1}{d\mu_{a1}} & \dots & \frac{d\Phi_1}{d\mu_{aN}} \\ \vdots & \ddots & \vdots \\ \frac{d\Phi_M}{d\mu_{a1}} & \dots & \frac{d\Phi_M}{d\mu_{aN}} \end{vmatrix} \quad (20)$$

where each row represents one measurement and each column represents each node in the mesh.

2.4b. Recovering chromophore concentrations

Based on the optical absorption maps recovered at multiple wavelengths, the water, lipid, oxy- and deoxy-hemoglobin concentrations are calculated using Equation (2). A system of linear equations can be constructed for each mesh node using L recovered absorption (μ_a) values and N known extinction coefficient (ϵ) of the chromophores [31,65]:

$$\begin{bmatrix} C_1 \\ \vdots \\ C_N \end{bmatrix} = \begin{bmatrix} \varepsilon(\lambda_1)_1 & \dots & \varepsilon(\lambda_1)_N \\ \vdots & \ddots & \vdots \\ \varepsilon(\lambda_L)_1 & \dots & \varepsilon(\lambda_L)_N \end{bmatrix}^{-1} \begin{bmatrix} \mu_a(\lambda_1) \\ \vdots \\ \mu_a(\lambda_L) \end{bmatrix} \quad (21)$$

This system of linear equations is solved with a non-negative linear least squares minimization, giving us the chromophore concentration for each node. Therefore, 3D maps for each chromophore, water, lipid, oxy- and deoxy-hemoglobin, are obtained.

2.4 Structured-light based DOT

The previously described image reconstruction algorithm describes DOT in general, where there is typically one source node that represents the position of each point laser source and one detection node that represents the position of each photodetector. The major difference between traditional DOT and structured-light DOT (SL-DOT) is the use of structured-light patterns over an area of the boundary in SL-DOT. Several modifications to the reconstruction algorithm need to be performed in order to reconstruct images from data taken with SL-DOT.

2.4a. Conversion of point sources to patterned sources

Point sources are normally modeled by the placement of a node at a position on the FEM mesh that mimics its location on the experimental setup. As imposed by the diffusion approximations, the node is placed inside the medium, at a depth of $1 / \mu_s'$, to model an isotropic light source. In SL-DOT, the source nodes are selected at a depth of $1 / \mu_s'$ to represent each source SL pattern. Given a binary pattern where light is either illuminated (1) or not illuminated (0), nodes that overlap with the illuminated areas of the pattern are chosen as the source nodes for that SL pattern.

Considering the irregular nature of the mesh, the number of nodes per SL pattern may not be uniform despite the SL patterns having the same amount of illuminated area. This results in some SL patterns having higher light intensity than others that have the same area. To correct for this, we modify the value of the light source when modeling the photon propagation with FEM. In traditional DOT, the single source node is set to 1 and the calculated photon fluxes are a fraction of that source light. In SL-DOT, every source node in the pattern is also assigned as 1, but multiplied by a correction factor. The correction factor is determined by the number of nodes and surface area of each SL pattern, normalized to the pattern with the maximum area in the set:

$$Q_s = \frac{1 \cdot \frac{N_s}{A_s}}{Q_M} \quad (22)$$

where Q_s is the value assigned to the nodes in source s , N_s is the number of nodes in source s , A_s is the area of the pattern s , and Q_M is the value $\frac{N_M}{A_M}$ of the source pattern with the largest area in the set. This ensures that the amount of light for each source pattern is dependent on the area of the pattern and not the number of nodes it contains.

2.4b. Integration of the flux on detection side

Like the source in traditional DOT, the detector is also represented by a single node. The flux is simply the value at the detector node calculated by solving the forward problem. SL-DOT uses a DMD to integrate the signal over a given SL pattern on the detection side, we need to consider the fluxes at all nodes in the detection

pattern and calculate their sum. We interpolate the flux values at the boundary nodes on to a finer Cartesian coordinate system with a rectangular grid (200 x 200) to match our SL patterns. The integrated flux is calculated as:

$$M_d = \sum_i^{P_d} A_i \phi_i \quad (23)$$

where P_d is the number of pixels in the that align with the detection SL pattern d , A_i is the area of the pixel and ϕ_i is the interpolated flux at the center of i^{th} pixel. This is done for each forward problem solved with a specific source SL pattern, resulting in $[S \times D]$ number of measurements.

Chapter Three: Measuring breast density using structured-light – simulation studies

Simulations were performed in order to test the feasibility of structured-light DOT in recovering the anatomical breast density. There is a large variety of FGT distributions within the breast, from having a centralized mass of FGT to having small pieces of FGT dispersed through the breast volume. Prior to phantom studies, we simulated optical measurements with breast-like numerical phantoms to understand the capabilities of SL-DOT and image various breast types with different FGT distributions.

3.1 Simplistic geometry phantoms

Our first simulation study looked at the ability of SL-DOT to recover absorption maps using different sized spherical inclusions centered inside a 3D rectangular geometry. The inclusion sizes ranged from 10 to 55mm in diameter, with 5mm intervals. SL-DOT measurements were created with our forward model and then used as inputs in our image reconstruction algorithm. Three-dimensional absorption maps were created for each case and were compared to the true geometry. Results were presented in terms of the percent volume of the sphere with respect to the total rectangular volume.

3.1a. Methods: Mesh creation

A rectangular phantom 100 x 90 x 60mm³ was created in COMSOL and then meshed. The mesh consisted of 9300 nodes and 46455 tetrahedral elements. The

inclusions were placed at the center by selecting the nodes that were within the spherical volume as defined by the Cartesian coordinate representation of a sphere. The inclusion had an absorption of 0.0374mm^{-1} and the background had an absorption of 0.0168mm^{-1} . These absorption values were calculated for a 1000nm light-source based on the assumption that FGT contains 80% water and 30% lipid, while adipose tissue contains 20% water and 70% lipid [39]. The scattering coefficient of both the inclusion and background was set to 0.6mm^{-1} [65,70].

3.1b. Generation of synthetic measurements

The pattern set consisted of vertical and horizontal stripes, as well as checkerboard patterns (Figure 6a). For each pattern, nodes that overlapped with the illuminated area of the pattern were chosen as the source or detector nodes (Figure 6b-d). The full pattern size projected onto the phantom was $70 \times 80\text{mm}^2$ centered onto the phantom surface, resulting in a 10mm margin on all sides. The source nodes were placed on the Y-Z plane at $x = 1.67\text{mm}$, which corresponds to $1 / \mu_s'$ below the surface. Then, the forward problem was solved sequentially by alternating the 12 source and the 12 detectors patterns, creating a set of 144 measurements. Each of these 144 measurements represent a unique combination of the source and detector patterns. These measurements will be later used as synthetic data for our image reconstruction.

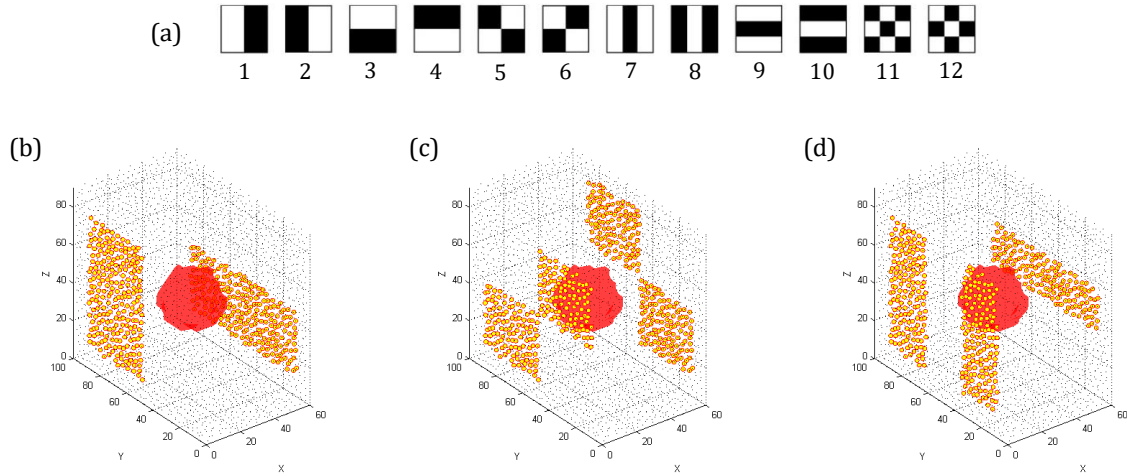


Figure 6. (a) The pattern set used for the simulations of spherical inclusions. Patterns consist of vertical and horizontal stripes as well as checkerboards. The white area represents where light is illuminated or detected and the black area represents where light is neither illuminated nor detected. (b-d) Nodes of the FEM mesh with a 30mm diameter spherical inclusion (red). The black dots are the boundary nodes. The yellow circles outlined in red are the source ($x=1.67\text{mm}$) and detector ($x=60\text{mm}$) nodes. Shown are the source and detector pattern combinations (b) 2 & 4, (c) 6 & 5, and (d) 7 & 10.

3.1c. Image reconstruction and analysis

During this study, it was found that our initial method to preliminary method to integrate the flux on the detection side was not realistically accurate. Prior to the method mentioned in the previous chapter, the flux was originally integrated by the direct summation of the values calculated at each element's center of gravity:

$$M_d = \sum_j^{E_d} A_j \phi_j \quad (24)$$

where M_d is the integrated intensity measurement for detector d , E_d is the number of elements whose vertices are the detection nodes, A_j is the area of the element j , and ϕ_j is the flux at center of element j , calculated by interpolating the central value within its three connected nodes. This improved the accuracy of the model, but because the elements are triangular and the SL patterns we use are rectangular, there may be cases where the triangular elements may not fall completely inside the

detection area, leading to an overestimation of the signal. Conversely, there may be triangular elements where the two of its nodes are inside the SL pattern, but one node fall outside, in which case the element will not be counted towards the integration and result in an underestimation of the flux. This led to our current method of calculating the measurements by interpolating the flux to a finer Cartesian coordinate system. Using the simplistic stripe pattern (Figure 7a), the forward model was solved on a phantom with homogenous optical properties. Both two methods were then used to integrate the flux on the detection side and compared (Figure 7b). Based on the appearance of the actual measurements, it becomes evident that using the Cartesian grid-based method is more accurate. Given that some of the SL-patterns within the set are mirror-images of each other, we expect that their integrated intensities would be of similar values, especially when performed on a homogenous phantom. The grid-based method produced measurements that are more symmetrical. The element-based method, however, lacks this symmetry. For example, measurement #1 and #100 result from source-detection pattern combinations 1 & 1 and 10 & 10, respectively. These SL-patterns are stripes that are along the edge and in both cases, the source pattern is directly across from the detection pattern. Given that there are no inclusions within the phantom, these two measurements should be the same. In the case of the element-based integration, these two measurements are not the same value; on the other hand, the grid-based method produced measurements where #1 and #100 are very similar (Figure 7b). For this reason, after we solve the forward problem, we interpolate the flux values to a finer Cartesian grid and integrate the intensities to form our measurements.

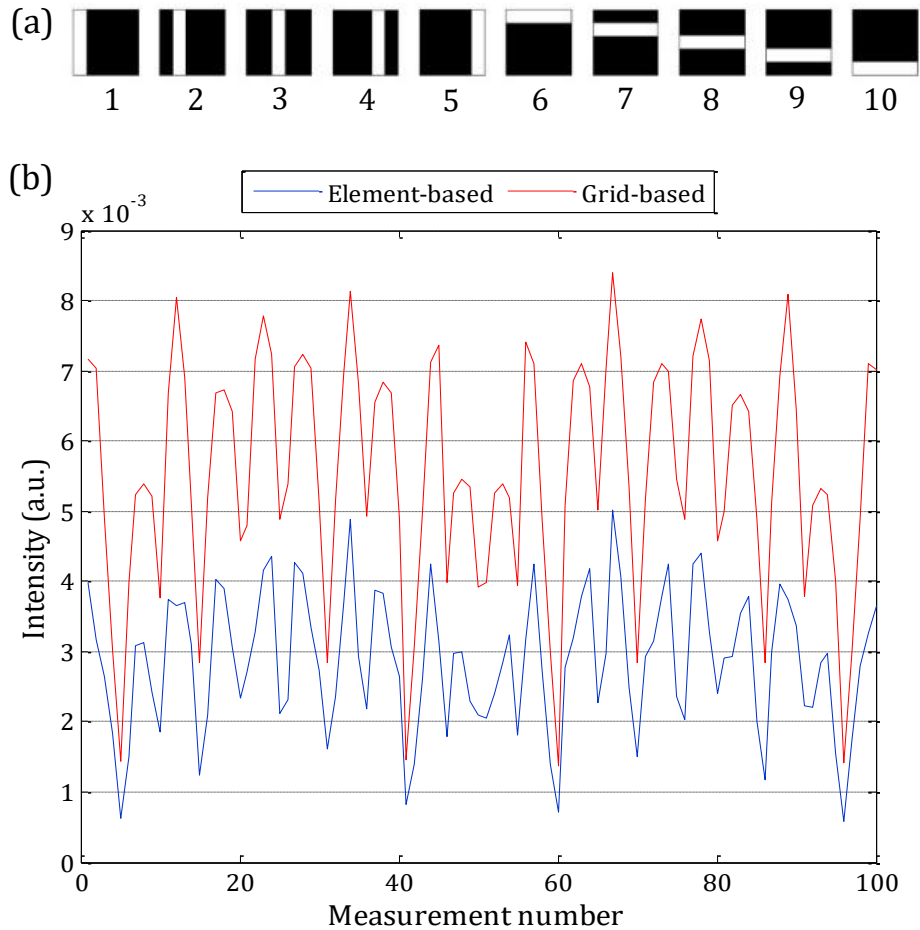


Figure 7. Simulated measurements were performed on a phantom with homogeneous optical properties with the pattern set presented (a). Comparison of the different methods to integrate the signal intensities on the detector side show that grid-based method performs the best, where the signals look smoother and symmetrical (b).

Our simulated measurements were then used in our reconstruction algorithm to find the 3D absorption maps of the numerical phantoms with different inclusion sizes. Image spatial resolution in DOT is generally low, especially when compared to MRI where internal structural boundaries are perfectly delineated. In our optical image reconstructions, we often get a diffuse-like image of an object and it may not be clear where to separate the inclusion from the background. For this reason, we rely on threshold-based segmentation of our absorption maps. Volumetric

information was extracted from the maps by segmentation at the half-maximum of the recovered absorption range. This segmented volume represents the reconstructed spherical inclusion, with higher absorption than the background.

3.2c. Results

The purpose of this simulation study is to look at the reconstructed absorption maps of simplistic spherical inclusions and to find a correlation between these maps and the true volumes of the spheres. From the reconstructed absorption maps, each sphere size case was segmented based on their own recovered absorption values. With the exception of the 10mm diameter case, the optical segmentations show a linear trend of increasing volume (Figure 8). The larger the case, the more accurate the optical segmentation is, where the difference between the reconstructed percent volume (%Vol) and the real value is smallest for the 50mm diameter case (Figure 8). The smallest sphere case was greatly overestimated (Figure 9a).

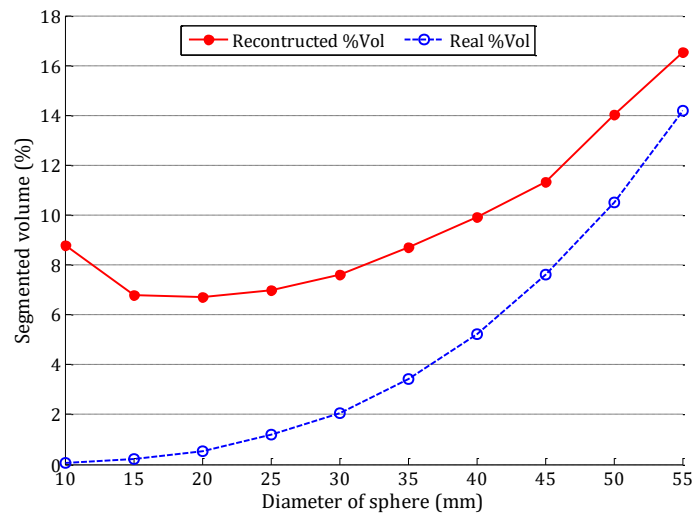


Figure 8. The real percent density of the spherical inclusions (blue) and the reconstructed percent volumes (red). With the exception of the 10mm diameter sphere case, the general trend of the segmented optical volumes increase as the sphere sizes increase, with more accurate results with larger objects.

In Figure 8, the optical segmented volumes are represented in the blue wireframe (bottom). The 2D representation of this segmentation can be seen as a green contour on the center slice of the absorption map (Figure 9a). As the size of the true inclusion increases, shown in red, the segmented volume, shown in the blue wireframe, becomes visually similar to the spherical inclusion.

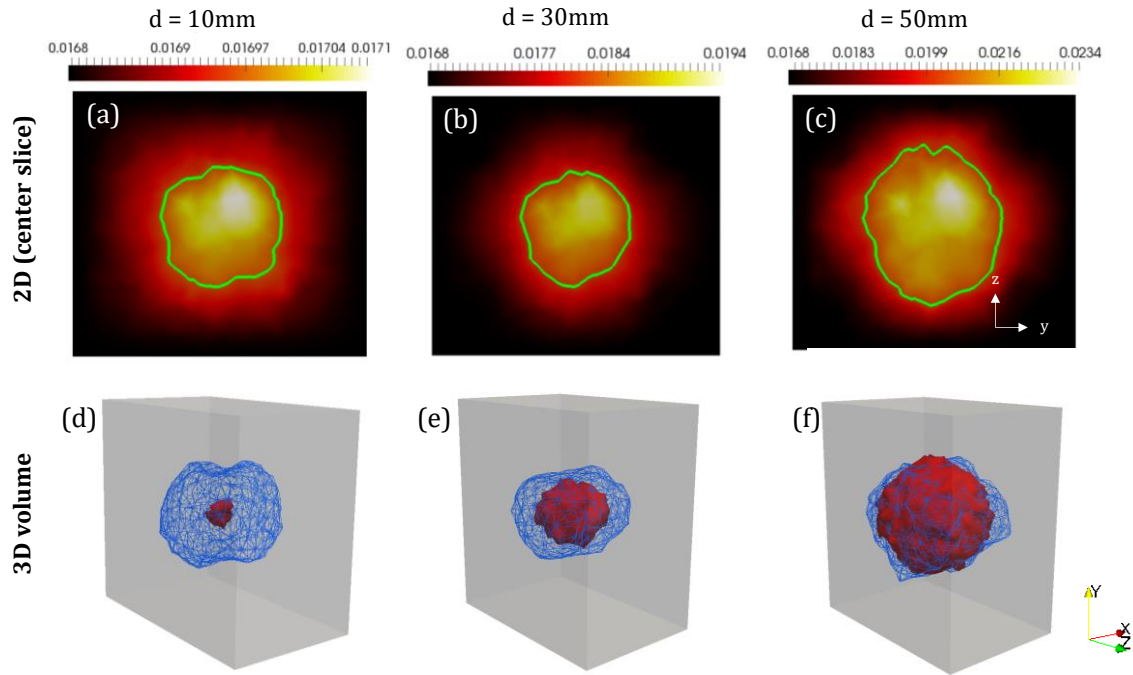


Figure 9. The central slice from the reconstructed 3D absorption maps for three different sphere sizes: (a) 10mm, (b) 30mm, and (c) 50mm diameter. The green contour outlined on each slice represents the segmentation at half-max of the recovered absorption values. n (d-f) The volumes segmented from the absorption maps are shown in the blue wireframe. The red object represents the true spherical inclusion used for simulating measurements.

The recovered absorption values for each case were also analyzed from a quantitative point of view. The mean absorption of the node values within the segmented volume was calculated:

$$\bar{\mu}_a = \frac{\sum_{i \in Vol} \mu_{ai}}{n} \quad (25)$$

where n is the number of nodes within the segmented volume, and μ_{ai} is the absorption value at node i . It was observed that the mean absorption for each case was related to the volume of the spherical inclusion (Figure 10).

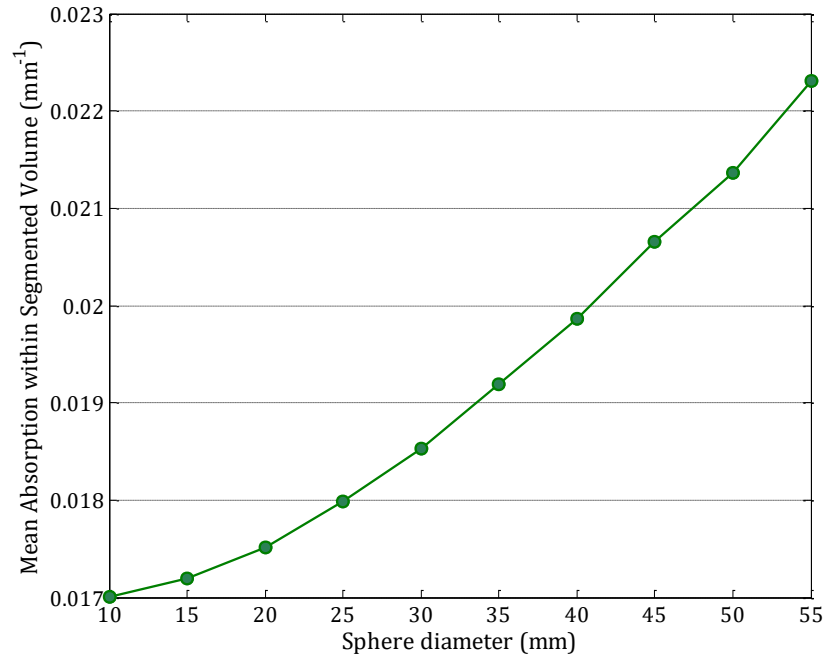


Figure 10. The mean recovered absorption value also has a relationship with the true sphere size, where smaller objects have lower recovered absorption and larger objects have higher recovered absorption

3.2 Numerical breast phantoms

While our first study aimed to investigate recovering an inclusion with a simple geometry, our second simulation study focused on the performance of SL-DOT in imaging realistic FGT geometries. This study compares the percent breast density (%BD) obtained from the reconstructed absorption maps with the original MRI %BD. Seven MR breast cases were segmented to build the breast volume and the internal FGT geometries. Afterwards, synthetic measurements were created, from which the

absorption maps were reconstructed. Finally, the volumes segmented at the half-maximum were used to obtain the %BD using our method and then compared to the MRI %BD.

3.2a. Methods: Building the numerical breast phantoms

Seven T1-weighted MR unilateral breast cases, where the adipose appears bright and the FGT appears dark, were imaged from healthy volunteers (Figure 11a). The cases were segmented using a previously developed in-lab k-means clustering algorithm to define the breast wall and to separate the FGT from the adipose tissue (Figure 11b) [20]. Each case consisted of slices, depicting the 3D images of the breast and the FGT. The MRI images were cropped to include only the breast of interest, where the bottom horizontal boundary was chosen to exclude the chest wall but include the breast as much as possible. The breast images were then used to create a computer-aided design (CAD) file (.stl) in MATLAB (Mathworks; Natick, Massachusetts). The CAD file was then exported to COMSOL Multiphysics (COMSOL; Stockholm, Sweden) to build the 3D geometry from the surface defined by the CAD file. After obtaining the 3D geometry, the COMSOL mesh generator was used to discretize the numerical geometry into small tetrahedrals. The source and detector planes were finely meshed compared to the other boundaries, creating a high density of nodes that can be chosen to represent the structured-light patterns. The FEM mesh information for each breast was exported back to MATLAB, where the FEM basis functions were created for each case. The FGT segmentations from MRI were then used to designate nodes within the mesh as FGT, by matching the 3D coordinates of the segmentations to the node coordinates in the mesh (Figure 11c). The remaining

nodes were designated as adipose tissue. The initial absorption properties that were assigned were 0.005mm^{-1} and 0.02mm^{-1} for the adipose and fibroglandular tissue, respectively. For simplicity, the scattering coefficient for both adipose tissue and FGT was 0.6mm^{-1} .

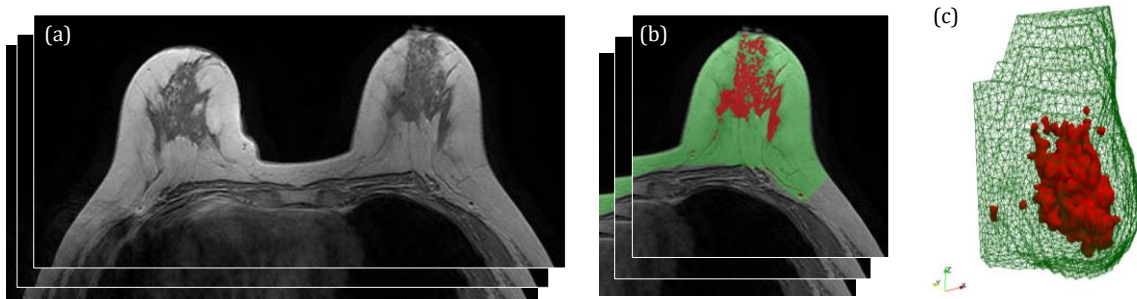


Figure 11. (a) Breast MR image is segmented to have the chest wall removed and is separated into a unilateral breast image. (b) The segmented breast MR slices separate the fibroglandular tissue from the breast volume. (c) Using the coordinates from the fibroglandular tissue geometries, the fibroglandular tissue was defined at specific nodes (red) with the FEM mesh. The green wiring represents the boundary elements.

3.2b. Methods: Simulation of SL-DOT measurements

For each breast case, the same pattern set used in the previous study was also used to designate the source and detector nodes (Figure 6a). On both the source and detector planes for each FEM mesh, a rectangular field-of-interest (FOI) for illumination and detection was chosen manually for each breast case. This FOI represents the boundaries of the SL patterns. Because the breast surface is not flat, the plane of the SL pattern lies along the curved surface of the breast. The FOI is maximized as much as possible on this curved surface without allowing its corners to wrap around the sides of the breast (Figure 12). This was done to replicate the real-life scenario where we avoid allowing the light source to directly enter the detector

without having passed through the breast. The synthetic measurements were then created as previously mentioned.

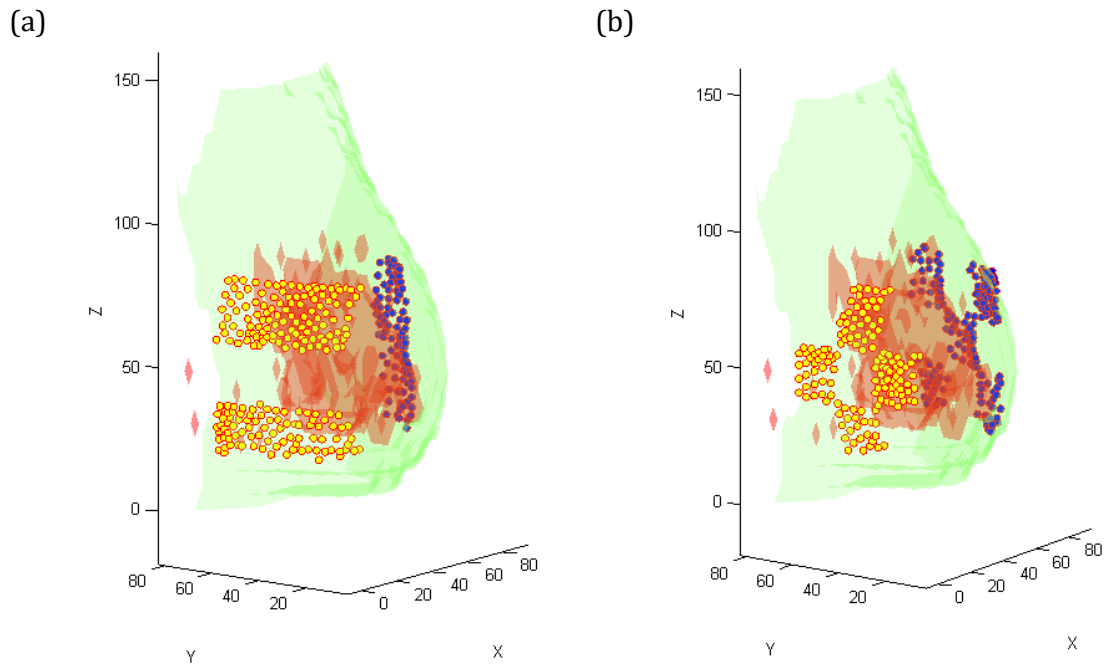


Figure 12. Example of how the source (yellow circles) and detector (blue circles) nodes are placed onto the breast. The boundary of the breast is shown in green and the FGT is shown in red. Shown are source and detector pattern combinations (a) 7 & 10 and (b) 12 & 11.

3.2c. Methods: Image reconstruction and analysis

Using the previously created synthetic measurements, the inverse solver was used to find the internal absorption distribution of the breast. For each case, the image reconstruction algorithm produced a 3D absorption map at each iteration of the minimization. The best solution was chosen from the iteration with the smallest residual error.

Similar to the previous study, a volume was segmented at the half-maximum of the recovered values of the 3D absorption maps. This volume was used to represent

the recovered FGT volume within the breast. From this volume, we calculated the optical %BD, which is the ratio of the FGT and the breast volumes, denoted as % V_{abs} .

3.2d. Results

Volumetric information that was extracted from the reconstructed absorption maps was compared to the volumetric information obtained from MRI. The 3D segmentations of the absorption maps (blue wireframe) for three cases are presented in Figure 13a-c. Although correlated ($r = 0.93$), it has been generally observed that lower density cases tend to be overestimated and higher density cases tend to be underestimated (Figure 13d).

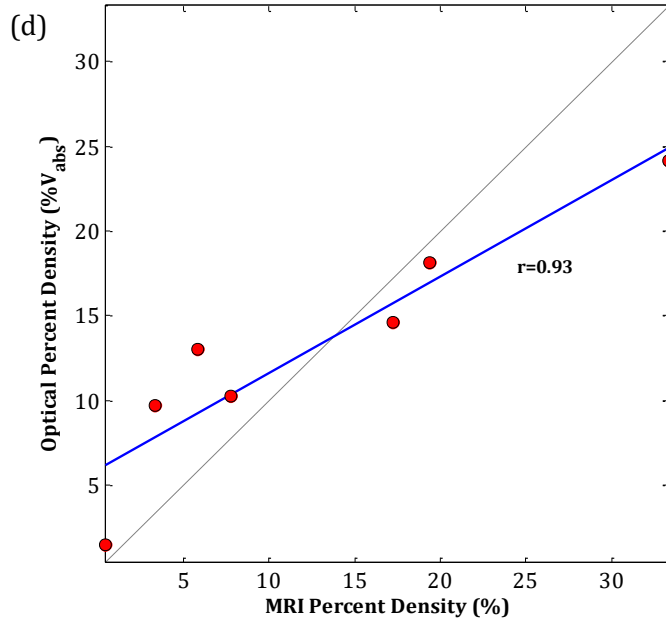
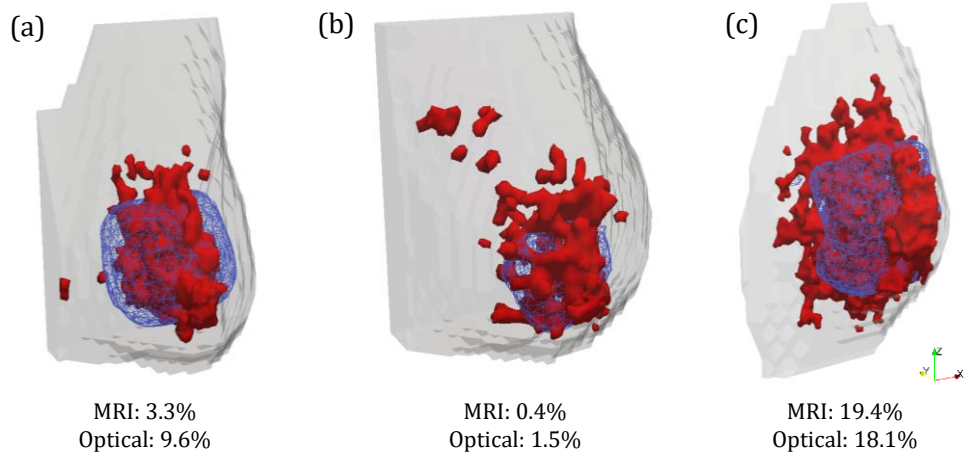


Figure 13. (a-c) The 3D segmentations of the reconstructed absorption maps for three different cases. The segmented optical volume is shown in the blue wireframe with the MRI-generated FGT geometries shown in red. (d) The correlation between the optical percent density and the MRI-based percent density for six cases are shown. The low density cases are above the line of unity (dashed line), showing that they are overestimated, while the higher density cases are underestimated.

There was difficulty in maximizing the SL pattern FOI to cover the breast as much as possible without wrapping around of the side of the breast. FGT can lie far from the FOI, making it difficult to recover and has been encountered in one case

(Figure 14). The MRI %BD is 33.31% while the optical %V_{abs} was 24.12% (Figure 14b). This can be solved by changing the FOI from a rectangular shape to a complex shape that covered the entire breast. The use of DMDs to spatially modulate the SL light patterns can also be used to spatially modulate the FOI, thus achieving shapes that match the breast profile.

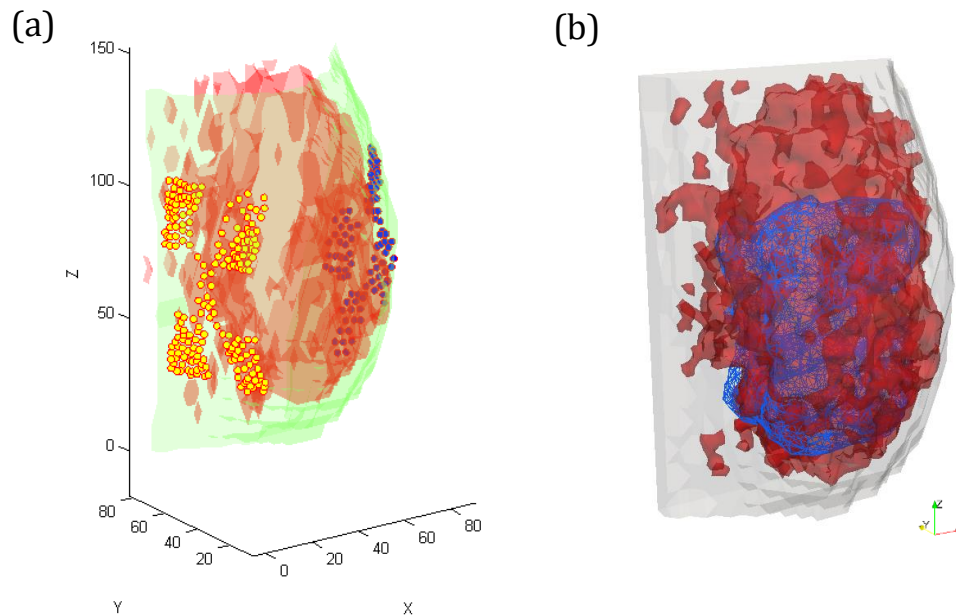


Figure 14. (a) Highly dense breast case where SL pattern FOI does not cover the entire breast volume. (b) The segmented optical volume (24.12%, blue wireframe) is underestimated compared to the true FGT density (33.31%, red).

Additionally, the FGT geometries seen in MRI are very complex, where radiologists can visualize and describe breasts as “fatty,” “scattered,” and “heterogeneously dense.” This is related to the BI-RADS categorization, and also refers to not only the size of the dense tissue but also to its distribution. For the purpose of our study, we have used different FGT morphologies which can be classified as “intermingled” type (to avoid confusion with the optical property of *scattering*) and “centralized” type (to avoid confusion with the term *optical*

heterogeneity). Intermingled geometries describe FGT that is dispersed into many smaller pieces throughout the breast and centralized geometries describe FGT that is mostly a large mass without many gaps. The next study aims to further look at SL-DOT reconstruction of these complex tissue morphologies.

3.3 Chromophore reconstruction and analysis

To test the feasibility of SL-DOT in quantifying breast density, we conducted a simulation study using numerical phantoms made from healthy breast MR images [103]. From these images, we built the FGT geometries and integrated them into a rectangular geometry to model a slightly compressed breast. The forward problem was solved to create synthetic measurements, which were then used in our image reconstruction algorithm. We recovered the 3D absorption properties and subsequently the 3D chromophore maps. We analyzed the water and lipid maps in order to obtain an optical-based %BD.

3.3a. Methods: Breast numerical phantom generation

In order to model a slightly compressed breast, a rectangular geometry, $60 \times 100 \times 90 \text{m}^3$, was used. This geometry was meshed using COMSOL into 46455 tetrahedral elements connected at 9300 nodes. Light was projected onto Y-Z plane ($x=0\text{mm}$), propagated through x-axis of the phantom and detected on the opposite ($x=60\text{mm}$) plane.

To mimic realistic FGT distributions, 45 (31 central and 14 intermingled tissue morphologies) segmented T1-weighted unilateral breast MR images of healthy patients were used (Figure 15). The coordinates of the FGT's binary segmented masks

were used to designate which of 9300 nodes are considered FGT, with the remaining nodes designated as adipose tissue (Figure 15g-i). For the FGT cases that exceeded the volume of the rectangular geometry, the FGT volume was rescaled equally in all dimensions (maintaining the original aspect ratio) until the FGT was fully within the rectangular geometry.

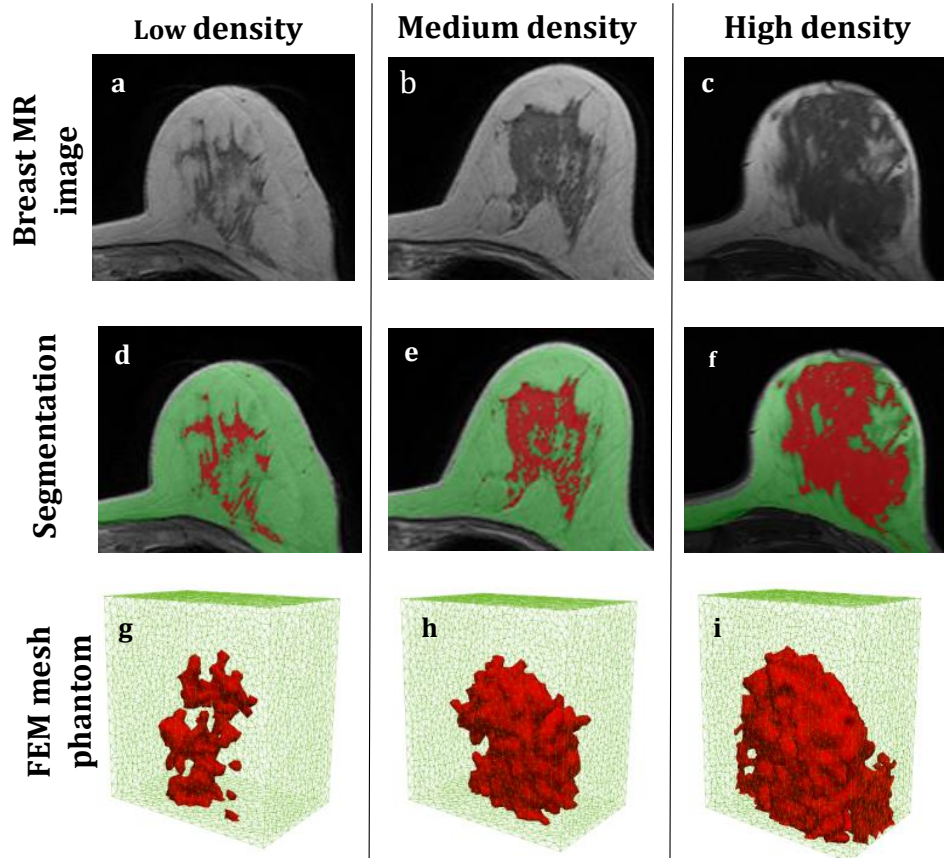


Figure 15. (a-c) Central breast MR slices are shown for three cases of increasing density. (d-f) All of the MRI slices for each case are segmented to separate the FGT from the breast volume. (g-i) These FGT volumes are then used to build numerical breast phantoms within a rectangular FEM mesh. [103]

3.3b. Methods: Simulations

As introduced in the previous chapters, the main chromophores of interest present in the breast within the therapeutic window are: water, lipid, oxy- and deoxy-

hemoglobin. Different absorption coefficients values were attributed to the two tissue types of the phantom. This is based on the fact that contrary to adipose tissue, FGT has a higher water content and lower lipid content (Table 1) [41,46,104]. For our preliminary tests, we focused on measuring the differences between water and lipid levels to calculate the anatomical percent densities. For this reason, the total hemoglobin levels of the FGT and adipose tissues to $30\mu\text{M}$ and $15\mu\text{M}$, respectively (Table 2). This is within the range of hemoglobin concentrations found throughout literature [33,45,46]. The tissue oxygen saturation ($\%StO_2$) of the FGT and adipose tissue were assumed to be 75% and 80%, respectively, where it has been found that FGT typically has a lower $\%StO_2$ than adipose tissue [39,46,105]. Synthetic measurements were simulated using our FEM SL-DOT solver at five different wavelengths: 760, 780, 830, 925 and 950 nm (Table 2).

Table 1. Concentrations of water, lipid, oxy- and deoxyhemoglobin chromophores chosen for both adipose and fibroglandular tissues.

Tissue	Water	Lipid	Oxyhemoglobin	Deoxyhemoglobin
Adipose	30%	70%	$6.25\mu\text{M}$	$2\mu\text{M}$
Fibroglandular	70%	30%	$18.75\mu\text{M}$	$8\mu\text{M}$

Table 2. Absorption coefficients for both adipose and fibroglandular tissue at five wavelengths. Absorption values were calculated from proposed chromophore concentrations from Table 2 using equation (3).

Tissue	760nm	780nm	830nm	925nm	950nm
Adipose	0.0035 mm^{-1}	0.0028 mm^{-1}	0.0035 mm^{-1}	0.0157 mm^{-1}	0.0169 mm^{-1}
Fibroglandular	0.007 mm^{-1}	0.0063 mm^{-1}	0.0075 mm^{-1}	0.202 mm^{-1}	0.0345 mm^{-1}

3.3c. Chromophore map analysis

The simulated measurements were used as inputs in our image reconstruction algorithm. The inverse problem was solved for each wavelength to provide the

estimated absorption coefficient at each node. Using Equation (21), we are able to calculate the 3D concentrations of the chromophores of interest at each node using a non-negative linear least squares minimization. Given the fact that the 3D maps of water and lipid are more correlated to the FGT, we explored various ways of quantifying the anatomical percent density. We did not choose to analyze the hemoglobin concentration maps because they are more indicative of blood perfusion of the FGT, which is similar to BPE-MRI. Because BPE is another independent risk factor and shown to be uncorrelated with the anatomical %BD [106], hemoglobin will be used in future analysis. There are two main approaches that other research groups have considered when relating the optical measurements to breast density: obtaining visual maps and delineating the FGT from the breast volume or using spectroscopic information to estimate the percent breast density. Since our technique is tomographic and provides 3D chromophore maps throughout the volume, segmentation based on the spatial distribution of the concentrations was first attempted. We segmented both the water and lipid maps at their respective half-maximum thresholds, for each case. We denoted this as $\%V_{water}$ and $\%V_{lipid}$ for water and lipid, respectively. Based on this, we explored two different approaches to correlate these chromophore maps to the anatomical breast density:

Approach 1: Because the $\%V_{water}$ and $\%V_{lipid}$ segmented for each case were highly correlated with each other, we chose one of the parameters ($\%V_{water}$) and compared it to the *MRI %BD*. This is similar to the absorption-based analysis that was performed in the previous simulation study.

Approach 2: We used the $\%V_{water}$ and $\%V_{lipid}$ in combination with the actual recovered chromophore values, specifically the mean concentrations within the segmented $\%V$, which we denoted as \bar{C}_{water} or \bar{C}_{lipid} :

$$\bar{C} = \frac{\sum_i^{N \in Vol} C_i}{N} \quad (26)$$

where N is the number of nodes within the $\%V$ and C_i is the concentration of node i . Then we formed a regression model incorporating all four parameters that will be further discussed.

3.3e. Results

Approach 1: Comparison between $\%V_{water}$ and MRI $\%BD$

The volumetric information from the water and lipid maps were extracted by segmenting the chromophore maps at the half-maximum and were compared to the MRI $\%BD$. Both the $\%V_{water}$ and $\%V_{lipid}$ are correlated with the real $\%BD$, with $r = 0.89$ (dashed-line) and $r = 0.85$ (solid-line) for the water and lipid volumes, respectively (Figure 16). The $\%V_{water}$ values were used for error analysis, where the absolute difference between the $\%V_{water}$ and MRI $\%BD$ was compared to the MRI $\%BD$ (Figure 17). Cases along the horizontal line ($y = 0$) have no difference between the $\%V_{water}$ and $\%BD$ MRI, and therefore have no error (Figure 17). The plot reveals low density cases are typically above the 0 error line, meaning they are overestimated (Figure 17). Conversely, high density cases are below the line, meaning they are underestimated (Figure 17). The same tendencies to overestimate smaller objects and underestimate larger objects have been seen in the previous two simulation studies. Furthermore,

the cases were categorized as either of centralized or intermingled FGT morphologies, which revealed that the two most overestimated cases are of intermingled type (Figure 17). It is interesting to note that the distribution of tissue morphologies among the *MRI %BD* also shows that higher density cases are typically centralized types, while low density cases can be either intermingled or centralized. This is because at higher densities, the FGT will more likely have fewer gaps and appear like a large centralized mass.

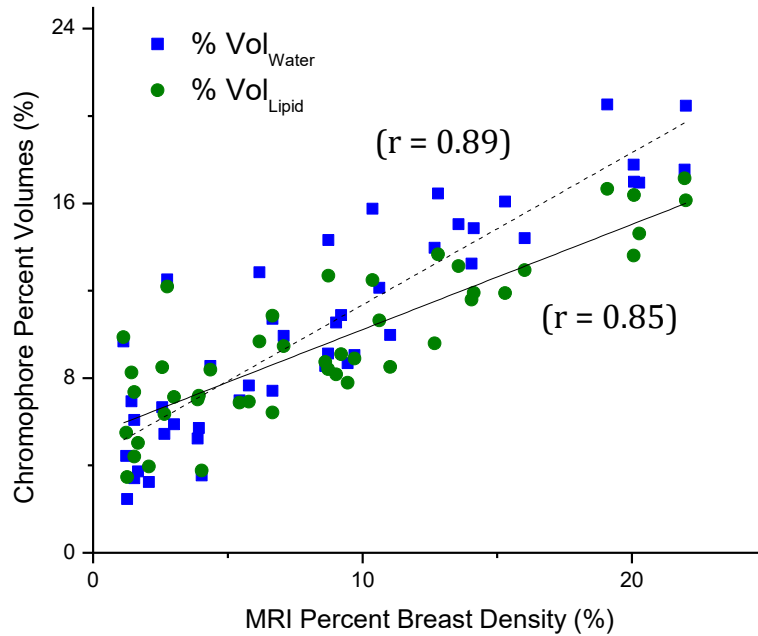


Figure 16. The relationship between both %Volumes and MRI %BD are shown. Water volumes (blue squares, $r=0.89$, dashed-line) and lipid volumes (green circles, $r=0.85$, solid-line) both show correlation with the MRI %BD.

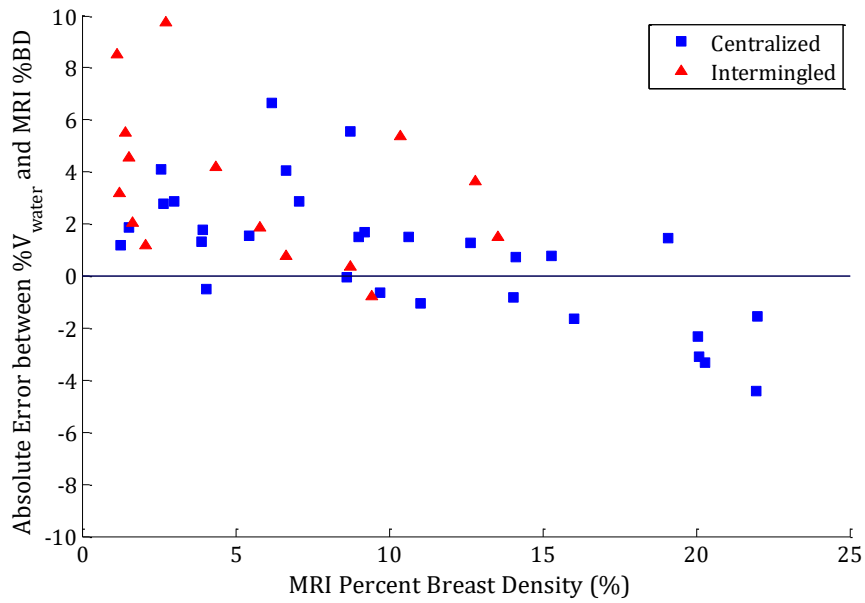


Figure 17. The absolute error between $\%V_{\text{water}}$ and MRI %BD is shown. The horizontal line marks 0, or no, error. Cases above this line are overestimated while cases below this line are underestimated. Discrimination between centralized (blue squares) and intermingled (red triangles) FGT morphologies show that the most overestimated cases are the intermingled FGT cases. [103]

Figure 18 presents three MRI breast cases: (a) a high density centralized case, (b) a low density centralized case, and (c) a low density intermingled case. The center slice of the water and lipid chromophore maps are presented in the second and third rows, respectively. On each chromophore map, the MRI-generated FGT geometries are outlined with a solid green line and the white dashed-line represents the 2D contour of the chromophore map segmentation (Figure 18). This figure illustrates that the high density case is underestimated, while the two low density cases are overestimated (Figure 18d-f, g-i). The two low density cases have similar *MRI %BDs*, but it was noted that $\%V_{\text{water}}$ was 3.4% for the centralized case and 6.08% for the intermingled case (Table 3). However, it can be visually seen on Figure 18 and from the values presented in Table 3, that the intermingled case had a lower \bar{C}_{water} and higher \bar{C}_{lipid} than the centralized case. The second approach we used to estimate the

%BD from the reconstructed chromophore maps uses these differences in the \bar{C} to correct for the over- and underestimations.

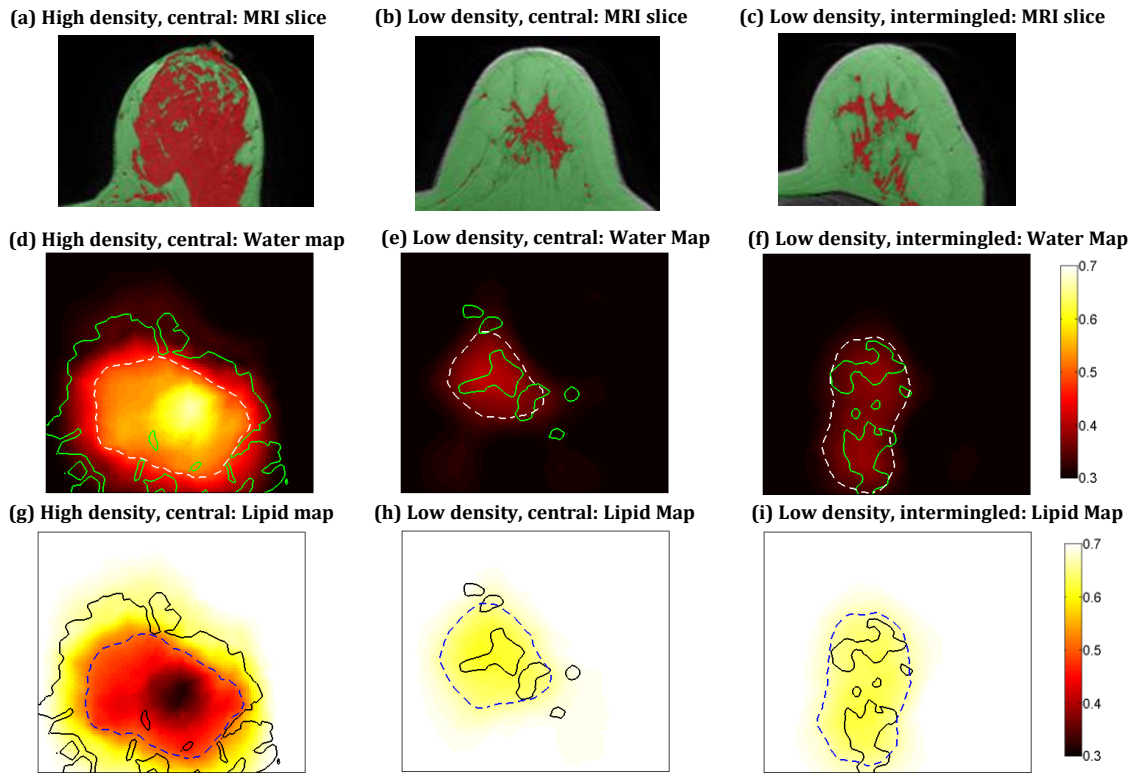


Figure 18. (a-c) Three breast MRI cases of different densities and tissue morphologies are presented. (d-f) The reconstructed water maps are shown, where the green outline shows the MRI-generated FGT while the white dashed-line shows the contour of the $\%V_{water}$ segmentation. (g-h) The lipid maps are also presented, where the black solid line is the FGT and the blue dashed-line is the $\%V_{lipid}$ segmentation contour. [103]

Table 3. The parameters of the three cases presented in Figure 18.

Breast density & morphology	High, centralized	Low, centralized	Low, intermingled
MRI %BD	16.02%	1.53%	1.53%
$\%V_{water}$	14.40%	3.40%	6.08%
\bar{C}_{water} (mol. fraction)	0.541	0.394	0.373
$\%V_{lipid}$	12.94%	4.40%	7.36%
\bar{C}_{lipid} (mol. fraction)	0.450	0.618	0.634

Approach 2: Comparison between a regression model and MRI %BD

It was observed that the recovered absorption coefficients were dependent on the distribution of the FGT, *i.e.* higher percent densities had a higher recovered absorption value than lower ones. This was also seen in the first simulation study, where smaller sized spheres had a lower recovered absorption (Figure 10). This dependency on FGT distribution also manifested itself in the recovered chromophore concentration maps. It is important to note that the recovered absorption value for all the cases tend to be between the μ_a for pure adipose tissue and the μ_a for pure FGT. In the case where a breast has less FGT, a lower absorption will be recovered within the %V. During the minimization to find the chromophore concentrations, the algorithm will estimate that the smaller FGT volume has higher lipid and lower water concentrations, traits of adipose tissue. Conversely, a case with more FGT will have higher recovered absorption values and be seen as more similar to pure FGT. Therefore, this case will have lower lipid and higher water concentrations. The relationship between the MRI %BD and the water and lipid \bar{C} for all 45 cases is presented in Figure 19. Using these trends, we formulated a regression model that can correct for the overestimation and underestimation of the %BDs.

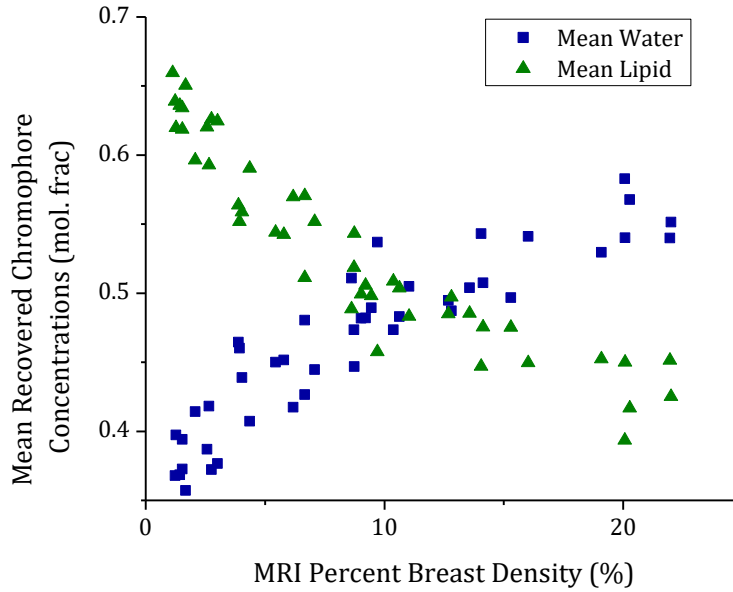


Figure 19. The mean water (blue) and lipid (green) concentrations within the segmented volume for each MRI case is shown. The plot shows that there is a dependency of the recovered chromophore concentrations on the MRI breast density, where high density cases have higher and lower recovered water and lipid, respectively. Lower density cases have higher recovered lipid and lower water concentrations. [103]

We built a regression model to estimate the $\%BD$ that uses the $\%V$ and corrects it with the \bar{C} for each case. Because the FGT size is positively correlated with the \bar{C}_{water} , we multiplied the $\%V_{water}$ directly by the mean water concentration:

$$Estimated \%BD = \beta \cdot \bar{C}_{water} \cdot \%V_{water} \quad (27)$$

where β is a coefficient found using a training set of 15 cases. This regression model corrects cases with a lower water concentration that would most likely be lower density cases. The coefficient β was found to be 1.87 and the model is shown in Figure 20 ($r = 0.96$).

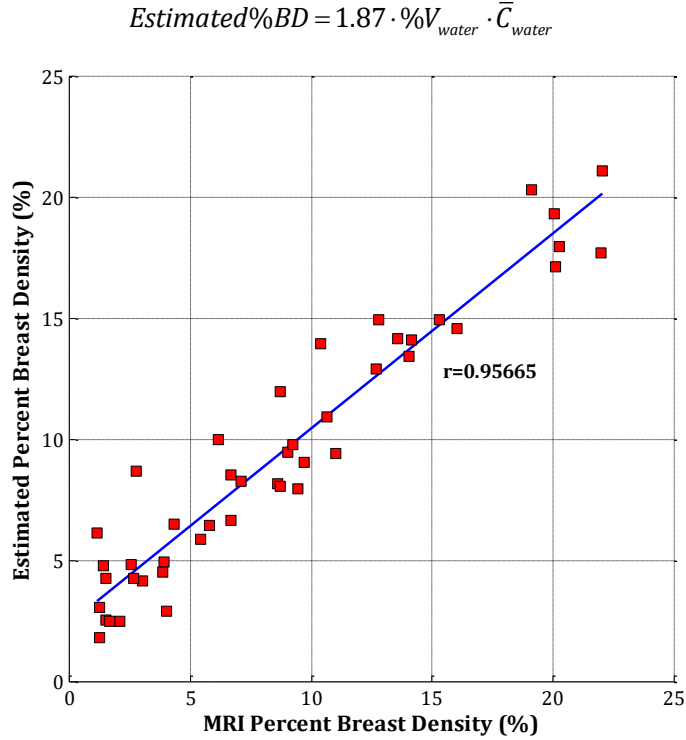


Figure 20. The estimated breast densities from the regression model that uses the $\%V_{water}$ and \bar{C}_{water} values show high correlation with the MRI %BD.

The FGT size was also seen to be inversely correlated with the lipid values and this was also incorporated into an expanded regression model in order to improve the prediction:

$$Estimated\%BD = \beta_1 \cdot \bar{C}_{water} \cdot \%V_{water} - \beta_2 \cdot \bar{C}_{lipid} \cdot \%V_{lipid} \quad (28)$$

The subtraction of the lipid term corrects for low density cases which have a higher lipid concentration. Using a training set of 15 cases, β_1 was found to be 2.62 and β_2 was found to be 0.84. This regression model's performance yielded a correlation coefficient of 0.97, which is slightly better than the previous model (Figure 21). Error analysis of this modified regression model shows that the absolute

difference between our estimation and the *MRI %BD* is well distributed around the horizontal no-error line, where there is no more tendency for low density cases to be overestimated and high density cases to be underestimated (Figure 22). Additionally, the largest error between our prediction and the *MRI %BD* was 3.8% (Figure 22). This is an improvement from the first method where we compared the $\%V_{water}$ and the *MRI %BD*, whose largest error was 9.8% (Figure 17).

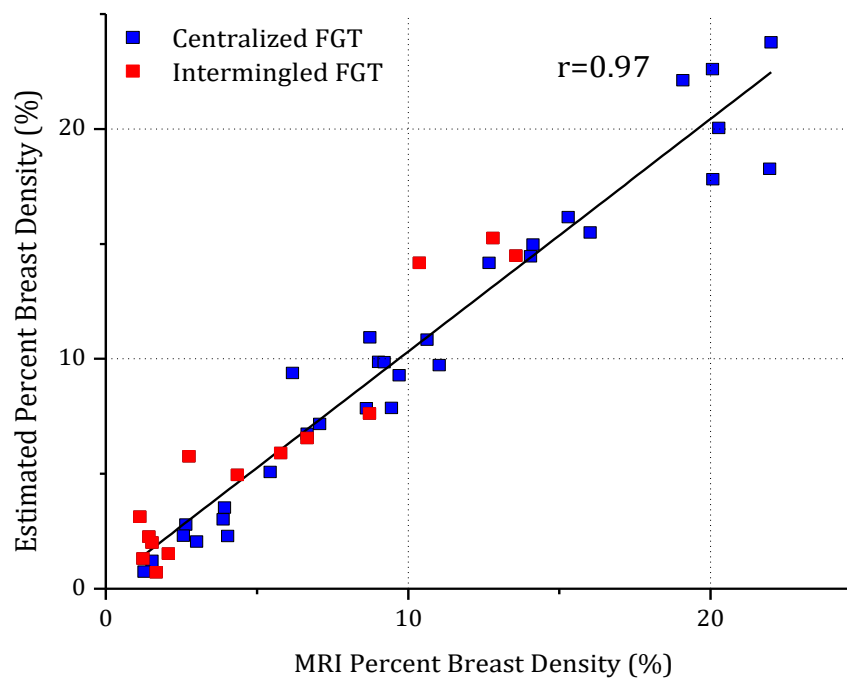


Figure 21. The modified regression model that uses parameters from both water and lipid maps to estimate the %BD shows good agreement with the MRI %BD ($r=0.97$). [103]

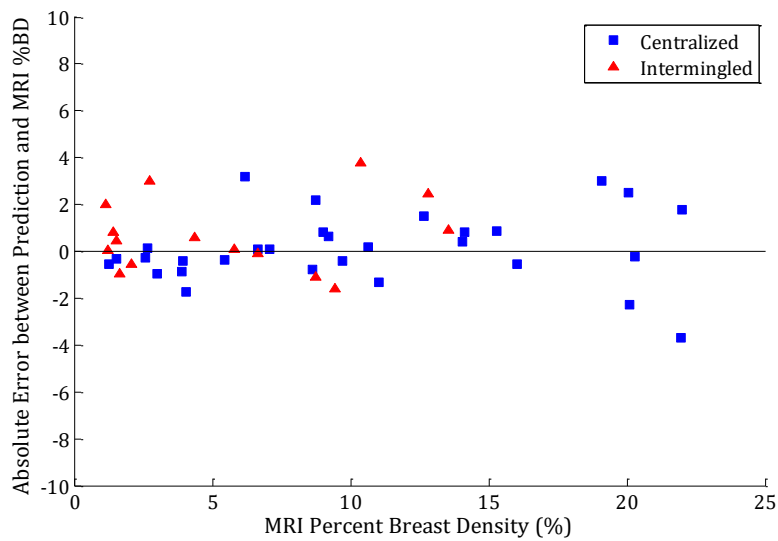


Figure 22. The absolute error between the estimated %BD and the MRI %BD is shown. The horizontal line marks 0, or no, error. The error for all the cases has been reduced compared the first approach and are all well distributed along this line for all the MRI %BDs. [103]

These simulation studies aim to look at the abilities of SL-DOT in imaging breast density. We found that although the exact volume may not be measured accurately for all sizes of the FGT, information encoded in the recovered absorption or chromophore concentration values can be used to correct any inaccurate estimations. Based on these preliminary simulation studies, we understood SL-DOT's capabilities and planned phantom studies to test them experimentally.

Chapter 4: Benchtop instrumentation

Our SL-DOT instrumentation is a horizontal benchtop system that has undergone modifications throughout its development. The main difference in configuration between this technique and traditional DOT is the incorporation of digital micro-mirror devices (DMDs) to spatially modulate the light. Our first iteration was a single-DMD system that projects SL patterns and used a charged-couple device (CCD) camera to collect wide-field images. With this system, the integration of the intensity measurements was performed post-imaging. Our second and current iteration is a dual DMD system where one DMD is used for SL illumination and the other DMD is used to spatially modulate the collection of light. This collected SL is then diverted towards a lens that focuses the light into a PMT to be measured. This chapter discusses the both imaging setups and the LabVIEW software to automate the second system.

4.1 Initial setup: Source DMD & CCD camera

Our first setup consisted of a laser source fiber coupled with a DMD projector and a CCD camera (Figure 23). The DMD projects SL patterns onto a phantom placed in between the light source and the CCD camera. The camera collected images of the opposite side of the phantom for each SL pattern projected. These images showed the spatial distributions of photons that are exiting the phantom. In order to convert these images into SL-DOT measurements, the intensity on the raw images were integrated with the FOI according to the SL patterns. This was done for each source

image, where each SL-DOT measurement is a different combination of the source and detection patterns.

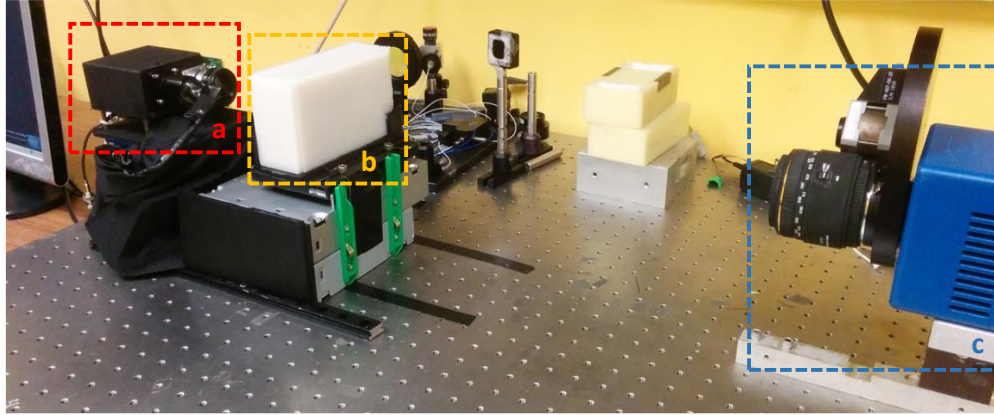


Figure 23. First preliminary setup of the SL-DOT system. A DMD projector coupled with a fiber laser source (a) projects light onto an agar phantom (b) and a CCD camera (c) collected images of the other side.

The schematic of the system is presented in Figure 24. The DMD SL patterns were manually changed using software on the computer. The CCD camera was then controlled using image acquisition software ColdBlue (Perkin Elmer; Waltham, MA).

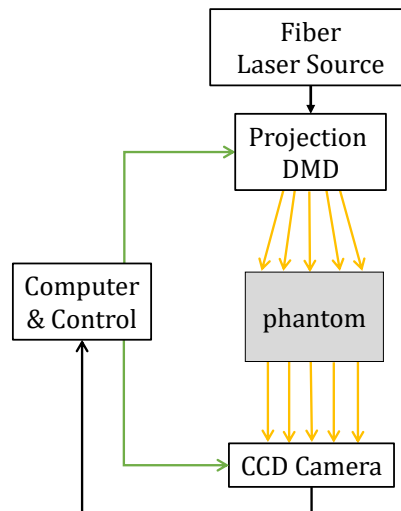


Figure 24. Schematic of the preliminary benchtop system. A computer controls which patterns the DMD projects and the settings of the camera. Images are collected when prompted through the computer.

4.1a. Laser Source Fiber

Two laser diodes, 660nm and 785nm, were used with this system. The wavelength of light used was manually switched by coupling the source fiber directly with the desired laser diode. The other end of the laser fiber is then connected to the DMD projector. The lasers operated in constant-power mode for constant laser intensity output to provide continuous-wave measurements. Because 660nm is in the visible region of light, it was used to mark the FOI of the DMD projector. The source fiber was then disconnected from the 660nm laser and then coupled to the 785nm laser for measurements.

4.1b. CEL-5500 DMD

The source fiber connected to a DMD (DLP-5500, Texas Instruments) that was bought as a repackaged projector with a modular lens system (Compact Embedded Light (CEL)-5500; DLInnovations; Austin, TX) with removable components (Figure 25). The DMD has 1024 by 786 micro-mirrors which spatially modulates the projected light and projects images onto the phantom at the same aspect ratio (1024 x 786).



Figure 25. CEL-5500 DMD projector used to spatially modulate the light source into structured-light patterns.

4.1c. CCD camera

A ColdBlue camera (Perkin Elmer; Waltham, MA) with a Kodak KAF3200ME CCD sensor (cooled to -30°C) was used to capture images of the opposite side of the phantom (Figure 26). Pixels within the images were averaged with 4-by-4 binning, resulting in a final image size of 570 by 382 pixels. A Sigma MACRO 50mm F2.8 lens was attached to the camera with a Nikon F-to-C adapter. A filter wheel is located in between the lens and the CCD sensor and is used in other fluorescence studies; however, in this project, the wheel position with no filter was used to collect light across all wavelengths.

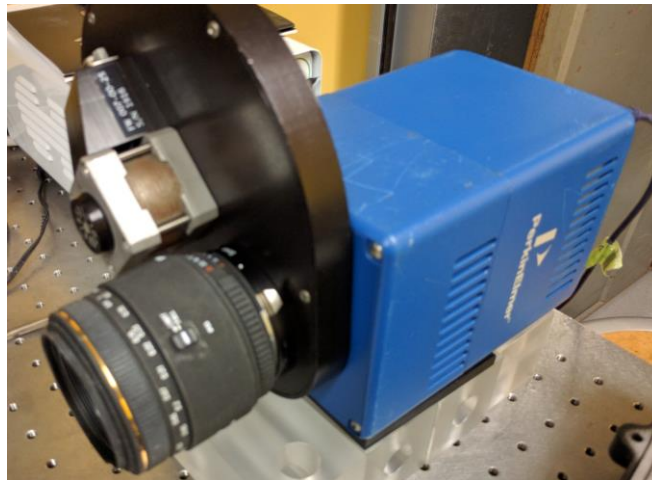


Figure 26. PerkinElmer ColdBlue™ CCD camera. Filter wheel was not used.

4.2 Final Setup: Source DMD & Detection DMD

The current and final version of the instrumentation consists of two separate DMDs: one for SL illumination and one for SL detection. The CEL-5500 that had acted as the source in our previous setup is now coupled with a PMT and serves as the

detector (Figure 27c). A new DMD (DLP-3000; Texas Instruments; Dallas, Texas) is used as a source (Figure 27a).

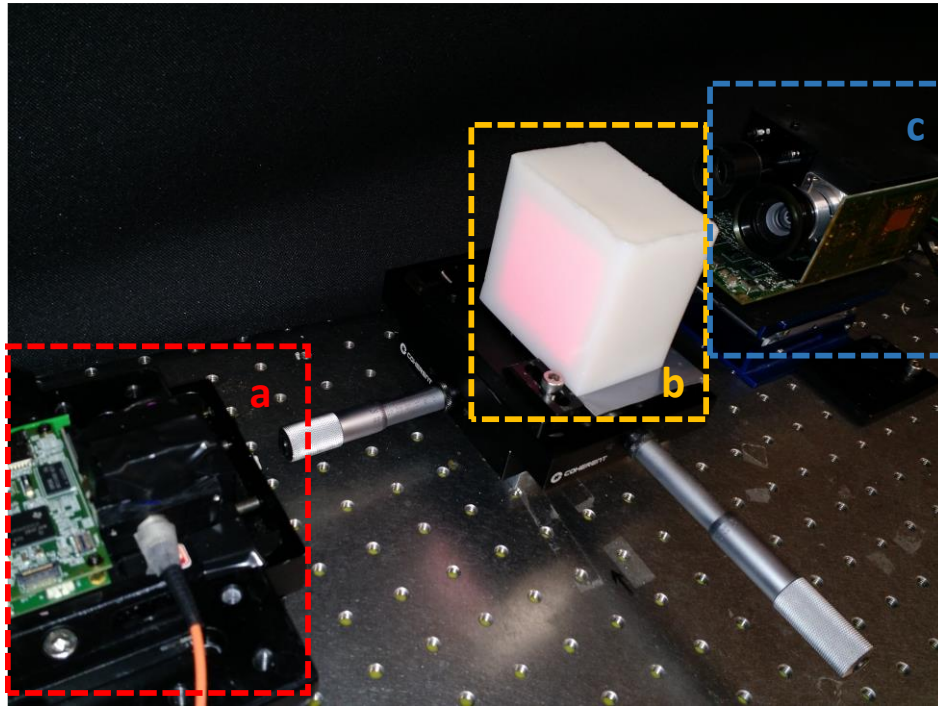


Figure 27. The final benchtop SL-DOT setup. (a) A source DMD coupled with a light source projects SL patterns onto (b) an agar phantom and (c) a second DMD with a PMT collects measurements from the other side.

The instrumentation is now automated through the use of LabVIEW software (Texas Instruments) and a data acquisition (DAQ) card (USB-6009; Texas Instruments). With the analog output of the DAQ card, a voltage (0-3.6V) can be used to apply a high voltage across the PMT (R7400U-01; Hamamatsu; Hamamatsu, Japan) to control its sensitivity to light (Figure 28). Using the digital outputs of the DAQ card, a 5V voltage can be applied across the input terminal of both DMD systems separately (Figure 28). This rising voltage trigger can induce the change of the SL pattern to the next pattern of the stored sequence. The input of the DAQ is then used to collect the current measurement from the PMT through a transimpedance amplifier (PDA-700;

Terahertz Technologies, Inc.; Oriskany, NY) and is converted into a voltage measurement (Figure 28).

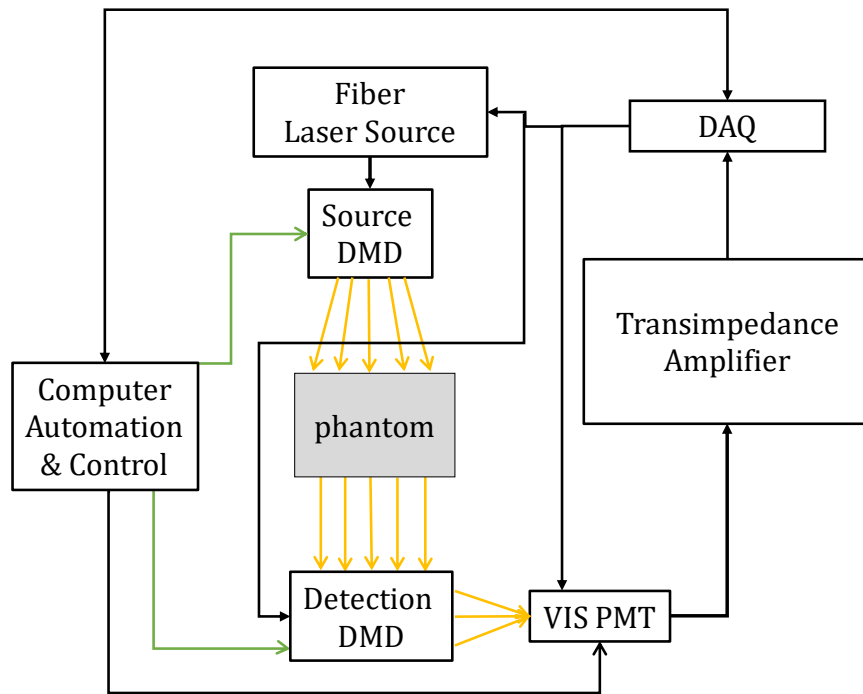


Figure 28. Schematic of the final benchtop system. The source DMD sends light towards a phantom and a detection DMD integrates the signal into a PMT. The current output of the PMT is measured by a transimpedance amplifier that is then measured by a data acquisition card (DAQ) and the computer. The computer controls the DMDs' patterns and controls the sensitivity of the PMT through the DAQ.

4.2a. Laser Source Fiber

With the current system, the number of wavelengths of light that are used increased. In addition to the two previously mentioned laser diodes, two more wavelengths were added: 808nm and 830nm. These lasers also operate in continuous-wave mode. When taking multi-wavelength measurements, the source fiber is connected to a fiber switch which controlled the wavelength of light being projected. The four laser diodes are connected as inputs to the fiber switch. The switch is used instead of directly coupling the source fiber to the laser diode because

the manually detachment and reconnection of the fibers to different laser diodes during an experiment may introduce variability among measurements on different phantoms.

4.2b. Source DMD

The DLP-3000 from Texas Instruments is a DMD-based light projector that has three LEDs (red, green, and blue) for color images. For our study, we use our own fiber-based laser source, so the LEDs were removed from their positions and covered with black tape to prevent illumination onto the DMD. They were not detached completely because the projector circuitry has a feature to shut down the projector if the LEDs overheat. Completely removing the LEDs may result in the projector not functionally if the system does not detect a connection. The laser fiber source is connected to the projector through an adapter made in-lab and is attached where one of the LED sources was originally positioned (Figure 29a-2, b-1). A dichroic filter that was located along the light path was removed. This allows the light from our fiber to freely move towards a lens that diffuses the light onto a mirror, reflecting the light onto the DMD (Figure 29b-2). The DMD then determines which pixels are illuminated and the SL-pattern is projected through the imaging lens (Figure 29b-3). A close-up of the DMD is shown in Figure 29c; although the DMD array looks rectangular, the array is actually 608 by 684 micro-mirrors. Additionally, the projected aspect ratio of the full-screen is 16:9, so care was taken when uploading images to this particular DMD. Patterns were adjusted so that the aspect ratio of our SL-patterns were correctly projected.

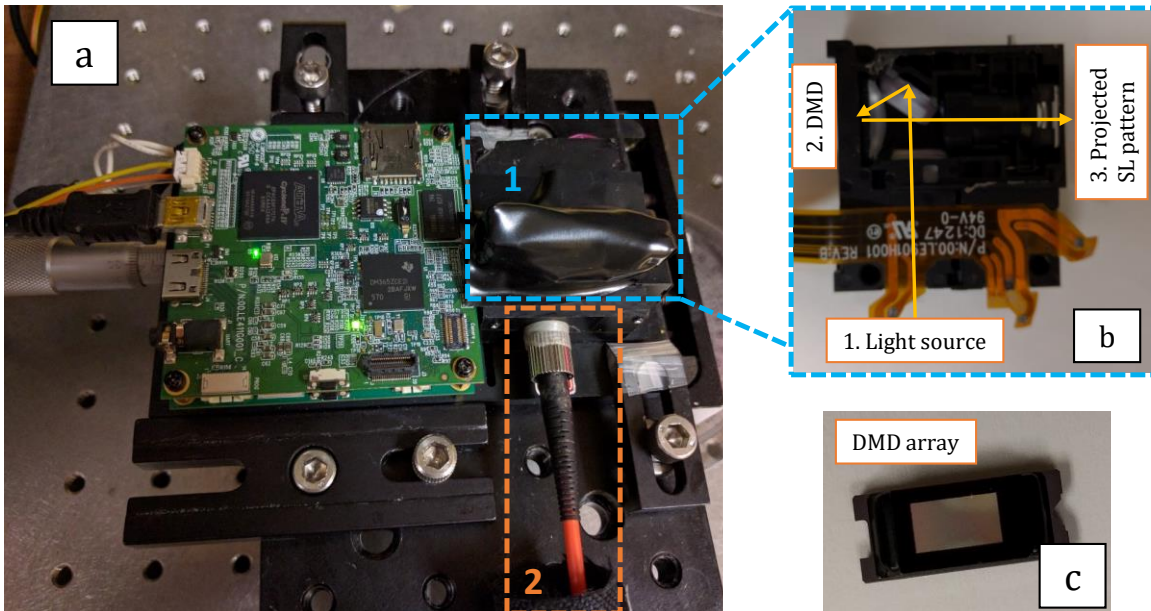


Figure 29. (a-1)The new DMD projector that is coupled with (a-2) a laser fiber source. Looking at (b) the opened projector, (b-1) a light source sends light towards a mirror and lens, which then illuminates (b-2) the DMD. The DMD then controls which pixels are projected, and sends the projected SL-pattern towards (b-3) the imaging lens. (c) A close-up of the DMD behind the lens is also shown.

4.3c. Detector DMD and PMT

The CEL-5500 that was previously used as a source is now used as a detector. Because the components of the projector are modular, we tested different configurations to optimize the collection of light. To be used as a detector, we found that only one piece, the diffuser, needs to be removed. The diffuser's purpose is to diffuse the laser light so that the DMD is illuminated homogeneously. If using the projector to collect light, the diffuser would distort the image before being focused into the PMT. The path of the collected image through a top-down view of the opened CEL-5500 is presented in Figure 30. (1) The imaging lens collects the light, which is sent towards (3) a DMD with the use of (2) a prism. Based on the incident angle, light entering at a 90° angle will be reflected towards the DMD. The DMD then spatially

modulates which parts of the image is collected and reflects that light back towards the prism. Rejected light is reflected away. Because the DMD reflects this light at a 12° angle, this light is then refracted towards (4) a mirror, reflecting this light towards (5) a focusing lens. The focal length of this lens is 25mm; (6) the PMT with a circular active area of 12mm diameter is aptly placed at the focal length to collect all of the focused light. The output of the PMT is connected to a transimpedance amplifier which amplifies the signal even further. Then the output of the transimpedance amplifier is then read by the DAQ.

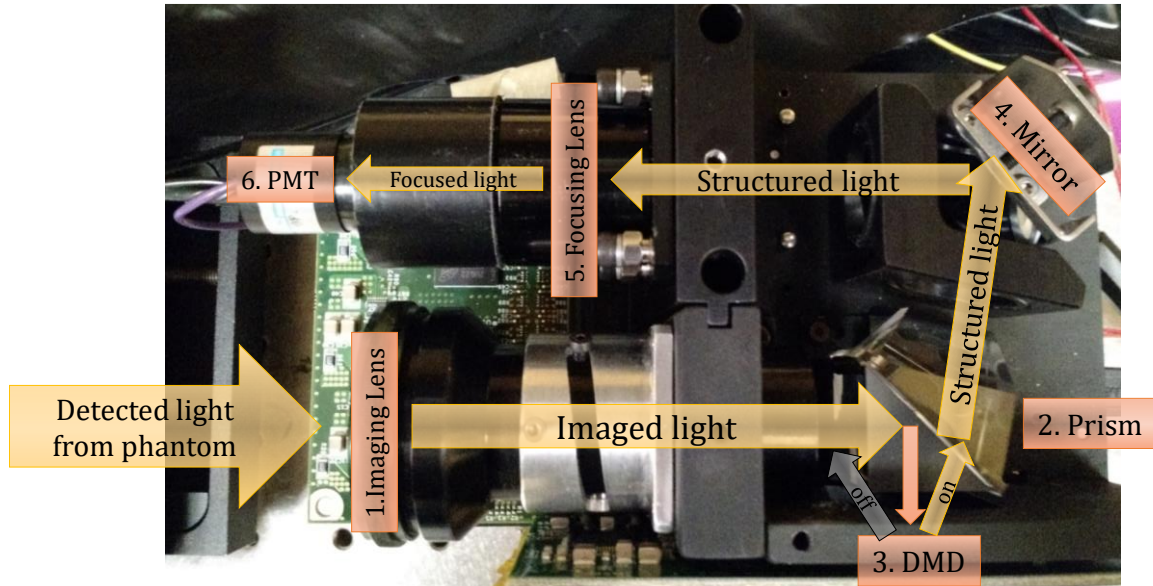


Figure 30. A view of the opened DMD system used for light collection is presented. Light from the agar phantom is collected with (1) the large imaging lens on the bottom left, the image of which is sent towards (2) a prism. Based on the angle of incidence, the prism reflects light towards (3) the DMD, where pixels are used to create the structured-light. The DMD reflects light back towards and passes through the prism, and is send towards (4) a mirror, which reflects the light towards (5) a focusing lens and to (6) the PMT.

We assumed that the light-path would be the same for illumination as it is for detection. We verified this by imaging a photograph (Figure 31a, lower-left) that was placed in front of the projector (Figure 31a). Initially, the 660nm (red) laser source was used in projector-mode to locate the field-of-view (FOV) if the DMD SL-pattern

was a square (Figure 31a). The laser fiber was removed and a photo was taken of the plane where the PMT would be placed (Figure 31b). Magnification of this plane shows that we can see the photograph of interest (Figure 31c). We also verified if the DMD can also spatially modulate the collection of images according to the SL-patterns. An example of this is shown with the checkerboard pattern (Figure 31d). The red laser light is used again to highlight the FOV (Figure 31e) and a magnification of the image plane shows that we only see the portions of the image that correspond to the “on” micro-mirrors of the DMD (Figure 31f). Please note that although the image is reversed at the imaging plane, the DMD is selecting the pixels that are highlighted with the red laser, which will be subsequently integrated into a single intensity measurement. Prior to each experiment, we verify the sequence and orientation of all the SL-patterns to ensure that they match the image reconstruction forward model.

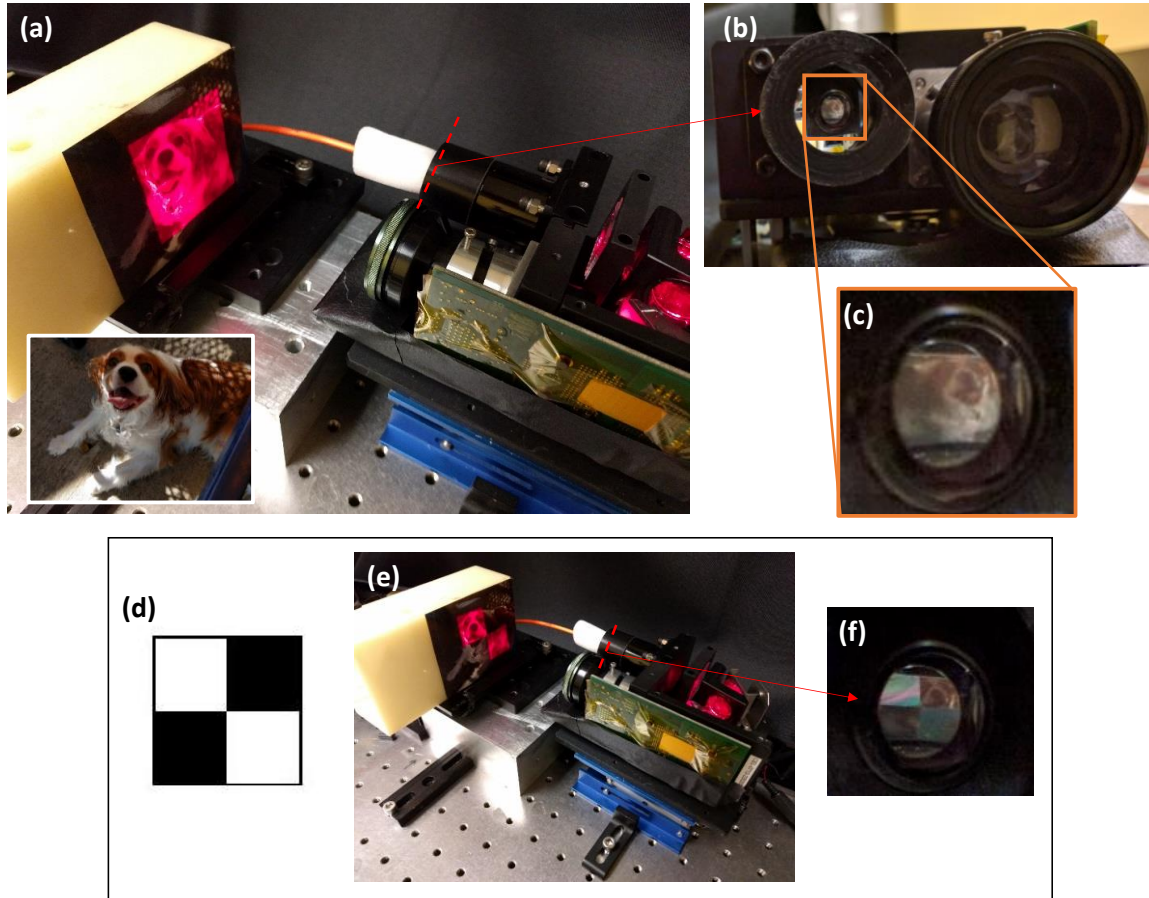


Figure 31. The DMD system used to collect light and images. (a) The red laser light overlay over the image is used to determine where the field of view of the DMD is. Image used for example is shown in lower-right corner of (a). (b) A camera takes an image of the plane where the PMT is positioned (red-dashed line, a). (c) A magnified image shows that the entire FOV can be seen. Please note that the image is reversed due to the lens system, but this is insignificant because all of the signal will be integrated into the PMT. (d-f) Another SL-pattern is demonstrated where only the DMD only reflects part of the image according to the pattern.

The PMT is placed where the laser fiber is normally positioned. As mentioned previously, the DAQ card is used to apply a voltage to a high voltage generator (C4900; Hamamatsu) that controls the sensitivity of the PMT. The maximum voltage that can be applied is 3.6V, which corresponds to 900V across the PMT to accelerate the electrons towards the end terminal to generate a measurement. This sensitivity voltage is always optimized for each pattern set and laser source to maximize the

signals collected by the PMT. The optimization is also performed for each experiment in case of day-to-day changes in the PMT sensitivity. For each pattern set, the source and detector SL pattern combination that produces the highest signal is used to find the PMT voltage that produces a $1\mu\text{A}$ measurement. This is the maximum measurement that is safely recommended for the PMT. The rest of the measurements within a pattern set are taken with the same voltage applied to the PMT.

4.3 Control software for the system

Separate software is used to control both the CEL-5500 and DLP-3000 DMD systems. If performed manually, the software can be used to directly change the SL pattern. Both DMD systems features a voltage trigger where when a rising change in voltage across their terminals results in a change of the pattern. This was used to our advantage and a LabVIEW program was created to automate the changing of SL patterns and measuring PMT signals.

4.3a. CELconductor Control Software

The CEL-5500 can be controlled from the computer using the CELconductor Control Software (DLInnovations). Images of the SL patterns (where white and black represent illuminated and non-illuminated pixels, respectively) can be uploaded and set as a pattern sequence (Figure 32). Patterns can be changed manually through the software, but there is an option to allow for an external 3.3V minimum voltage trigger applied to the CEL-5500 that can change the patterns as well. The DAQ card was used to supply 5V to the terminal located on the DMD driver board.

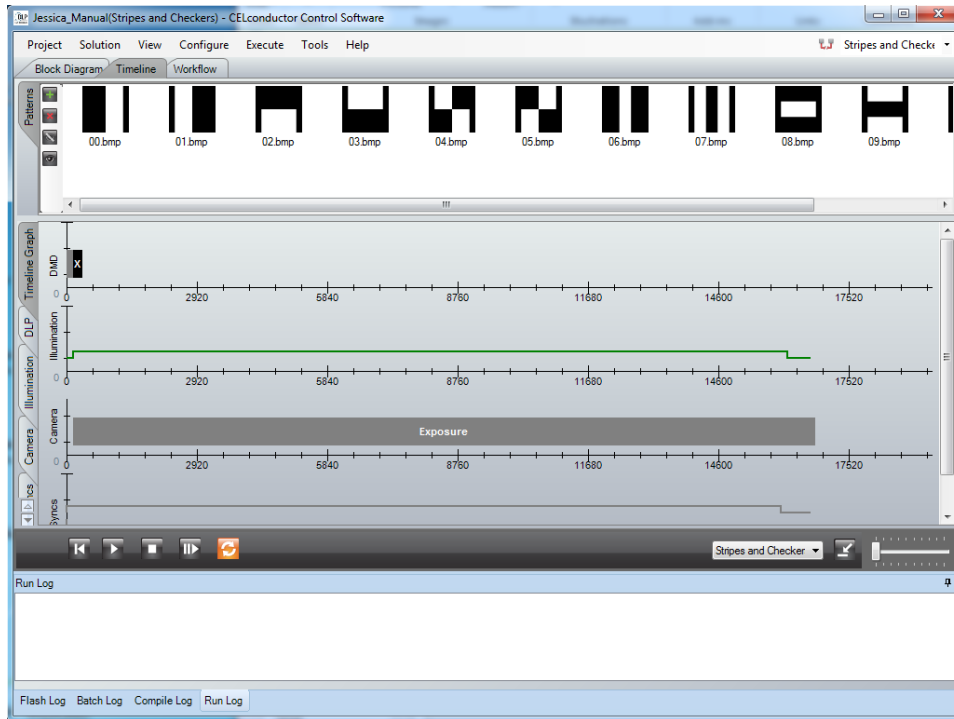


Figure 32. CELconductor Control Software from DLInnovations to control the CEL-5500 DMD system. Software can be used to manually select patterns or store pattern sequences that can be externally triggered.

4.3b. DLP LightCrafter Control Software

The DLP-3000 DMD system is controlled using the DLP LightCrafter Control Software (Texas Instruments). It controls most features of the DMD, including the LED current to adjust the LED power. Although we do not use the LEDs in our studies, we set the current to the minimum (141mA) to reduce the heat produced, prevent overheating and prevent the safety mechanism from shutting down the DMD system. Like the previously mentioned CELconductor software, binary images can be uploaded and manually changed through the user-interface (Figure 33). Images that are uploaded as a pattern sequence can be changed by applying an external 3.3V external trigger to the DMD system. This is done with a 5V output from the DAQ card.

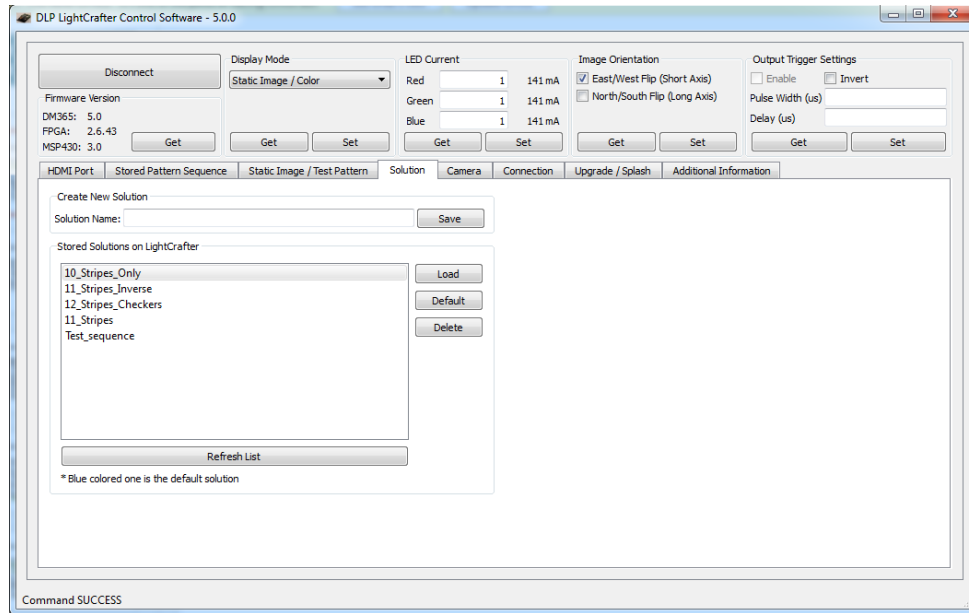


Figure 33. DLP LightCrafter Control Software from Texas Instruments is used to control the DLP-3000 DMD system. The software allows for patterns to be manually selected or can store pattern sequences that can be controlled externally through voltage triggering.

4.4c. LabVIEW control software

A graphical user interface (GUI) was created using LabView (Texas Instruments) to automate cycling through SL patterns and taking PMT measurements (Figure 34). Through the GUI, the user can specify what voltage to supply the PMT to control its sensitivity, the number of source and detector patterns that will be used, the number of samples to average, and the sampling rate of the DAQ card. The individual DMD control software are still required to select the SL pattern sequence and need to be initialized prior to using the LabVIEW GUI.

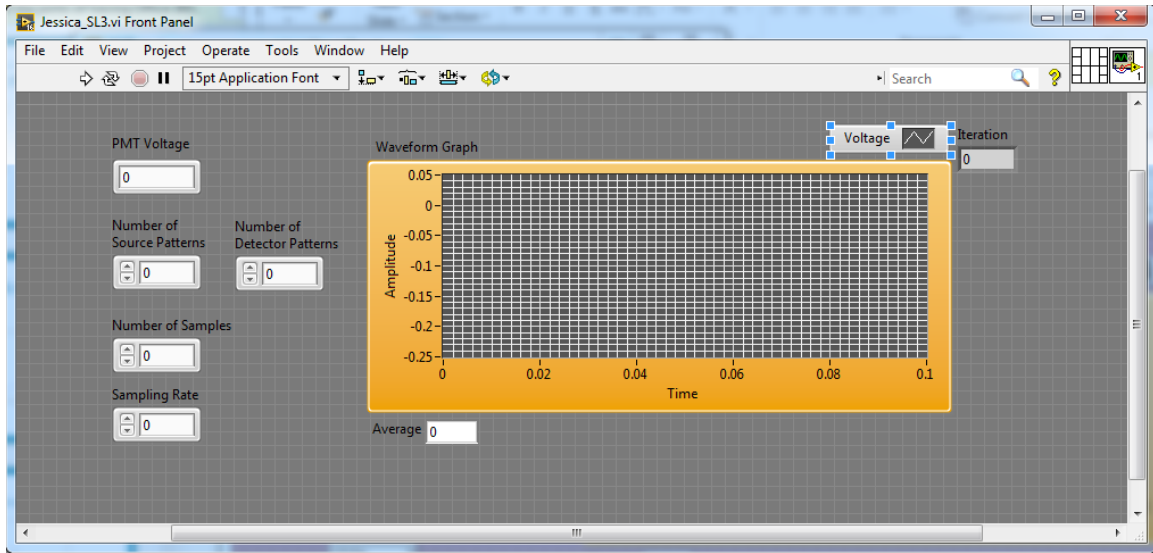


Figure 34. Graphical user interface created in LabVIEW to control the SL-DOT system. Parameters that are inputted include the voltage to apply to the PMT, the number of source and detector patterns, the number of samples to be averaged, and the sampling rate of the DAQ card.

An overview of the program is shown in Figure 35. When executed, a prompt will warn the user that the PMT will turn on to prevent light overexposure to the PMT. Then, the program applies the desired voltage to the PMT to begin taking measurements. The program then applies a 5V voltage to the source DMD, triggering the first source pattern to be projected. A 5V voltage is then applied to the detector DMD to trigger the first detection pattern. The DAQ card will average N number of PMT measurements at X sampling rate, with both N and X specified by the user. The program averages multiple PMT measurements to minimize the error due to fluctuations and obtain a steady signal. This average is then written to an Excel file. The program will loop through all the detections patterns while keeping the source pattern constant. The source pattern is then triggered to change, and the program loops through all the detection patterns again while taking measurements. This

nested loop ensures that all source and detection patterns combinations are measured. The final Excel file will contain an array that is $N_d \cdot N_s$ long, where N_d is the number of detection patterns and N_s is the number of source patterns. Measurements are in {S1-D1, S1-D2, ... S1-D N_d , SN $_s$ -D1, SN $_s$ -D2... SN $_s$ -D N_d } format, which match the format of the forward model of our image reconstruction algorithm.

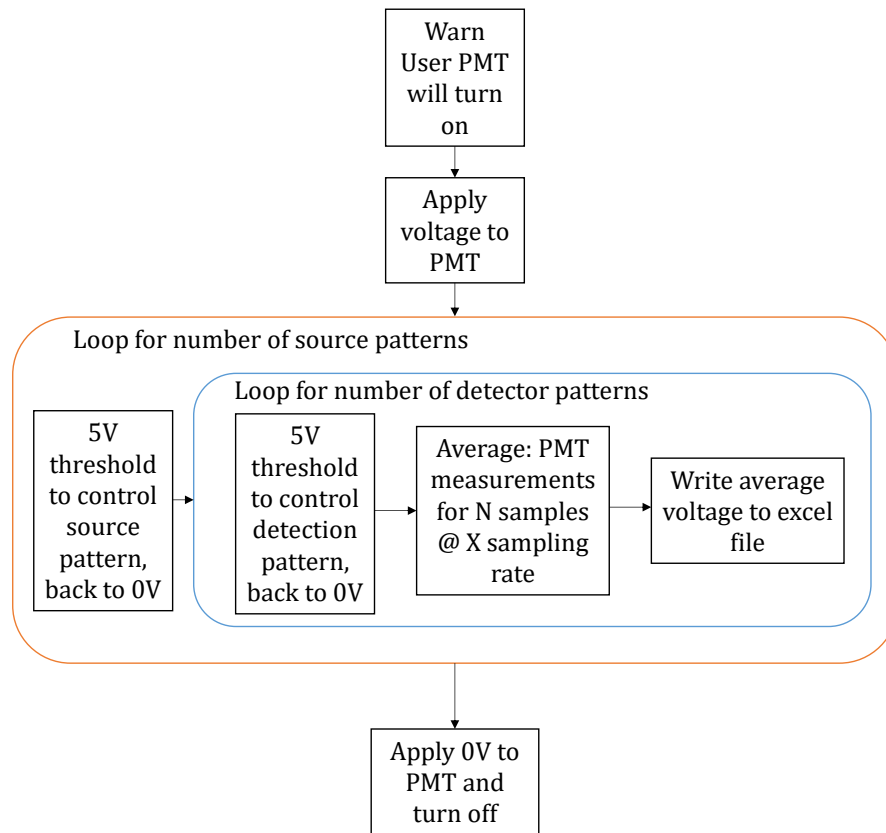


Figure 35. An overview of the LabVIEW code behind the GUI.

Chapter five: Characterizing and optimizing the structured-light DOT system

After completing the final hardware design, we tested and characterized the system. The first was to determine whether our system was stable and that measurements are consistent and reproducible. The second is to ensure that our intensity measurements have high signal-to-noise ratio by evaluating the signals throughout the system. Thirdly, we investigated the effect of averaging on the measurements. And lastly, we wanted to look at optimizing the SL pattern set based on experimental obtained data.

5.1 System stability and measurement reproducibility

5.1a. Stability of measurements over time

Prior to the start of these tests and our experiments, we turned the laser on for at least one hour in order for the temperature, and subsequently the power, of the LED to stabilize. A 60mW 785nm laser was used. Eleven PMT measurements were taken every minute without changing the patterns of the DMDs to check the stability over a short period of time (Figure 36a). The SL pattern that was used was a full-square illumination that was 5mm by 5mm and centered on the phantom. The PMT voltage was set to 2.25V to optimize the signals collected. The sampling rate of the DAQ card is 10kHz and 1,000 samples were averaged to for the final measurement. Measurements were taken using a homogeneous epoxy phantom made with India ink as an absorbing agent and TiO₂ as the scattering agent. The dimensions of the

phantom are $42 \times 110 \times 70 \text{mm}^3$. This solid phantom is very stable and optical properties will not change within the short time period of the measurements. For our purposes, a stable system is defined as having a standard deviation less than 1%. The mean of these eleven measurements is $0.9083 \mu\text{A}$; the standard deviation is $0.0077 \mu\text{A}$ which is 0.85% of the mean.

A second test took six measurements were taken every five minutes without changing patterns (Figure 36b). This timing is comparable to the length of our multi-phantom experiments where each phantom is imaged for 1-2 minutes for each wavelength of light. The settings of these measurements were the same as the first test where 1,000 samples were averaged and collected at a 10kHz sampling rate. Measurements were also performed on the same solid epoxy phantom. The mean of these measurements is $0.9199 \mu\text{A}$ with a standard deviation of $0.0035 \mu\text{A}$ (0.38% of mean).

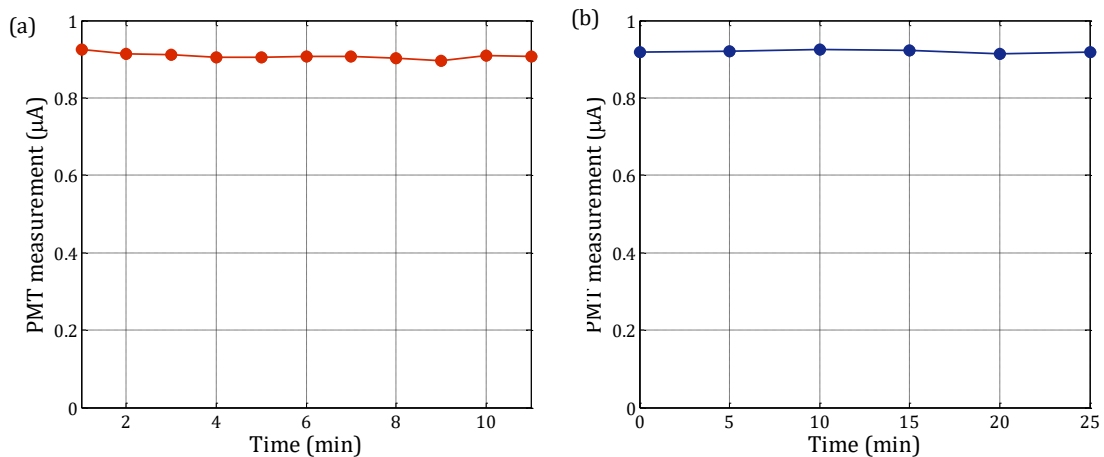


Figure 36. (a) Single intensity measurements taken every minute and (b) every five minutes to test the system's stability over time. The mean of the measurements taken every minute is $0.9083 \mu\text{A}$ with a standard deviation of $0.0077 \mu\text{A}$. The mean of the measurements taken every five minutes is $0.9199 \mu\text{A}$ with a standard deviation of $0.0035 \mu\text{A}$. In both cases, the standard deviation is less than 1% of the mean, which is acceptable for our imaging studies.

5.1b. Reproducibility of measurements over time

Our final test took measurements using an entire pattern set. With 12 patterns for both the source and detection, 144 intensity measurements were taken every 30 minutes for four hours. With a sampling rate of 10kHz and 1,000 sample number, this measurement set was acquired in less than 30 seconds. To test the reproducibility of these results, we used pair-wise intra-correlation coefficient (ICC) analysis in comparing the absolute values of the measurements over time. All pair-wise comparisons yielded a $p \ll 0.01$. A visualization of the correlation between two time points show high fidelity between the two sets of measurements ($r = 0.98$, Figure 37).

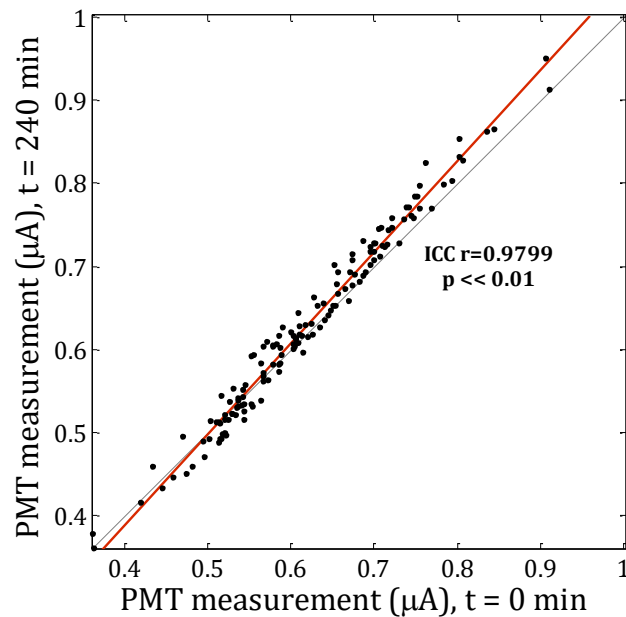


Figure 37. Scatter plot of the 144 measurement set at $t = 0\text{min}$ and $t = 240\text{min}$ to visualize the correlation between the two. ICC analysis yielded a $r = 0.9799$ with a $p \ll 0.01$ for this particular pair-wise comparison.

5.2 Signal levels and signal-to-noise ratio

A common goal when developing all types of imaging systems is achieving high signal-to-noise ratio (SNR). In order to extract the correct information from a

measurement, the signal must be much higher than the noise. Our SL-DOT system was evaluated for performance and compared to simulations of a traditional DOT point source and detector. Additionally, various number of samples collected by the DAQ card and averaged were tested to note its effect on the SNR.

5.2a. Signal evaluation throughout system

Using a power meter, the power of the laser was measured to be 61mW (Figure 38a). It was found that there are points within the system that contribute to the loss of photons, thus lowering our recovered signal. With the laser inserted into the source DMD, the power meter was used again to measure the power of a projected 45mm x 45mm square: 7.8mW. Thus, the efficiency of the source DMD is 0.128 (Figure 38b). Using the simulation of a 53mm thick phantom with optical properties of 0.0066mm^{-1} and 0.645mm^{-1} for absorption and scattering, respectively, the fraction of the incident light that is detected is 5×10^{-4} (Figure 38c). Like the source DMD, a power meter was used to compare the input laser power to the output for the detector DMD. The detected power was 16mW compared to the initial 61mW laser source, making the efficiency of the second DMD 0.262 (Figure 38d). We assume that the loss seen from using the second DMD as a source is similar to using the second DMD as a detector because the lens system is unchanged except the diffuser is removed. With this particular phantom, we calculate that the amount of light that reaches the PMT is a 1.68×10^{-5} fraction of the original laser source's power.

Power loss through SL-DOT system

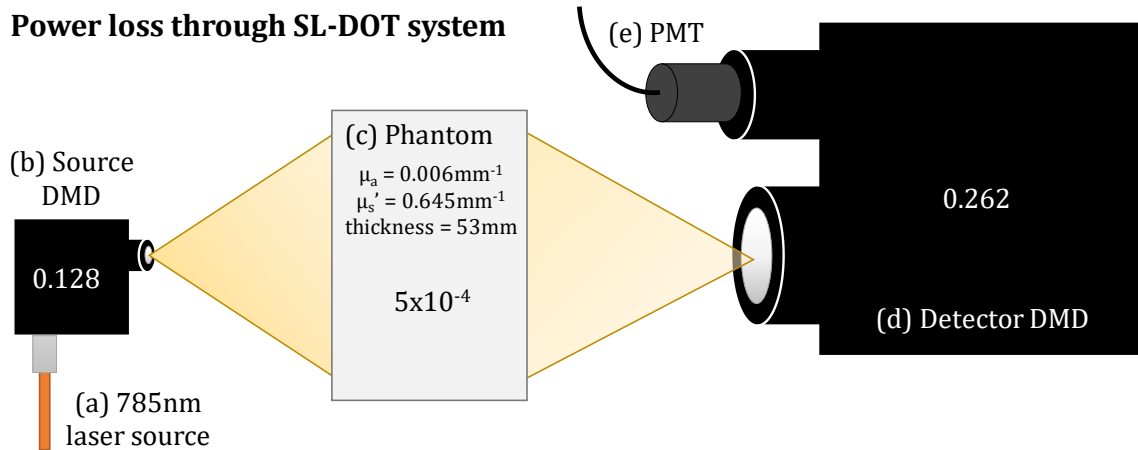


Figure 38. Illustration of points of power loss throughout system. Beginning from the initial laser fiber power (a), 0.128 of the fiber power is transmitted through the source DMD (b). Based on a simulation with a 53mm thick phantom (c), the detected flux is 5×10^{-4} of the incident light. This light then goes through another drop in power while being collected by the detector DMD (d), where only 0.262 of the collected light reaches the PMT (e).

A similar analysis was performed with a traditional point source and point detector configuration that is commonly used DOT. Based on a simulation where a laser source was centered on one side of the phantom and a PMT was centered directly across the source on the other side, only a 9.25×10^{-5} fraction of the initial source power is detected (Figure 39).

Power loss through DOT system

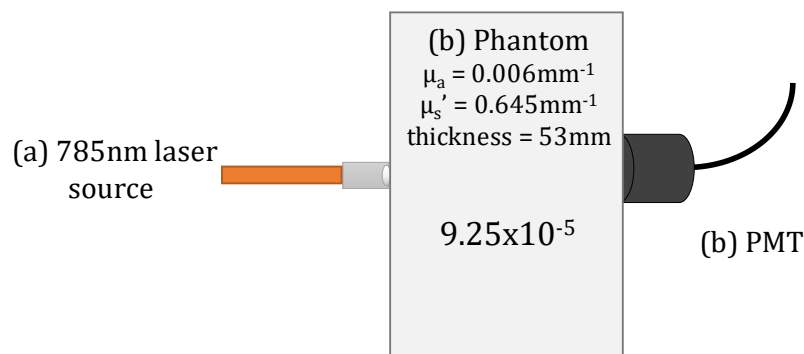


Figure 39. The loss of power in a traditional contact DOT transmission-mode point source (a) and point detector (c) is illustrated. The main loss of photons is from the phantom (b).

To discuss the overall system's efficiency in detecting the light, we need to understand the PMT's spectral response and signal amplification. At 785nm, the spectral response of the R7400U-01 model is 2mA/W, meaning it produces 2mA for every 1W that is detected. Additionally, the PMT's sensitivity can be controlled by applying a voltage from 0 to 3.6V to the high voltage generator. This applies an even larger voltage across the PMT, amplifying the signal exponentially. For example, applying the full 3.6V to the high voltage generator results in 900V across the PMT, corresponding in a 10^6 fold gain. Despite the large loss of light across the SL-DOT system, the use of a PMT can recover extremely low levels of light.

For example, the amount of light that can be detected by the traditional DOT system in Figure 39 can be calculated to show the typical light levels that can be expected. Given that the safety limit of a continuous-wave 700-1400nm laser light intensity illuminated onto skin is approximately $3\text{mW}/\text{mm}^2$, we set the laser power to 2mW over a 1mm^2 area on the phantom. The detected flux at the position of the PMT would be $1.85 \times 10^{-4}\text{mW}$. The PMT will then convert this power into $3.70 \times 10^{-7}\text{mA}$ and with maximum gain, the measured current would be 0.370mA, or 370 μA . This is well above the inherent noise of the PMT at 900V, which is typically 1-1.6nA. Additionally, this is well above the maximum limit of the PMT of $1\mu\text{A}$ and the gain would be lowered in this scenario.

The next example will calculate the typical light levels for our SL-DOT system. The laser power will be set to 2mW again, but because we are using SL patterns, this power is distributed over an area of $2,025\text{mm}^2$, making the intensity at the surface of the phantom $9.9 \times 10^{-4}\text{mW}/\text{mm}^2$. This is well below the safety limit of laser light onto

the skin. After going through the SL-DOT system, the amount of light that reaches the PMT detector is $5.03 \times 10^{-5} \text{mW}$. After signal amplification, the measured PMT current is $67 \mu\text{A}$. This may be lower than the traditional DOT measurement, but it is important to note that is still above the maximum limit ($1 \mu\text{A}$) and that the laser intensity is also much lower than the safety standard. If a 60mW source was used, the measured PMT signal would be $2000 \mu\text{A}$, even higher than the measurement in the traditional DOT system.

The SL pattern for both the source and detection is $45 \times 45 \text{mm}^2$ square in the previous case, but a smaller SL pattern was also analyzed. A $9 \times 45 \text{mm}^2$ vertical stripe was used for both the source and detection. If the source and detection was placed as far from each other as possible, the longer pathlength of the traveling photons would result in a very low signal of detected light (Figure 40). The amount of light that transmits through the phantom is a 4.59×10^{-5} fraction of the incident light (Figure 40). With a 2mW laser source, the amount of light that reaches the PMT is $1.25 \times 10^{-7} \text{mW}$. With 10^6 fold amplification, the measured PMT current is $0.25 \mu\text{A}$, which is still a strong signal in comparison to the 1.6nA noise. A key advantage to the SL-DOT system is the distribution of the laser light over large area when forming the SL patterns. Because the 2mW laser source distributed among a large area, the intensity of the incident light is well below the safety limit of $3 \text{mW}/\text{mm}^2$. As we saw, an increase in the laser power greatly improves the signal while still remaining below the safety limit.

Power loss through SL-DOT system: Smaller SL patterns

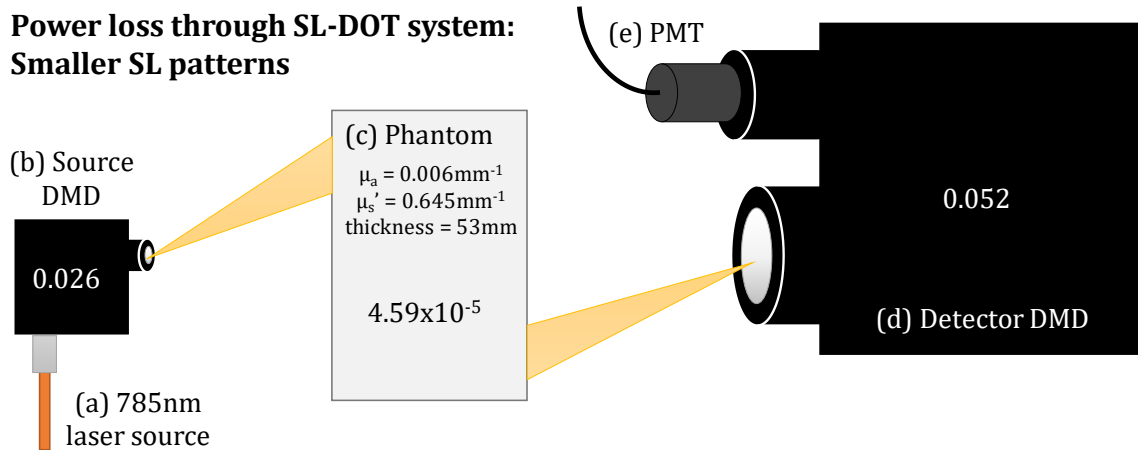


Figure 40. Illustration of points of power loss throughout system using smaller SL patterns. Beginning from the initial laser fiber power (a), 0.026 of the fiber power is transmitted through the source DMD (b). Based on a simulation with a 53mm thick phantom (c), the detected flux is 4.59×10^{-5} of the incident light. This light then goes through another drop in power while being collected by the detector DMD (d), where only 0.052 of the collected light reaches the PMT (e).

5.2a. Number of samples to average

Readings from the PMT are collected by the DAQ and averaged in order to obtain a more accurate measurement. To minimize data acquisition time, the sampling rate of DAQ was set to the maximum limit of 10kHz. The number of PMT measurements should also be minimized to reduce acquisition time, but should also be enough to achieve an accurate measurement. Using the solid epoxy phantom, the number of measurements to be averaged were tested: 10, 100, 1000, 10000 and 100000 samples. With 10 samples, one pattern combination is measured in 1ms; with 100000 samples, one pattern combination is measured in 10sec. Measurements were taken with 560V applied across the PMT, resulting in a PMT noise of 0.16nA. The measurements are approximately 0.9 μ A consistently, well above the noise level (Figure 41a). The SNR for all sample numbers is relatively similar and very high, close to a SNR of 7000 (Figure 41b). For the majority of experiments performed, the

number of readings that was averaged is 1000 samples, corresponding to 100ms spent for a single source-detector measurement.

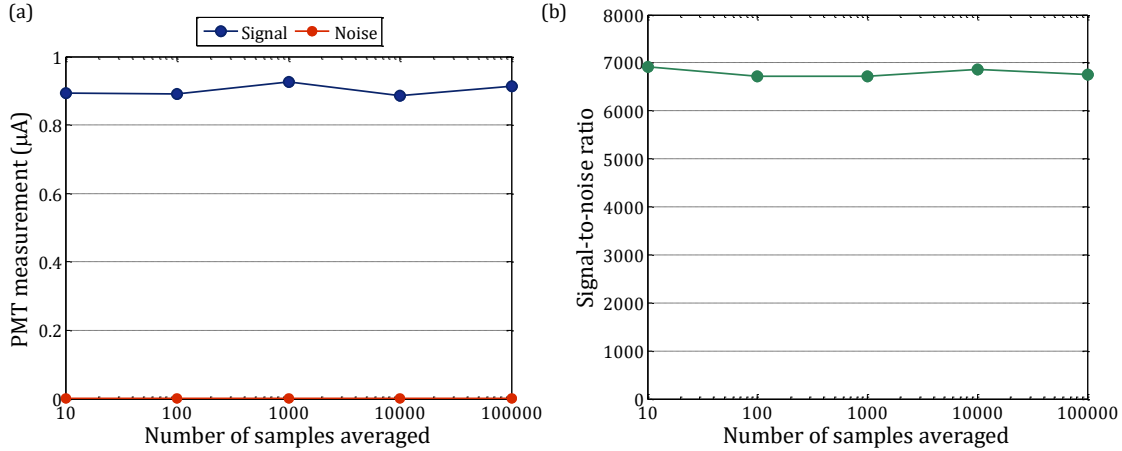


Figure 41. (a) The signal (blue) and noise (red) levels and (b) the SNR of measurements collected with a different number of averaged samples. Measurements were taken on a solid epoxy phantom with 560V applied to the phantom, with corresponds to a PMT dark current of 0.16nA.

5.3 Structured-light pattern optimization

In SL-DOT, arbitrary patterns of light can be illuminated and detected from the object of interest. The choice of which SL-patterns to use may seem daunting where there can be an infinite number of patterns. Another consideration is the number of patterns to use, though more patterns requires more time to acquire data. In our study, we experiment with two SL-pattern sets: large stripes with checkerboards (12, patterns, Figure 42a) and smaller horizontal and vertical stripes (10 patterns, Figure 42c). The experiment consisted of taking measurements on a $53 \times 77 \times 77 \text{mm}^3$ agar phantom with a cubic inclusion centered within the volume. The volume of the inclusion is 10% of the phantom's total volume. After image reconstruction, the recovered absorption maps were segmented at half-max of the recovered range

(Figure 42b,d). The segmented volumes were 10.32% for pattern set # 1 and 10.35% for pattern set # 2.

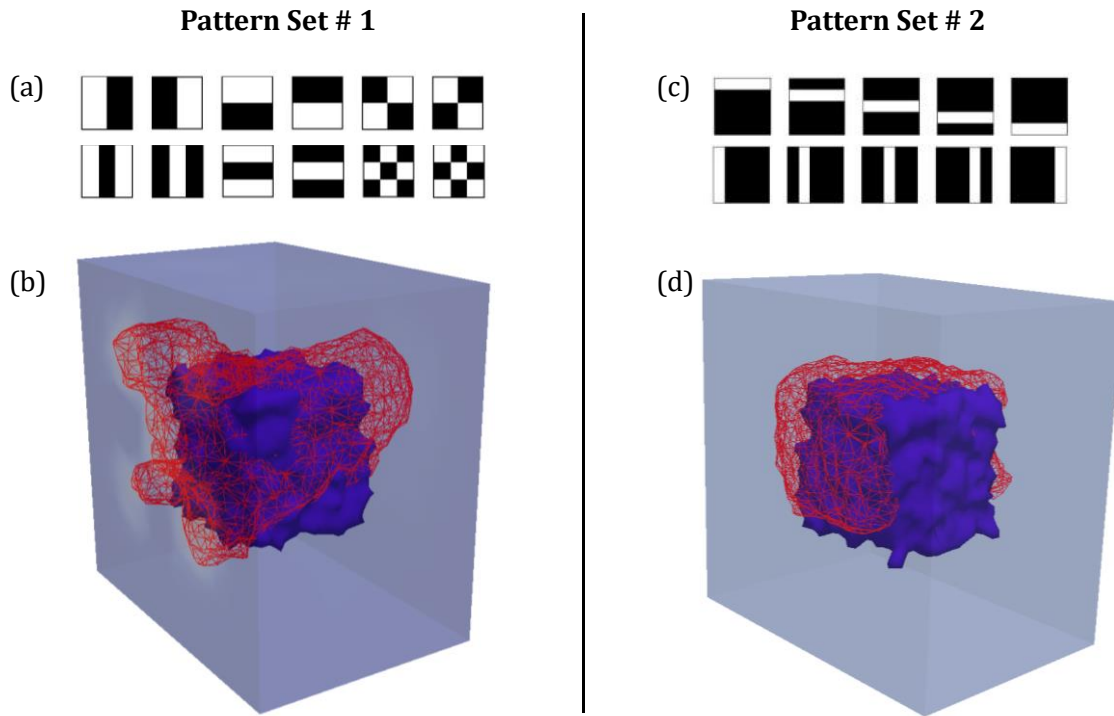


Figure 42. Reconstructions (b, d) from using (a) pattern set # 1 and (c) pattern set # 2 as SL-patterns to collect measurements from a phantom with an inclusion that is 10% of the phantom’s volume. The red wireframe represents the reconstructed volume segmented at half-max and the blue isosurface represents the inclusion.

Although both are very similar to the true inclusion volume, the reconstructed shape using the first pattern set is unusual (Figure 42b). When looking at a reconstruction slice close to the detection side of the phantom, the area of high absorption is similar to the last checkerboard pattern in set # 1 (Figure 43). This “artifact” may be due to this particular SL-pattern’s relatively larger surface area. The sensitivity matrix (the Jacobian) that is formed for this pattern set may be highly influenced by the checkerboard pattern because the convolution with this pattern and the others is much higher. The SL patterns in set # 2 are all the same area of illumination, but with different positions. Because of this, the Jacobian is more

balanced and the reconstructed volume resembles the cubic inclusion. Therefore, pattern set # 2 is chosen for our experimental studies.

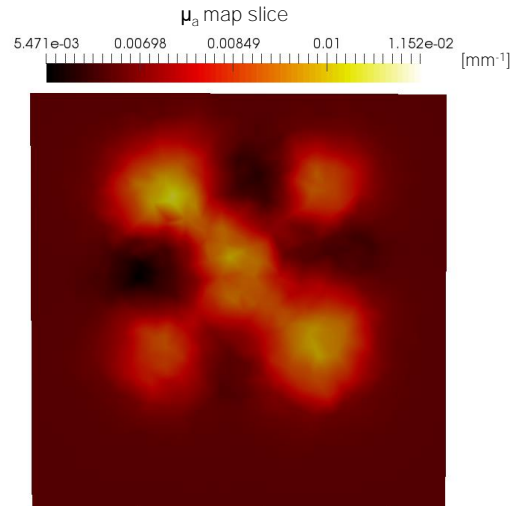


Figure 43. Absorption map slice that was reconstructed from measurements using pattern set # 1. Slice is positioned at 5mm before the detection surface. The areas of high absorption match the appearance of the last pattern in pattern set # 1.

This simple comparison between the two pattern sets showed that consideration is needed when choosing SL patterns. Because the patterns can be arbitrary, it would be very tedious to test many different sets. Additionally, patterns do not need to be binary; DMDs are capable of grayscale imaging where 8-bit SL-patterns with gradients can be formed. This technique is already being implemented in Spatial Frequency Domain Imaging, where sinusoidal gradients of light are projected onto an object [107,108]. In our case, the simpler pattern set performed better in terms of reconstructed a volume most similar in shape to the actual inclusion. Overly complex pattern sets may not perform well experimentally, but further studies are needed.

It is also important to note that the size of these SL patterns affect the shape of the Jacobian, which describes the influence of measurements on the photon density of the internal nodes. The shape, or region of high sensitivity, of the Jacobian is determined by the source and detection patterns used. When larger SL patterns are used, a larger portion of the volume is influenced and the region of sensitivity also becomes larger. This can be thought of as the region in which the photons have most likely traveled through and have influenced. In tomography, this larger Jacobian shape will decrease the resolution of the imaging system because it becomes more difficult to determine the exact path of the detected photons. For example, in computed tomography, x-rays travel in a relatively straight path through the body with very little scattering. The influence of that x-ray is small and narrow compared to the whole volume; therefore, the shape of the sensitivity matrix is small and the image resolution of the recovered attenuation coefficients is higher. SL-DOT's larger Jacobian shape result in a low-resolution imaging system. One solution for SL-DOT to obtain higher resolution is to reduce the size of the SL patterns; however, this results in less signal being detected. The optimal pattern set should have appropriately large SL patterns for high signal collect but not excessively large to avoid vastly lowering the resolution of the system. The clinical goal of SL-DOT is to image fibroglandular tissue, which is generally large pieces of tissue within the breast. SL-DOT may be sufficient in accomplishing this goal.

Chapter six: Phantom studies

Our main goal is to develop a SL-DOT system that can be used to measure the amount of fibroglandular tissue and the hemoglobin concentration within the breast. Through a series of phantom studies, we test our system's capabilities in measuring inclusions of varying sizes. Additionally, we varied the size of the inclusion while using the two NIR dyes in order to recover dye concentration, which may be influenced by the inclusion size. In this study, the goal was to confirm the size-dependency of the recovered concentrations. Lastly, we performed phantom studies where the inclusions had varying amounts of NIR dye concentration from the background, forming different levels of absorption contrast. This is the mimic the varying levels of hemoglobin within the breast among different patients. Prior to the discussion of these phantom studies, we will describe the creation of the phantoms.

6.1 Agar phantoms creation

In order to test the performance of an optical imaging system, phantoms with known optical properties are used. Phantoms can be made from different materials, each with their own advantages and disadvantages. Agar is used because it is relatively quick and easy to make, has a refractive index similar to biological tissue, and can be layered in order to create enclosed inclusions. The process by which agar phantoms are made involves the heating of the agar solution and adding absorption and scattering agents to manipulate the optical properties. The timing of this process is key to formulating consistent and reliable phantoms. Once made, the phantoms can

be imaged for several days but must remain refrigerated to minimize shrinkage and mold growth.

6.1a. Creation of agar mixture

The formulation of the phantoms is 2% agar by weight. Agar powder (RM-301; HiMedia; Mumbai, India) is dissolved in deionized water by heating the mixture to 95°C on a hot plate stirrer. Once fully dissolved, the agar is moved to a regular stirring plate where it is cooled. When the mixture reaches 50°C, India ink is added to act as the absorbing agent in our phantoms. The relationship between the amount of India ink added and the absorption is linear and has been characterized with a spectrophotometer (USB2000; Ocean Optics; Dunedin, Florida). Two characterization studies were performed six months apart and showed that India ink's absorption properties are extremely stable. Furthermore, the absorption of India ink is relatively constant across the NIR spectrum. In addition, 10% Intralipid® (Fresenius Kabi; Uppsala, Sweden) is added to the mixture to act as a scattering agent. The solution continues to be stirred for several minutes before being poured into a mold and placed in a refrigerator for rapid cooling.

In the case of creating heterogeneous phantoms with inclusions of different optical properties, the phantoms are created through layers. The inclusion mixture is created first and placed in the refrigerator until completely solid. The solid mixture is then cut and shaped into the desired inclusion size. The background mixture of different optical properties is then made in bulk. The bottom layer of the mold is filled and allowed to solidify in the refrigerator (approximately 20-25 minutes) (Figure 44b). The remaining background mixture continues to be stirred to prevent

solidification. Once the bottom layer is solid, the inclusion is centered on top of the first layer and the remaining background mixture is poured on top, encasing the inclusion within the phantom volume (Figure 44c-d). The fully finished phantom is then placed inside of the refrigerator to be cooled for at least 2 hours to ensure that the phantom is fully solid. For the majority of our experiments, phantoms are imaged the following day.

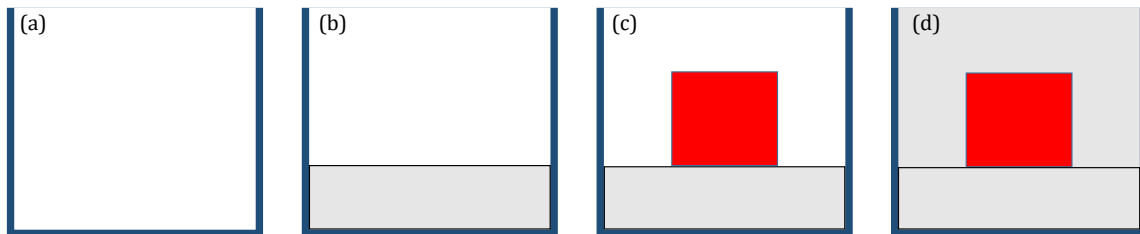


Figure 44. (a) An agar phantom with enclosed inclusions is made through layering the agar mixture into a mold. (b) A bottom layer in gray is allowed to solidify and (c) the inclusion (red) is centered on top. (d) Agar is then poured on top (gray) of the inclusion to encase it in the center.

6.1b. NIR absorbing dyes

As previously mentioned, the absorption of India ink across the NIR region is constant, making it unsuitable for collecting multi-wavelength measurements and recovering chromophore concentrations. Two NIR absorbing dyes, NIR782E and NIR869A (QCR Solutions; Port St. Lucie, Florida), are used (Figure 45). Each dye has a unique absorption spectrum in the NIR region, where NIR782E peaks at 782nm and NIR869A peaks at 869nm. The wavelength at which their spectra cross (isobestic point) is 801nm, which is similar to the isobestic point of oxy- and deoxyhemoglobin: 808nm. Both of these dyes are added to the agar mixture to act as the absorbing agent. By taking multi-wavelength measurements of the phantoms, we can recover the amount of dye that was added to the agar mixture.

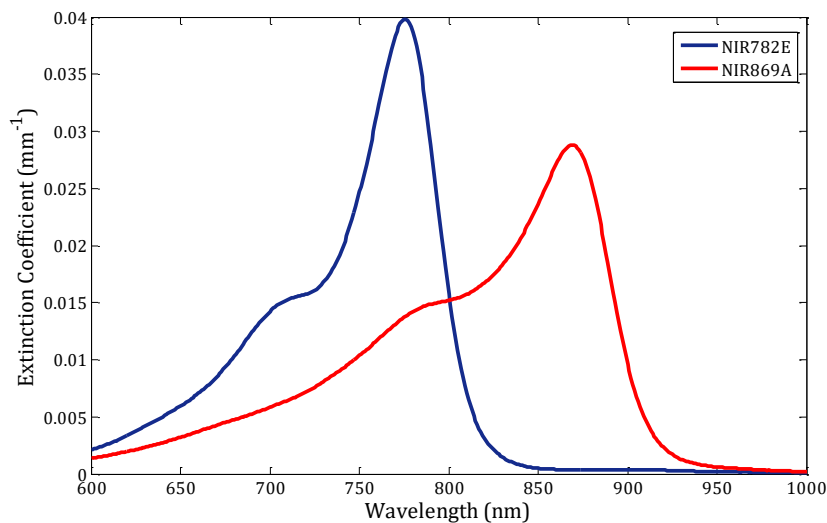


Figure 45. Absorption spectrum of two dyes, NIR782E and NIR869A, in the near infrared region. Their isobestic point (where the absorption is the same for both dyes) is 801nm.

These NIR dyes are stored as a powder for stability. To prepare the dye for the agar mixture, water is added. The absorption of the aqueous dye solution is then characterized using a spectrophotometer and appropriately diluted to obtain the desired optical properties within the phantom. It is important to note that the absorption of these dyes deteriorate over time. Since measurements immediately after the phantom has solidified is not always possible, we monitored the decrease in absorption over time of the original stock solution that was used and assumed that the absorption loss within the phantom was similar. We measured the decay in both dyes' absorption over a span of six days (Figure 46). After six days, the absorption of NIR782E has dropped about 50% while NIR869A's absorption drops to 50% after four days. For this reason, measurements should be performed as soon as possible after the creation of the phantom with these dyes.

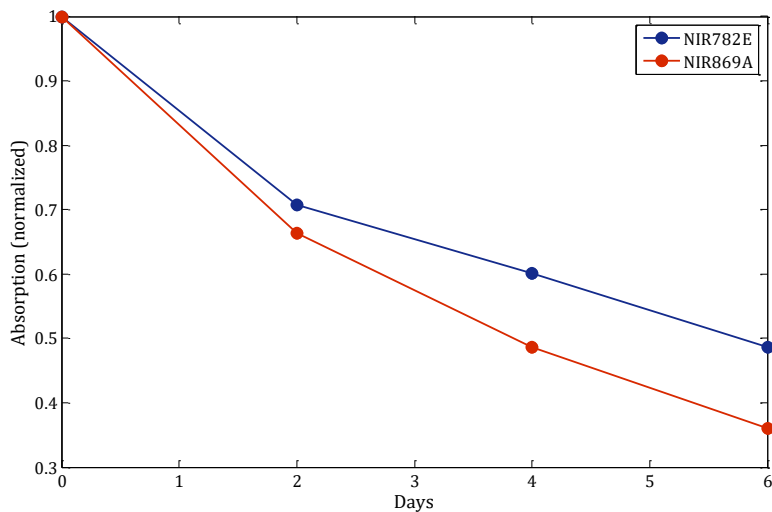


Figure 46. Decay of the NIR782E (blue) and NIR869A (red) dyes over 6 days. Day 0 is the day the aqueous dye solution was created. Absorption measurements are taken at each dye's peak absorption (782nm and 869nm, respectively) and normalized to Day 0's measurement.

6.2 Size-dependency of recovering inclusion volume and absorption coefficients

Because we are interested in recovering volumetric breast density information, we performed a study where we imaged different inclusion sizes within a phantom. Agar phantoms with enclosed inclusions (1, 5, 10% by volume) were made and measurements were performed at one wavelength: 808nm. We are interested in reconstructing the absorption maps of these phantoms and segmenting the absorption maps to measure a volume. Because we saw a size-dependency of the recovered chromophore concentrations in the simulation studies, we expect that there will be a similar relationship between the inclusion size and the recovered absorption.

6.2a. Phantoms

Four agar phantoms with a dimension size of $53 \times 77 \times 77 \text{ mm}^3$ were created. One phantom had homogeneous optical properties to act as a calibration for our image reconstruction algorithm. The remaining three phantoms had inclusion sizes that represented 1, 5, and 10% of the phantom's total volume (Figure 47). The exact dimensions of the inclusions are presented in Table 4. The inclusions are of the same thickness and each is centered within their own phantom.

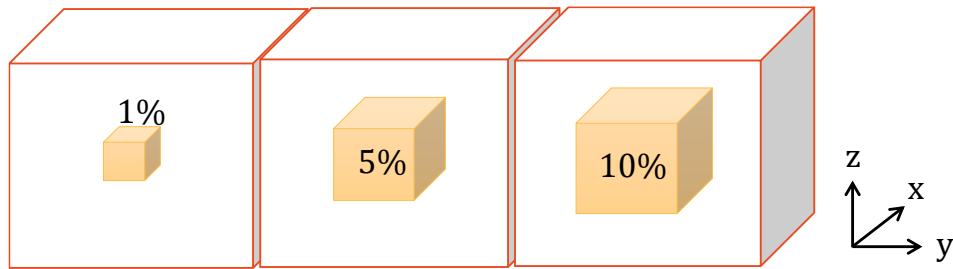


Figure 47. Illustration of different inclusion sizes (1, 5, 10% by volume) within the $53 \times 77 \times 77 \text{ mm}^3$ agar phantom.

Table 4. Dimensions of the inclusions used in the phantoms.

Inclusion volume	1%	5%	10%
Inclusion dimension	$30 \times 10 \times 10 \text{ mm}^3$	$30 \times 23 \times 23 \text{ mm}^3$	$30 \times 33 \times 33 \text{ mm}^3$

India ink was added to the agar mixture to act as an absorbing agent. The absorption and scattering coefficients of the background are 0.0066 mm^{-1} and 0.625 mm^{-1} , respectively, at 808 nm . The absorption of the inclusion is twice that of the background: 0.0132 mm^{-1} . The scattering coefficient of the inclusion is the same as the background. The homogeneous phantom has optical properties that match the background. The optical properties of the background and inclusion are summarized in Table 5.

Table 5. Optical properties of agar used for different inclusion sizes experiment. Values are given for 808nm.

	Absorption (mm ⁻¹)	Scattering (mm ⁻¹)
Background	0.0066	0.625
Inclusion	0.0132	0.625

6.2b. Experimental setup, image reconstruction and analysis

The agar phantom was placed between the source DMD and detector DMD. A 40mW 808nm laser was coupled with the source DMD. 850V was applied across the PMT coupled to the detector DMD. The SL patterns used was five horizontal stripes and five vertical stripes (Figure 48). The FOI was centered on the Y-Z plane of the agar phantom, with an area of 45x45mm². The phantoms were imaged in this sequence: homogeneous, 1%, 5% and 10%. 100 SL-DOT measurements were collected from each phantom. To measure the background light/dark noise from the room, the lasers were turned off and SL-DOT data was collected again. The true signal from the phantoms is the difference between the measurements and the dark noise.



Figure 48. SL pattern set used for the illumination and detection of light from the phantom, forming 100 unique measurements.

Once all measurements are collected, the data was processed in MATLAB prior to image reconstruction. The voltage measurements need to be calibrated in order to be used with the reconstruction algorithm. The forward model produces flux measurements that are a fraction of the source light intensity. To convert our measurements from the “experimental space” to the “simulation space,” the data from the homogeneous phantom is needed. A simulation of the SL-DOT measurements is

performed on a mesh with the same optical properties as the homogeneous phantom.

The conversion of the experimental data is as follows:

$$\frac{Heterogeneous_{sim}}{Heterogeneous_{exp}} = \frac{Homogeneous_{sim}}{Homogeneous_{exp}} \rightarrow$$

$$Heterogeneous_{sim} = \frac{Heterogeneous_{exp} \cdot Homogeneous_{sim}}{Homogeneous_{exp}} \quad (28)$$

where exp and sim denote experimental space and simulation space, respectively. This was done for each of the heterogeneous phantoms with inclusions. The $Heterogeneous_{sim}$ measurements are used then for the image reconstruction. The algorithm runs until the residual has not changed more than 5% for five iterations or for a max number of 20 iterations.

Once the absorption maps have been reconstructed, volumes were segmented at half-max of the recovered range, denoted as $\%V_{abs}$. The mean absorption of these segmented volumes was then calculated, denoted as $\bar{\mu}_a$.

6.2a. Results

The aim of this study is to the performance of SL-DOT in recovering small inclusions of different sizes. The inclusion sizes that were tested were 1% (10x10mm² cross-section), 5% (23x23mm²), and 10% (33x33mm²). The measurements for each phantom are shown in Figure 49. Because the homogeneous phantom does not have a highly absorbing inclusion, the measured flux for this case is the highest. With the increasing size of the inclusions, the amount of detected light decreases, resulting in the largest inclusion size (10% volume inclusion) having the least measured flux.

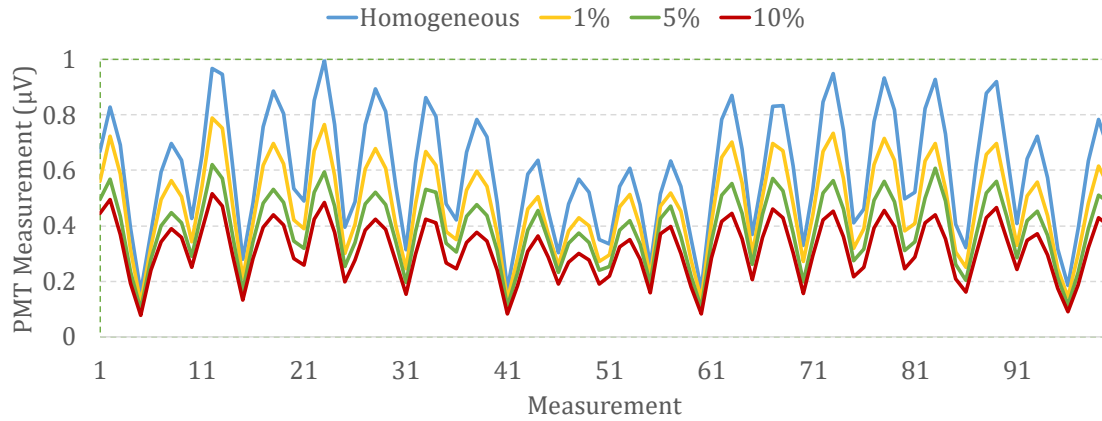


Figure 49. SL-DOT measurements from the homogeneous (blue), 1% (yellow), 5% (green), and 10% (red) phantoms using pattern set shown in Figure 48.

For each phantom, 3D absorption maps are recovered. Slices at four depths ($x = 10, 20, 30, 40\text{mm}$) are presented in Figure 50a. FEM elements in the mesh are segmented based on its absorption coefficient value at the center of its gravity. If the element's absorption value is above the half-maximum of the recovered absorption range, then that element considered to be part of the recovered volume (Figure 50b).

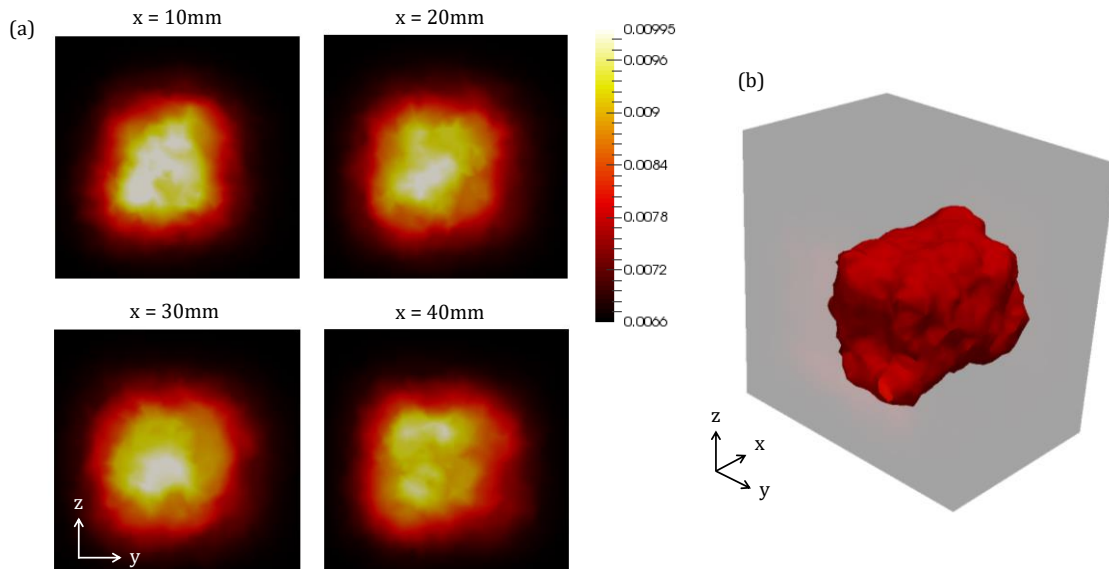


Figure 50. (a) Slices of the reconstructed absorption map for the 10% volume inclusion phantom are presented at $x = 10, 20, 30, 40\text{mm}$ in depth. (b) A volume (red) is segmented at half-maximum of the recovered absorption range to represent the recovered inclusion.

The image reconstructions for each phantom are presented in Figure 51. The smallest inclusion (1%) was difficult to recover, where the $\%V_{\text{abs}}$ (red) is not similar to the true shape of the inclusion (blue) (Figure 51b). The reconstructions for 5% and 10% are much closer in shape to the true inclusion. It is also important to note that the recovered $\bar{\mu}_a$ is dependent on the size of the inclusion, where smaller objects have lower absorption (Figure 51a). This was also seen in our simulation studies where the absorption, and subsequently the chromophore concentrations, were dependent on the size of the fibroglandular tissue within the breast.

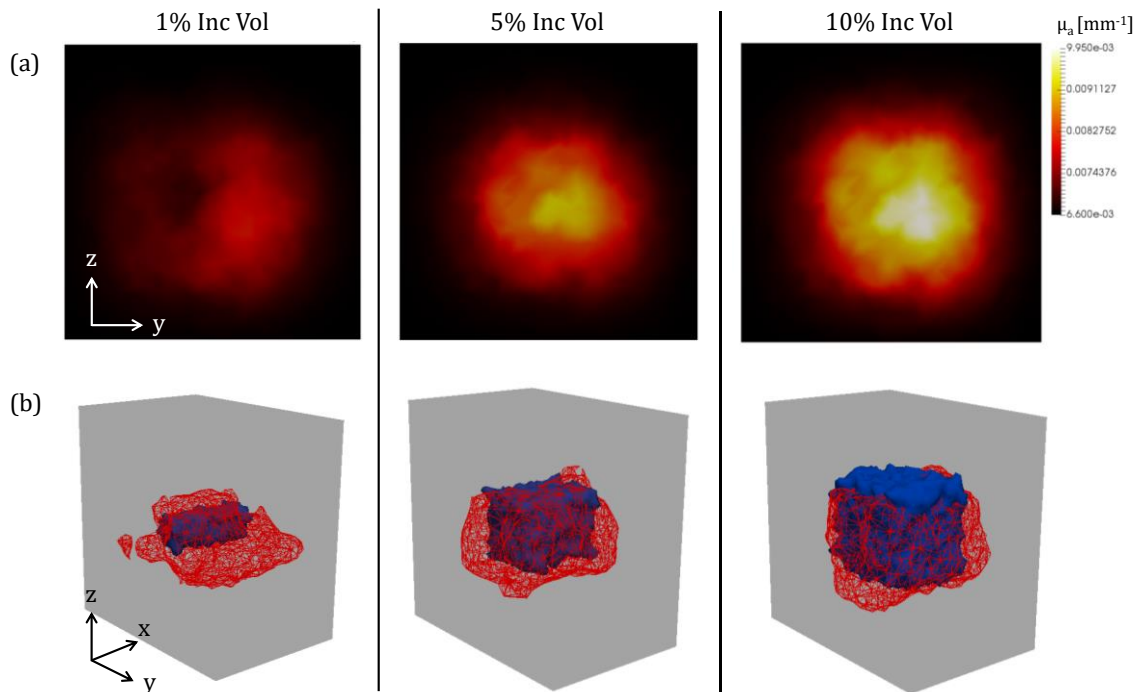


Figure 51. (a) The center slice of the image reconstruction for each phantom is presented in the top row. As the inclusion size increases, the higher the absorption is recovered. (b) The bottom row represents the 3D representation of the reconstructed volume. The red wireframe represents the contour of the volume segmented at half-max, V_{abs} , and the solid blue object represents the inclusion.

When comparing the $\%V_{\text{abs}}$ to the true volume of the inclusion, the smaller inclusions are greatly overestimated, where the $\%V_{\text{abs}}$ of the 1% inclusion is five times

greater (Table 6). This degree of overestimation is lower as the inclusion size increases, where the 10% inclusion is estimated as 10.4%. Although simulations of this phantom study showed that SL-DOT can recover the 3D map of the inclusion for 1% inclusion, we saw with our system that is very difficult to do experimentally. The reconstructed volume for the 1% phantom is not similar in shape to the actual inclusion. This may be the limit of our SL-DOT, where we may not be able to recover inclusions smaller than 2x2x3cm. As previously mentioned, the SL patterns are large in comparison to a single point source and detector. Therefore, the region of the phantom where the optical properties are more sensitive becomes larger for each source-detection combination. Additionally, we have a limited view of the phantom, where we collect measurements through one plane. For these reasons, SL-DOT is considered to be a low-resolution imaging system; however, it is important to note that this volume is well below the size of fibroglandular tissue found in the breast. For the application of imaging the larger fibroglandular tissue within the breast, our system may be sufficient in recovering the volumetric information. Furthermore, the recovered $\bar{\mu}_a$ also has a relationship with the inclusion size (Table 6), where we see a positive trend between absorption and inclusion size. This perhaps is the key to correcting the overestimation of smaller objects, which was done in our breast simulation studies.

Table 6. The recovered inclusion volume and mean absorption for each phantom.

Phantom	1%	5%	10%
Recovered %V _{abs}	4.92%	8.3%	10.4%
$\bar{\mu}_a$	0.0078mm ⁻¹	0.0085mm ⁻¹	0.0091mm ⁻¹

6.3 Size-dependency of multiple chromophores

The purpose of this phantom study is to observe the size-dependency of the recovered chromophores. This study is a slight modification of the previous study where the inclusion size is varied (5 and 10%); however, the 1% volumetric inclusion was excluded because we have determined that it is below the limit that can be reconstructed from experimental data. Additionally, specific NIR absorption dyes are used instead of the India ink. India ink has a constant absorption coefficient across the NIR region. For this reason, NIR782E and NIR869A, both of which have a large dynamic range of absorption in the NIR, were chosen. This would allow us to take multi-wavelength measurements and quantify each dye concentration. The inclusions across all phantoms have the same NIR782E (referred to as D1) and NIR869A (referred to as D2) concentrations.

6.3a. Phantoms

Three agar phantoms similar to study #1 were created, where one phantom was homogenous and used for calibration. The remaining two phantoms had centered inclusion sizes that represented 5% and 10% of the phantom's volume. The dimensions of the 5% and 10% volumetric inclusions are presented in study #1, Table 4. The dye concentrations within the background and inclusion are presented in Table 7. The concentration of D1 is higher in the background than the inclusion. Conversely, the concentration of D2 is higher in the inclusion than the background. This is to mimic the fibroglandular and adipose tissue, where the FGT has higher water and lower lipid than the adipose tissue. The dye concentrations resulted in the absorption

properties shown in Table 8 at the four wavelengths through the previously described modified Beer-Lambert law (Equation 2). Intralipid was added for the scattering properties, which was the same for both the inclusion and the background. Due to its wavelength-dependency, the scattering coefficient for each wavelength is different, where the shortest wavelength has the highest μ_s' and vice versa.

Table 7. D1 and D2 concentrations used in both the background and inclusion.

	Background	Inclusion
D1 ($\mu\text{g/mL}$)	0.2	0.05
D2 ($\mu\text{g/mL}$)	0.05	0.2

Table 8. The optical properties of the background and inclusion at 660, 785, 808 and 830nm.

	Bkg. μ_a (mm^{-1})	Inc. μ_a (mm^{-1})	Scattering μ_s' (mm^{-1})
660nm	0.0037	0.0025	0.778
785nm	0.0177	0.0107	0.645
808nm	0.0057	0.0081	0.624
830nm	0.0028	0.0086	0.606

6.3b. Experimental setup, image reconstruction and analysis

The experimental setup is similar to the first study, with the exception that multiple wavelengths of light were used instead. Four laser diodes 660nm (12mW), 785nm (30mW), 808nm (40mw), and 830nm (30mW), were connected to a fiber optic switch and outputted to the source DMD. When the 660nm laser was in use, 725V was applied across the PMT; for the remaining three wavelengths, the maximum 900V was applied across the PMT. The same five horizontal stripes and five vertical stripes SL-patterns were used (Figure 48). The FOI was centered on the agar phantom, with an area of $45 \times 45 \text{mm}^2$. The phantoms were imaged in this sequence: homogeneous, 5% and 10%. 100 SL-DOT measurements for each wavelength were

collected from each phantom. The dark noise was also recorded and used to correct the signals.

The data was calibrated with the homogeneous phantom measurements prior to image reconstruction. This is done for each phantom at each wavelength. The absorption maps are recovered for each phantom and each wavelength. The algorithm runs until the residual has not changed more than 5% for five iterations or for a max number of 20 iterations. Once the 3D absorption (μ_a) maps are recovered, the dye concentrations are estimated through a non-negative linear least squares minimization at each node in the mesh. This is based on the system of linear equations relating the μ_a at each wavelength to the dyes' concentrations through their unique extinction coefficients (Equation 18).

Once the dye concentration maps have been recovered, volumes were segmented at half-max of the recovered range to represent the reconstructed inclusion of the phantom. The mean dye concentrations are then calculated both within and outside of the reconstructed inclusions. These dye concentrations are denoted as either the background or inclusion, \bar{C}_N where N is D1 or D2. The contrast

of each dye map is calculated as $\frac{D_{inclusion}}{D_{background}}$.

6.3c. Results

From our SL-DOT measurements on the phantoms, the image reconstruction recovered the 3D absorption maps, which were used to estimate the concentrations of D1 and D2. As the inclusion volume increases from 5% to 10%, the contrast between the background and inclusion on both dye maps becomes more apparent

(Figure 52). The 10% inclusion has a lower recovered C_{D1} and a higher recovered C_{D2} (Figure 52). Despite the fact that the dye contrast between the background and inclusion should be the same, the 5% inclusion has lower contrast for both dyes compared to the 10% case (Table 9).

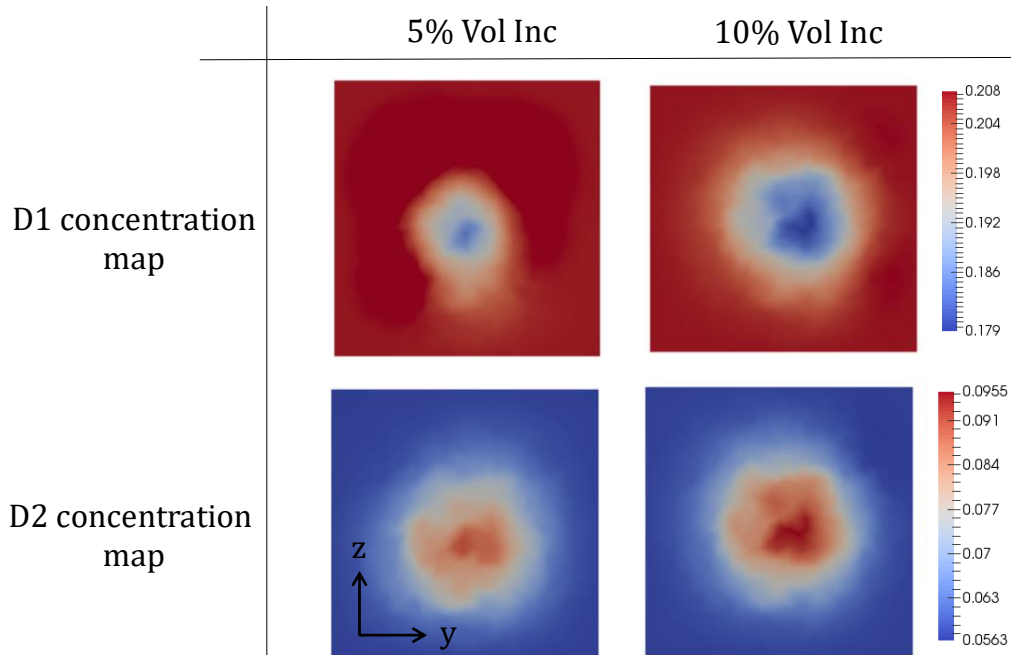


Figure 52. The center slice of the reconstructed dye (D1 and D2) concentrations are shown for phantoms with 5% and 10% inclusion sizes. The larger the inclusion, the more contrast between the inclusion and background is seen.

Table 9. The recovered contrast between the inclusion and the background for both D1 and D2.

	5% Inclusion Volume	10% Inclusion Volume
Recovered D1 contrast	1.36X	2.25X
Recovered D2 contrast	1.30X	2.12X

The previous study simplistically looked at the relationship of the absorption and inclusion size with data taken at one wavelength. By taking multi-wavelength measurements, multiple chromophores' concentrations can be recovered, providing a richer amount of data. With the introduction of more data, more considerations and

analysis are needed to accurately estimate the inclusion. As the inclusion size increases, the recovered chromophore concentration becomes more accurate. This resulted in the 10% inclusion phantom having a higher contrast between the inclusion and the background. The true contrast between these compartments is 4X, which was never fully recovered with the largest inclusion. In a standalone diffuse optical system, the recovery of the true contrast is not expected; we only anticipate a portion of this contrast to be reconstructed. This does, however, corroborate the results seen in the breast simulation study, where low density cases tend to have chromophore concentrations similar to that of the adipose tissue (*i.e.* lower contrast with the adipose tissue). With this phantom study, we confirm what we have seen from simulations and also gained insight about the capabilities of our SL-DOT system.

6.4 Recovering contrast between the inclusion and background

We have found a relationship between the segmented volumes and the measured $\bar{\mu}_a$ in the first study. In the second study, we saw the effect of inclusion size on the reconstructed dye concentrations and the dye contrast between the inclusion and the background. Our next step is to test our system's ability in distinguishing different contrasts of dye concentration between the inclusion and the background. Both NIR782E and NIR869A were used again. Our aim in this study is to recover the amounts of the dyes used by creating phantoms with variable dye concentrations.

6.4a. Phantoms

Four agar phantoms with a dimension size of 53x77x77mm³ were created, where one served as the homogeneous phantom that shared the same optical

properties as the background for calibration. The three heterogeneous phantoms (P1, P2, & P3) all had an inclusion size of $30 \times 33 \times 33 \text{ mm}^3$, representing 10% of the phantom's volume (Figure 53).

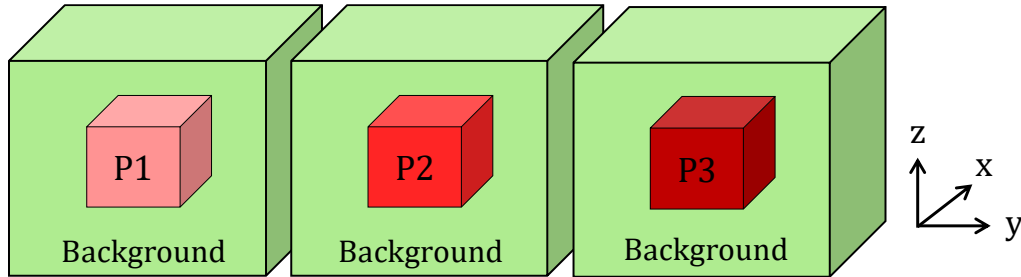


Figure 53. The geometry of the heterogeneous phantoms for this study. The background surrounds an inclusion that is 10% of the phantom's volume. The inclusions P1, P2, and P3 denote the specific dye concentrations used.

The NIR782E dye, referred to as D1 again, is more concentrated in the background, while NIR869A (D2) is more concentrated in the inclusion. The exact formulation for each agar mixture is presented in Table 10. The background refers the portion enclosing each inclusions, P1, P2 and P3, in three separate heterogeneous phantoms. The normalized values are also presented in Table 11 to show the contrast between the inclusions and the background.

Table 10. The concentrations of NIR782E (D1) and NIR869A (D2) added to each agar mixture to form the phantoms.

	Background	P1 inclusion	P2 inclusion	P3 inclusion
D1 ($\mu\text{g/mL}$)	0.2	0.1	0.05	0.025
D2 ($\mu\text{g/mL}$)	0.05	0.1	0.2	0.3

Table 11. The dye concentrations inside the inclusions normalized to the background. This highlights the concentration contrast between the background and each inclusion.

	Background	P1 inclusion	P2 inclusion	P3 inclusion
D1	1	0.5X	0.25X	0.125X
D2	1	2X	4X	6X

Based on the dye concentrations within each agar mixture, the total absorption is calculated based on equation (2), where each dye concentration is multiplied by its respective wavelength-dependent extinction coefficient. Scattering is the same throughout the entire phantom and is controlled by the amount of Intralipid that is added to the agar mixture. The total absorption for the background and each inclusion are shown in Table 12 at each wavelength of the system (660, 785, 808, 830nm). The wavelength-dependent scattering coefficients are also presented.

Table 12. Optical properties of the background and inclusions calculated at each wavelength.

	Bkg. μ_a (mm^{-1})	P1 Inc. μ_a (mm^{-1})	P2 Inc. μ_a (mm^{-1})	P3 Inc. μ_a (mm^{-1})	Scattering μ_s' (mm^{-1})
660nm	0.0037	0.0025	0.0025	0.003	0.778
785nm	0.0177	0.0114	0.0107	0.0121	0.645
808nm	0.0057	0.0055	0.0081	0.0112	0.624
830nm	0.0028	0.0045	0.0086	0.0127	0.606

6.4b. Experimental setup, image reconstruction and analysis

Four laser diodes, 660nm (12mW), 785nm (30mW), 808nm (40mw), and 830nm (30mW), were connected to a fiber switch which controls the wavelength of light that is sent to the source DMD. The FOI was centered on the agar phantom, with an area of 45x45mm². When the 660nm laser source was used, 725V was applied across the PMT; for the remaining three wavelengths, the maximum 900V was applied across the PMT. The same five horizontal stripes and five vertical stripes SL-pattern set was used (Figure 48). The phantoms were imaged in following sequence: homogeneous, P1, P2 and P3. 100 SL-DOT measurements for each wavelength were collected from each phantom. The dark noise was also recorded and used to correct the signals.

Prior to image reconstruction, the data was calibrated with the homogeneous phantom measurements as previously explained. This is done for each phantom at each wavelength. The image reconstruction is then performed and the absorption maps are recovered for each phantom and each wavelength. The algorithm runs until the residual has not changed more than 5% for five iterations or for a max number of 20 iterations. Once the 3D absorption (μ_a) maps are recovered, the dye concentrations are estimated through a non-negative linear least squares minimization at each node in the mesh. This is based on the system of linear equations relating the μ_a at each wavelength to the dyes' concentrations through their unique extinction coefficients (Equation 18).

Once the dye concentration maps have been recovered, volumes were segmented at half-max of the recovered range. These segmented volumes represent the reconstructed inclusion of the phantom. The mean dye concentrations both within and outside of the reconstructed inclusions were calculated. These dye concentrations are denoted as either the background or inclusion \bar{D}_N , where N is either D1 or D2. The contrast for each dye is then calculated as the ratio of the dye concentration within the inclusion to the dye concentration in the background.

6.4c. Results

From the multi-wavelength SL-DOT measurements, we reconstructed the absorption maps and subsequently the 3D dye concentration maps. The center slices of these maps show are presented in Figure 54. The inclusion is much clearly seen in both P2 and P3 than in P1 (Figure 54). This is most likely due to P1's low contrast of

the dyes between the background and inclusion. The recovered C_{D1} is lowest for the P3 phantom, where the D1 contrast is the strongest (Figure 54, top). The recovered C_{D2} is highest for P3, which similarly has the strongest D2 contrast (Figure 54, bottom). The dye contrast for each phantom is presented in Table 13.

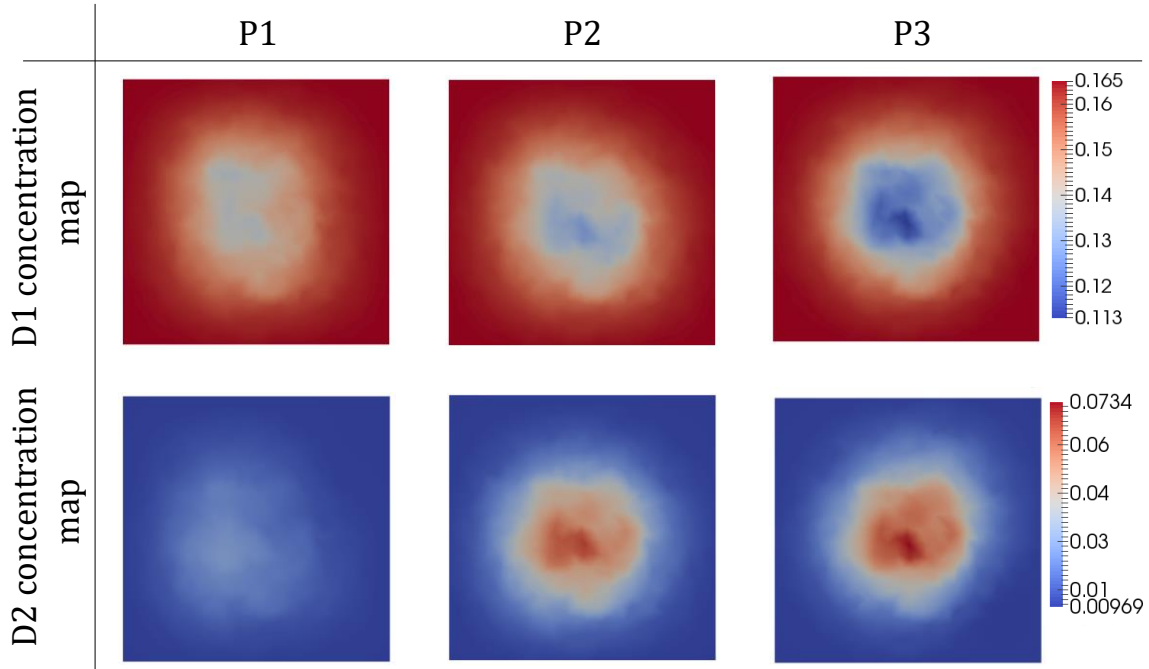


Figure 54. Center slices of the recovered dye (D1 & D2) concentrations for each phantom (P1, P2, & P3).

Table 13. The recovered dye contrast between the inclusion and background for each phantom (P1, P2, & P3).

	P1	P2	P3
Recovered D1 contrast	0.88X	0.85X	0.78X
Recovered D2 contrast	2.08X	3.38X	3.80X

In order to truly evaluate the SL-DOT's ability in recovering the dyes concentrations, we performed noiseless simulations with the same parameters as our experimental setup. The experimental results were compared to the simulation

results, which we consider to be the best results possible from the SL-DOT image reconstruction. The dye contrast for phantom is calculated and the simulated and experimental contrasts are compared (Figure 55). For D1, both simulation (red) and experimental (green) has increasing contrast, seen as a further deviation from the value 1, as the inclusion size increases (Figure 55a). This is also the case for D2, where the experimental and simulation contrast are similar to each other and are both increasing as the inclusion size increases (Figure 55b).

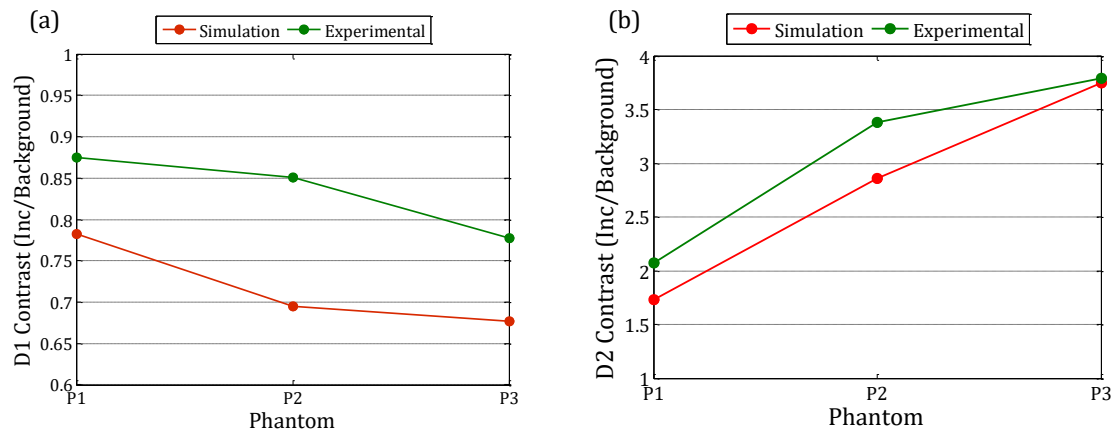


Figure 55. The dye contrast between the inclusion and background is shown for (a) D1 and (b) D2. The contrast for each phantom is calculated as the mean dye concentration of the inclusion divided by the concentration in the background. The contrast from simulated data is shown in red and the contrast from the experimental data is shown in green.

From this study, it is interesting to note that noiseless simulated SL-DOT measurements have a limitation in recovering the dye concentrations. We expect that experimental data cannot surpass the simulated results as the experimental measurements are susceptible to noise. Our best aim would be to match these simulation results. Considering the application in measuring breast density, this study was designed to test SL-DOT's ability to measure oxy and deoxy-hemoglobin

rather than the water and lipid concentrations. We assume that the molecular structure of the fibroglandular tissue would not vary greatly among patients and that it is the volume of these structures that are variable. Hemoglobin concentrations, however, may not be the same among different patients as the microvasculature of the breast would vary. This is the basis of different levels of BPE seen among patients, which is related to the blood perfusion of the fibroglandular tissue. Because BPE is an enhancement index, perhaps the concentration contrast ratio between the optically imaged FGT and adipose tissue is correlated and can be used as a measurement equivalent to BPE.

There is also interest in recovering the contrast between the background and inclusion because of the availability and advancement of NIR contrast agents. The use of a contrast agent greatly improves the signal that can be collected from the breast. Indocyanine green (ICG) is a FDA-approved fluorescent agent that is excited at 785nm and emits light at 830nm. ICG binds to plasma proteins in the blood, typically to albumin, increases its size and restricting its circulation to within the vasculature [109]. For this reason, ICG can highlight regions with increased vasculature and blood flow. The gadolinium-DTPA agent used in contrast-enhanced MRI, on the other hand, is very small in size and can permeate into the extravasculature [109]. Despite this, we believe ICG can indicate regions of the fibroglandular tissue that have higher perfusion, and therefore can be used to also quantify functional breast density. Because the circulation time of ICG is on the order of minutes [109], SL-DOT is suitable for imaging the flow of ICG through the breast. This can be accomplished by modifying the SL-DOT system for fluorescence imaging,

where the simple addition of an optical bandpass filter collects light at 830nm, the emission wavelength of ICG. Additionally, because we are interested in one wavelength, 100 measurements can be obtained within one minute, well within the timeframe of ICG circulation in the blood.

Chapter seven: Conclusions and future work

7.1 Conclusions

The work presented in this thesis represents the preliminary steps in developing an optical technique to measure breast density. Structured-light diffuse optical tomography (SL-DOT) is a wide-field imaging technique that uses structured-light patterns for illumination and detection. The advantages of this technique are its speed and relatively low cost. The application of imaging breast density has not been explored with SL-DOT and this work aims to build the foundation for developing a system that can be used in the clinics.

Simulations performed on breast phantoms showed that although volumetric information can be obtained from our optically recovered chromophore maps, smaller fibroglandular tissue geometries tended to be overestimated. Analysis revealed that the size of the FGT affected the recovered water and lipid concentrations, where lower densities had lower water and higher lipid content. This information was used to form a regression model that could estimate the percent breast density well ($r = 0.97$).

The results of our simulations were considered when building our instrumentation and planning our phantom experiments. We wanted to confirm that is a relationship between the true size of the inclusion and the recovered absorption despite not reconstructing the correct inclusion volume. In our studies, it has been shown that SL-DOT has difficulty in imaging smaller objects ($10 \times 10 \text{mm}^2$ cross-section): the tomographic maps show a volume that does not match the true

inclusion, but the image reconstruction still recovers an object. Perhaps for the application of measuring breast density, the actual visual image may not matter as long as the FGT volume is quantified correctly.

Additionally, the SL-DOT technique has been tested in recovering varying chromophore concentrations within varying inclusion sizes. We also found a size-dependency of the recovered chromophore concentrations and the contrast between the inclusion and background. This is similar to what was seen in our simulation studies. Recovering different levels of contrast was also tested. Although the exact concentrations and contrast are not recovered, some contrast between the background and the inclusion is preserved among the different phantoms.

Understanding the capabilities and limitations of our system are the first steps in developing this technique to be used to measuring breast density. There are two clinically relevant parameters in which we are interested: the volume of fibroglandular tissue within the breast and the amount of hemoglobin within the FGT that may be correlated to background parenchymal enhancement (BPE) seen in MRI. Though most of the work in this thesis has been focused on the anatomical breast density, further studies are needed to expand our technique to measuring the functional breast density.

7.2 Future Work

There is still much work that needs to be done in order to develop the SL-DOT system for clinical use. Because water and lipid have peak absorption beyond 850nm, our current system is not capable of measuring these chromophores. The

incorporation of a NIR-PMT that is sensitive in the 850-1000nm range, in addition to the current VIS-PMT, would expand the wavelengths of light that can be measured. Once the NIR-PMT is acquired, water and lard phantoms can be used to test the improved the benchtop system. Further studies can expand the number of chromophores to four to mimic the molecular components of the breast: water, lipid oxy- and deoxyhemoglobin.

As mentioned previously, SL patterns can be arbitrary, making optimization of the pattern set tedious and difficult. Although this study looks at binary patterns corresponding to “on” and “off” pixels, the DMDs are capable of projecting 8-bit images. This greatly expands the number of possible SL patterns and would require extensive studies to truly optimize the pattern set to measure breast density.

Human studies are needed to truly test the capabilities of the SL-DOT system. The conversion of our benchtop hardware into a human breast imaging system would require some considerations. In our system, two transparent plates would be used to lightly compress the breast to hold it in place. The compression of the breast have been shown to affect the optical properties [110], so studies are needed to see the effects on our measurements. If a relationship is found, perhaps a correction factor can be used. Additionally, in our experiments the agar phantoms are rectangular, but each breast has a unique shape and curvature. The source DMD and additional CCD cameras can then be used to outline the shape of the breast so the SL pattern can be shaped to cover as much as the breast as possible. In addition, the CCD cameras surrounding the breast can collect the breast boundary shape to be used in our image reconstructions and to measure the breast volume.

Our breast imaging work have been based on simulations and assumed chromophore concentrations, so a new training set with human data is needed to form a more accurate regression model. The basis of the simulation and the phantom studies have shown us what to expect, where although low density cases may be overestimated, the recovered water and lipid concentrations can be used to correct for this error. What was difficult to simulate was the BPE that is seen in MRI, because no study has truly correlated hemoglobin values to the BPE parameters. It would be very interesting to be able to find the relationship between the higher intensity enhancement from the blood perfusion seen on MRI to the optically measured hemoglobin values. Because the recovered hemoglobin values may also depend on the fibroglandular size, perhaps the ratio between the hemoglobin seen within the segmented optical volume and outside this volume may be correlated to the BPE.

Lastly, fluorescence imaging can be implemented with the SL-DOT technique through the simple addition of an optical bandpass filter [48]. NIR fluoresce imaging can enhance the information collected from DOT by localizing and quantifying molecular probes tagged with fluorescent agents [111]. As previously mentioned, the fluorophore ICG can be used as a contrast agent to identify areas within the FGT with high vascularization. Additionally, with advancements in tumor-targeted probes, applications can also include cancer detection and characterization [112]. For example, fluorophores conjugated with ligands targeting the folate receptor can be used in breast cancer imaging [113]. Through this specific-targeting, fluorescence can distinguish between the tumor and background tissue.

References

1. "What are the key statistics about breast cancer?," <http://www.cancer.org/cancer/breastcancer/detailedguide/breast-cancer-key-statistics>.
2. U.S. Preventive Services Task Force, "Screening for Breast Cancer: U.S. Preventive Services Task Force Recommendation Statement," *Ann. Intern. Med.* **151**, 716–726 (2009).
3. K. C. Oeffinger, E. T. Fontham, R. Etzioni, A. Herzig, J. S. Michaelson, Y. C. Shih, L. C. Walter, T. R. Church, C. R. Flowers, S. J. LaMonte, a M. Wolf, C. DeSantis, J. Lortet-Tieulent, K. Andrews, D. Manassaram-Baptiste, D. Saslow, R. a Smith, O. W. Brawley, and R. Wender, "Breast Cancer Screening for Women at Average Risk: 2015 Guideline Update From the American Cancer Society," *J. Am. Med. Assoc.* **314**, 1599–1614 (2015).
4. G. S. Lebovic, A. Hollingsworth, and S. a Feig, "Risk assessment, screening and prevention of breast cancer: A look at cost-effectiveness.," *Breast* **19**, 260–267 (2010).
5. D. Saslow, C. Boetes, W. Burke, S. Harms, M. O. Leach, C. D. Lehman, E. Morris, E. Pisano, M. Schnall, S. Sener, R. A. Smith, E. Warner, M. Yaffe, K. S. Andrews, and C. A. Russell, "American Cancer Society guidelines for breast screening with MRI as an adjunct to mammography.," *CA. Cancer J. Clin.* **57**, 75–89 (2007).
6. N. F. Boyd, G. A. Lockwood, J. W. Byng, D. L. Tritchler, and M. J. Yaffe, "Mammographic Densities and Breast Cancer," *Cancer Epidemiol. biomarkers Prev.* **7**, 1133–1144 (1998).
7. N. F. Boyd, L. J. Martin, M. J. Yaff, and S. Minkin, "Mammographic density and breast cancer risk : current understanding and future prospects," *Breast Cancer Res.* **13**, 1–12 (2011).
8. A. T. Wang, C. M. Vachon, K. R. Brandt, and K. Ghosh, "Breast density and breast cancer risk: A practical review," *Mayo Clin. Proc.* **89**, 548–557 (2014).
9. N. F. Boyd, L. J. Martin, M. Bronskill, M. J. Yaffe, N. Duric, and S. Minkin, "Breast tissue composition and susceptibility to breast cancer.," *J. Natl. Cancer Inst.* **102**, 1224–37 (2010).
10. C. M. Vachon, V. S. Pankratz, C. G. Scott, L. Haeberle, E. Ziv, M. R. Jensen, K. R. Brandt, D. H. Whaley, J. E. Olson, K. Heusinger, C. C. Hack, S. M. Jud, M. W. Beckmann, R. Schulz-Wendland, J. a. Tice, A. D. Norman, J. M. Cunningham, K. S. Purrington, D. F. Easton, T. a. Sellers, K. Kerlikowske, P. a. Fasching, and F. J. Couch, "The contributions of breast density and common genetic variation to breast cancer risk," *J. Natl. Cancer Inst.* **107**, 1–4 (2015).

11. M. T. Mandelson, N. Oestreicher, P. L. Porter, D. White, C. A. Finder, H. Taplin, Stephen, and E. White, "Breast density as a Predictor of Mammographic Detection: Compariton of Interval- and Screen-Detected Cancers," *J. Natl. Cancer Inst.* **92**, 1081–1087 (2000).
12. Z. Zhou and Z.-R. Lu, "Gadolinium-based contrast agents for magnetic resonance cancer imaging,," *Wiley Interdiscip. Rev. Nanomed. Nanobiotechnol.* **5**, 1–18 (2013).
13. H. Daldrup, D. M. Shames, M. Wendland, Y. Okuhata, T. M. Link, W. Rosenau, L. Ying, and R. C. Brasch, "Correlation of Dynamic Contrast Enhanced MR Imaging with Histologic Tumor Grade: Comparison of Macromolecular and Small-Molecular Contrast Media," *Am. J. Roentgenol.* **171**, 941–949 (1998).
14. V. King, J. D. Brooks, J. L. Bernstein, A. S. Reiner, M. C. Pike, and E. A. Morris, "Background Parenchymal Enhancement at Breast MR Imaging and Breast Cancer Risk," *Radiology* **260**, 50–60 (2011).
15. M. C. Pike and C. L. Pearce, "Mammographic density, MRI background parenchymal enhancement and breast cancer risk," *Ann. Oncol.* **24**, (2013).
16. J. N. Wolfe, "A Study of Breast Parenchyma by Mammography in the Normal Woman and Those with Benign and Malignant Disease," *Radiology* **89**, (1967).
17. J. Wolfe, "Breast patterns as an index of risk for developing breast cancer," *Am. J. Roentgenol.* **126**, 1130–1139 (1976).
18. E. U. Ekpo and M. F. McEntee, "Measurement of breast density with digital breast tomosynthesis-a systematic review," *Br. J. Radiol.* **87**, 1–9 (2014).
19. J. Wang, A. Azziz, B. Fan, S. Malkov, C. Klifa, D. Newitt, S. Yitta, N. Hylton, K. Kerlikowske, and J. a. Shepherd, "Agreement of mammographic measures of volumetric breast density to MRI,," *PLoS One* **8**, e81653 (2013).
20. M. Lin, S. Chan, J.-H. Chen, D. Chang, K. Nie, S.-T. Chen, C.-J. Lin, T.-C. Shih, O. Nalcioglu, and M.-Y. Su, "A new bias field correction method combining N3 and FCM for improved segmentation of breast density on MRI," *Med. Phys.* **38**, 5 (2011).
21. M. Lin, J.-H. Chen, X. Wang, S. Chan, S. Chen, and M.-Y. Su, "Template-based automatic breast segmentation on MRI by excluding the chest region,," *Med. Phys.* **40**, 122301 (2013).
22. J. H. Chen, H. Yu, M. Lin, R. S. Mehta, and M. Y. Su, "Background parenchymal enhancement in the contralateral normal breast of patients undergoing neoadjuvant chemotherapy measured by DCE-MRI," *Magn. Reson. Imaging* **31**, 1465–1471 (2013).
23. S. Wu, S. P. Weinstein, M. J. DeLeo, E. F. Conant, J. Chen, S. M. Domchek, and D. Kontos, "Quantitative assessment of background parenchymal enhancement in breast MRI predicts response to risk-reducing salpingo-oophorectomy: preliminary evaluation in a cohort of BRCA1/2 mutation carriers," *Breast Cancer Res.* **17**, 67 (2015).

24. T. D. O'Sullivan, A. E. Cerussi, D. J. Cuccia, and B. J. Tromberg, "Diffuse optical imaging using spatially and temporally modulated light," *J. Biomed. Opt.* **17**, 071311 (2012).
25. V. Ntziachristos, J. Ripoll, L. V Wang, and R. Weissleder, "Looking and listening to light: the evolution of whole-body photonic imaging," *Nat. Biotechnol.* **23**, 313–320 (2005).
26. J. C. Hebden, S. R. Arridge, and D. T. Delphy, "Optical imaging in medicine: I. Experimental techniques," *Phys. Med. Biol.* **42**, 825–840 (1997).
27. S. R. Arridge and J. C. Hebden, "Optical imaging in medicine: II. Modelling and reconstruction," *Phys. Med. Biol.* **42**, 841–853 (1997).
28. J. Ripoll, V. Ntziachristos, J. P. Culver, D. N. Pattanayak, A. G. Yodh, and M. Nieto-vesperinas, "Recovery of optical parameters in multiple-layered diffusive media: theory and experiments," *J. Opt. Soc. Am. A* **18**, 821–830 (2001).
29. L. O. Svaasand, S. Thorsten, J. B. Fishkin, T. Pham, B. J. Tromberg, and M. W. Berns, "Reflectance measurements of layered media with diffuse photon-density waves: a potential tool for evaluating deep burns and subcutaneous lesions," *Phys. Med. Biol.* **44**, 801–813 (1999).
30. B. J. Tromberg, B. W. Pogue, K. D. Paulsen, A. G. Yodh, D. A. Boas, and A. E. Cerussi, "Assessing the future of diffuse optical imaging technologies for breast cancer management," *Med. Phys.* **35**, 2443–51 (2008).
31. A. Corlu, R. Choe, T. Durduran, K. Lee, M. Schweiger, S. R. Arridge, E. M. C. Hillman, and A. G. Yodh, "Diffuse optical tomography with spectral constraints and wavelength optimization," *Appl. Opt.* **44**, 2082 (2005).
32. B. a. Brooksby, "Combining near infrared tomography and magnetic resonance imaging to improve breast tissue chromophore and scattering assessment," (2005).
33. S. Srinivasan, B. W. Pogue, S. Jiang, H. Dehghani, C. Kogel, S. Soho, J. J. Gibson, T. D. Tosteson, S. P. Poplack, and K. D. Paulsen, "In vivo hemoglobin and water concentrations, oxygen saturation, and scattering estimates from near-infrared breast tomography using spectral reconstruction," *Acad. Radiol.* **13**, 195–202 (2006).
34. P. Taroni, G. Quarto, A. Pifferi, F. Ieva, A. M. Paganoni, F. Abbate, N. Balestreri, S. Menna, E. Cassano, and R. Cubeddu, "Optical identification of subjects at high risk for developing breast cancer," *J. Biomed. Opt.* **18**, 060507 (2013).
35. P. Taroni, A. Pifferi, G. Quarto, L. Spinelli, A. Torricelli, F. Abbate, A. Villa, N. Balestreri, S. Menna, E. Cassano, and R. Cubeddu, "Noninvasive assessment of breast cancer risk using time-resolved diffuse optical spectroscopy," *J. Biomed. Opt.* **15**, 060501 (2010).

36. K. M. Blackmore, J. a Knight, R. Jong, and L. Lilge, "Assessing breast tissue density by transillumination breast spectroscopy (TIBS): an intermediate indicator of cancer risk," *Br. J. Radiol.* **80**, 545–56 (2007).
37. K. M. Blackmore, J. a Knight, and L. Lilge, "Association between transillumination breast spectroscopy and quantitative mammographic features of the breast," *Cancer Epidemiol. Biomarkers Prev.* **17**, 1043–50 (2008).
38. B. Brooksby, B. W. Pogue, S. Jiang, H. Dehghani, S. Srinivasan, C. Kogel, T. D. Tosteson, J. Weaver, S. P. Poplack, and K. D. Paulsen, "Imaging breast adipose and fibroglandular tissue molecular signatures by using hybrid MRI-guided near-infrared spectral tomography," *Proc. Natl. Acad. Sci. U. S. A.* **103**, 8828–33 (2006).
39. F. El-Ghoussein, M. a Mastanduno, S. Jiang, B. W. Pogue, and K. D. Paulsen, "Hybrid photomultiplier tube and photodiode parallel detection array for wideband optical spectroscopy of the breast guided by magnetic resonance imaging," *J. Biomed. Opt.* **19**, 011010 (2014).
40. T. D. O'Sullivan, A. Leproux, J.-H. Chen, S. Bahri, A. Matlock, D. Roblyer, C. E. McLaren, W.-P. Chen, A. E. Cerussi, M.-Y. Su, and B. J. Tromberg, "Optical imaging correlates with magnetic resonance imaging breast density and reveals composition changes during neoadjuvant chemotherapy," *Breast Cancer Res.* **15**, R14 (2013).
41. P. Taroni, A. Pifferi, E. Salvagnini, L. Spinelli, A. Torricelli, and R. Cubeddu, "Seven-wavelength time-resolved optical mammography extending beyond 1000 nm for breast collagen quantification," *Opt. Express* **17**, 15932–46 (2009).
42. P. Taroni, A. Pifferi, G. Quarto, A. Farina, F. Ieva, A. M. Paganoni, F. Abbate, E. Cassano, and R. Cubeddu, "Time domain diffuse optical spectroscopy: *In vivo* quantification of collagen in breast tissue," **9529**, 952910 (2015).
43. K. Blyschak, M. Simick, R. Jong, and L. Lilge, "Classification of breast tissue density by optical transillumination spectroscopy: optical and physiological effects governing predictive value," *Med. Phys.* **31**, 1398–1414 (2004).
44. K. M. Blackmore, S. Dick, J. Knight, and L. Lilge, "Estimation of mammographic density on an interval scale by transillumination breast spectroscopy," *J. Biomed. Opt.* **13**, 064030 (2008).
45. N. Shah, a Cerussi, C. Eker, J. Espinoza, J. Butler, J. Fishkin, R. Hornung, and B. Tromberg, "Noninvasive functional optical spectroscopy of human breast tissue," *Proc. Natl. Acad. Sci. U. S. A.* **98**, 4420–5 (2001).
46. N. Shah, A. E. Cerussi, D. Jakubowski, D. Hsiang, J. Butler, and B. J. Tromberg, "Spatial variations in optical and physiological properties of healthy breast tissue," *J. Biomed. Opt.* **9**, 534–40 (2004).

47. S. Bélanger, M. Abran, X. Intes, C. Casanova, F. F. F. Lesage, S. Bélanger, M. Abran, X. Intes, C. Casanova, and F. F. F. Lesage, "Real-time diffuse optical tomography based on structured illumination," *J. Biomed. Opt.* **15**, 0160061–7 (2010).
48. Q. Pian, R. Yao, L. Zhao, and X. Intes, "Hyperspectral time-resolved wide-field fluorescence molecular tomography based on structured light and single-pixel detection," *Opt. Lett.* **40**, 431–434 (2015).
49. J. Chen and X. Intes, "Time-resolved Optical Imaging with Patterned Light for Pre-clinical Studies," *Biomed. Opt. 3-D Imaging OSA Opt. Photonics Congr.* **4**, 6–8 (2010).
50. P. Taroni, A. Pifferi, G. Quarto, L. Spinelli, A. Torricelli, F. Abbate, N. Balestreri, S. Ganino, S. Menna, E. Cassano, and R. Cubeddu, "Effects of tissue heterogeneity on the optical estimate of breast density," *Biomed. Opt. Express* **3**, 2411–8 (2012).
51. S. Srinivasan, B. W. Pogue, C. Carpenter, S. Jiang, W. a Wells, S. P. Poplack, P. a Kaufman, and K. D. Paulsen, "Developments in quantitative oxygen-saturation imaging of breast tissue in vivo using multispectral near-infrared tomography.," *Antioxid. Redox Signal.* **9**, 1143–56 (2007).
52. S. R. Arridge, "Optical tomography in medical imaging," *Inverse Probl.* **15**, 41–43 (1999).
53. S. R. Arridge, "The forward and inverse problems in time-resolved infrared imaging," *Med. Opt. Tomogr. Funct. Imaging Monit.* 35–64 (1993).
54. S. R. Arridge, M. Cope, and D. T. Delpy, "The theoretical basis for the determination of optical pathlengths in tissue: temporal and frequency analysis," *Phys. Med. Biol.* **37**, 1531–60 (1992).
55. H. Liu, D. A. Boas, Y. Zhang, A. G. Yodh, and B. Chance, "Determination of optical properties and blood oxygenation in tissue using continuous NIR light.," *Phys. Med. Biol.* **40**, 1983–1993 (1995).
56. A. G. Yodh and B. Chance, "Spectroscopy and imaging with diffusing light," *Phys. Today* **48**, 34–40 (1995).
57. M. S. Patterson, B. Chance, and B. C. Wilson, "Time resolved reflectance and transmittance for the non-invasive measurement of tissue optical properties," *Appl. Opt.* **28**, 2331–2336 (1989).
58. L. Kocsis, P. Herman, and A. Eke, "The modified Beer-Lambert law revisited," *Phys. Med. Biol.* **51**, N91–8 (2006).
59. D. R. Busch, R. Choe, M. A. Rosen, W. Guo, T. Durduran, M. D. Feldman, C. Mies, B. J. Czerniecki, J. Tchou, A. Demichele, M. D. Schnall, and A. G. Yodh, "Optical malignancy parameters for monitoring progression of breast cancer neoadjuvant chemotherapy," *Biomed. Opt. Express* **4**, 105–21 (2013).

60. R. Choe, A. Corlu, K. Lee, T. Durduran, S. D. Konecky, M. Grosicka-Koptyra, S. R. Arridge, B. J. Czerniecki, D. L. Fraker, A. DeMichele, B. Chance, M. A. Rosen, and A. G. Yodh, "Diffuse optical tomography of breast cancer during neoadjuvant chemotherapy: a case study with comparison to MRI," *Med. Phys.* **32**, 1128–39 (2005).
61. T. Durduran, R. Choe, G. Yu, C. Zhou, J. C. Tchou, B. J. Czerniecki, and A. G. Yodh, "Diffuse optical measurement of blood flow in breast tumors," *Opt. Lett.* **30**, 2915–2917 (2005).
62. T. Durduran, R. Choe, J. P. Culver, L. Zubkov, M. J. Holboke, J. Giammarco, B. Chance, and A. G. Yodh, "Bulk optical properties of healthy female breast tissue," *Phys. Med. Biol.* **47**, (2002).
63. G. Quarto, A. Torricelli, L. Spinelli, A. Pifferi, R. Cubeddu, and P. Taroni, "Breast Monitoring by Time-Resolved Diffuse Optical Imaging," in *Advanced Time-Correlated Single Photon Counting Applications*, W. Becker, ed. (Springer International Publishing, 2015), Vol. 111, pp. 587–611.
64. T. Durduran, R. Choe, W. B. Baker, and a G. Yodh, "Diffuse optics for tissue monitoring and tomography," *Reports Prog. Phys.* **73**, 076701 (2010).
65. A. E. Cerussi, D. Jakubowski, N. Shah, F. Bevilacqua, R. Lanning, a J. Berger, D. Hsiang, J. Butler, R. F. Holcombe, and B. J. Tromberg, "Spectroscopy enhances the information content of optical mammography," *J. Biomed. Opt.* **7**, 60–71 (2002).
66. G. M. Hale and M. R. Querry, "Optical Constants of Water in the 200-nm to 200-microm Wavelength Region.," *Appl. Opt.* **12**, 555–563 (1973).
67. R. L. P. van Veen, H. J. C. M. Sterenborg, A. Pifferi, A. Torricelli, and R. Cubeddu, "Determination of VIS-NIR absorption coefficients of mammalian fat, with time- and spatially resolved diffuse reflectance and transmission spectroscopy," in *BOS Annual Biomedical Topical Meeting* (2004).
68. S. Prahl, "Optical Absorption of Hemoglobin," <http://omlc.org/spectra/hemoglobin/>.
69. R. C. Mesquita and A. G. Yodh, "Diffuse optics: Fundamentals and tissue applications," in *Proceedings of the International School of Physics "Enrico Fermi"* (2011), pp. 51–74.
70. S. L. Jacques, "Optical Properties of Biological Tissues: A Review," *Phys. Med. Biol.* **58**, R37–61 (2013).
71. R. C. Haskell, L. O. Svaasand, T.-T. Tsay, T.-C. Feng, M. S. McAdams, and B. J. Tromberg, "Boundary conditions for the diffusion equation in radiative transfer," *J. Opt. Soc. Am. A* **11**, 2727–2741 (1994).
72. S. R. Arridge, M. Schweiger, M. Hiraoka, and D. T. Delpy, "A finite element approach for modeling photon transport in tissue," *Med. Phys.* **20**, 299–309 (1993).

73. M. Burcin Unlu, O. Birgul, R. Shafiha, G. Gulsen, and O. Nalcioglu, "Diffuse optical tomographic reconstruction using multifrequency data.," *J. Biomed. Opt.* **11**, 054008 (2006).
74. M. Schweiger, S. R. Arridge, M. Hiraoka, and D. T. Delpy, "The finite element method for the propagation of light in scattering media: Boundary and source conditions," *Med. Phys.* **22**, 1779–1792 (1995).
75. W. G. Egan and T. W. Hilgeman, *Optical Properties of Inhomogeneous Materials* (Elsevier, 1979).
76. H. Erkol, F. Nouizi, M. B. Unlu, and G. Gulsen, "An extended analytical approach for diffuse optical imaging," *Phys. Med. Biol.* **60**, 5103–5121 (2015).
77. M. S. Patterson, S. J. Madsen, J. D. Moulton, and B. C. Wilson, "Diffusion equation representation of photon migration in tissue," 1991 IEEE MTT-S Int. Microw. Symp. Dig. 905–908 (1991).
78. M. Schweiger, S. R. Arridge, and D. T. Delpy, "Application of the finite-element method for the forward and inverse models in optical tomography," *J. Math. Imaging Vis.* **3**, 263–283 (1993).
79. J. M. Schmitt, G. X. Zhou, E. C. Walker, and R. T. Wall, "Multilayer model of photon diffusion in skin," *J. Opt. Soc. Am. A* **7**, 2141–2153 (1990).
80. D. A. Boas, M. A. O’Leary, B. Chance, and A. G. Yodh, "Scattering of Diffuse Photon Density Waves by Spherical Inhomogeneities Within Turbid Media - Analytic Solution and Applications," *Proc. Natl. Acad. Sci. Med. Sci.* **91**, 4887–4891 (1994).
81. S. a Walker, D. a Boas, and E. Gratton, "Photon density waves scattered from cylindrical inhomogeneities: theory and experiments.," *Appl. Opt.* **37**, 1935–44 (1998).
82. B. W. Pogue and M. S. Patterson, "Frequency-domain optical absorption spectroscopy of finite tissue volumes using diffusion theory," *Phys. Med. Biol.* **39**, 1157–1180 (1994).
83. D. Contini, F. Martelli, and G. Zaccanti, "Photon migration through a turbid slab described by a model based on diffusion approximation. I. Theory," *Appl. Opt.* **36**, 4587–4599 (1997).
84. A. Kienle and M. S. Patterson, "Improved solutions of the steady-state and the time-resolved diffusion equations for reflectance from a semi-infinite turbid medium," *J. Opt. Soc. Am. A* **14**, 246–254 (1997).
85. F. Martelli, A. Sassaroli, Y. Yamada, and G. Zaccanti, "Analytical approximate solutions of the time-domain diffusion equation in layered slabs.," *J. Opt. Soc. Am. A. Opt. Image Sci. Vis.* **19**, 71–80 (2002).

86. A. Kienle, "Light diffusion through a turbid parallelepiped.," J. Opt. Soc. Am. A. Opt. Image Sci. Vis. **22**, 1883–1888 (2005).
87. A. Liemert and A. Kienle, "Light diffusion in a turbid cylinder. I. Homogeneous case.," Opt. Express **18**, 9456–9473 (2010).
88. D. A. Boas, J. P. Culver, J. J. Stott, A. K. Dunn, M. J. Holboke, B. J. Tromberg, X. Li, N. Shah, J. Fishkin, D. Kidney, J. Butler, B. Chance, A. G. Yodh, D. A. Benaron, S. R. Hintz, A. Villringer, D. Boas, A. Kleinschmidt, J. Frahm, C. Hirth, H. Obrig, J. C. Van Houten, E. L. Kermit, W. F. Cheong, D. K. Stevenson, A. M. Siegel, and A. Zourabian, "Three dimensional Monte Carlo code for photon migration through complex heterogeneous media including the adult human head," J Biomed OptTissue Opt. Sci. J. Neurotrauma Opt. EXPRESS **10**, 159–170 (2002).
89. S. A. Prahl, M. Keijzer, S. L. Jacques, and A. J. Welch, "Monte-Carlo model of light propagation in tissue," SPIE Inst. Ser. **5**, 102–111 (1989).
90. L. Wang, S. L. Jacques, and L. Zheng, "MCML - Monte Carlo modeling of light transport in multi-layered tissues," Comput. Methods Programs Biomed. **47**, 131–146 (1995).
91. F. Nouzi, "Preclinical, fluorescence and diffuse optical tomography: non-contact instrumentation, modeling and time-resolved 3D reconstruction," University of Strasbourg, France (2011).
92. I. J. Bigio and S. Fantini, *Quantitative Biomedical Optics: Theory, Methods, and Applications* (2016).
93. D. W. Marquardt, "An Algorithm for Least-Squares Estimation of Nonlinear Parameters," J. Soc. Ind. Appl. Math. **11**, 431–441 (1963).
94. K. Levenberg, "A method for the solution of certain non-linear problems in least squares," Q. Appl. Math. **2**, 164–168 (1944).
95. H. Dehghani, D. C. Barber, and I. Basarab-Horwath, "Incorporating a priori anatomical information into image reconstruction in electrical impedance tomography.," Physiol. Meas. **20**, 87–102 (1999).
96. A. N. Tikhonov, "Regularization of incorrectly posed problems," Sov. Math. Dokl. **4**, 1624–1627 (1963).
97. K. D. Paulsen and H. Jiang, "Spatially varying optical property reconstruction using a finite element diffusion equation approximation," Med. Phys. **22**, 691–701 (1995).
98. S. Srinivasan, B. W. Pogue, H. Dehghani, S. Jiang, X. Song, and K. D. Paulsen, "Improved quantification of small objects in near-infrared diffuse optical tomography.," J. Biomed. Opt. **9**, 1161–71 (2004).

99. P. K. Yalavarthy, B. W. Pogue, H. Dehghani, and K. D. Paulsen, "Weight-matrix structured regularization provides optimal generalized least-squares estimate in diffuse optical tomography," *Med. Phys.* **34**, 2085 (2007).
100. P. K. Yalavarthy, B. W. Pogue, H. Dehghani, C. M. Carpenter, S. Jiang, and K. D. Paulsen, "Structural information within regularization matrices improves near infrared diffuse optical tomography.," *Opt. Express* **15**, 8043–58 (2007).
101. S. R. Arridge and M. Schweiger, "Photon-measurement density functions. Part 2 : Finite-element-method calculations," *Appl. Opt.* **34**, 2683–2687 (1995).
102. F. Nouizi, M. Torregrossa, R. Chabrier, and P. Poulet, "Improvement of absorption and scattering discrimination by selection of sensitive points on temporal profile in diffuse optical tomography," *Opt. Express* **19**, 12843–12854 (2011).
103. Jessica Kwong, F. Nouizi, J. Cho, J. Zheng, Y. Li, J. Chen, M.-Y. Su, and G. Gulsen, "Breast density quantification using structured-light based diffuse optical tomography simulations," *Appl. Opt.* (2016). (*Submitted*)
104. S. Srinivasan, B. W. Pogue, S. Jiang, H. Dehghani, C. Kogel, S. Soho, J. J. Gibson, T. D. Tosteson, S. P. Poplack, and K. D. Paulsen, "Interpreting hemoglobin and water concentration, oxygen saturation, and scattering measured in vivo by near-infrared breast tomography.," *Proc. Natl. Acad. Sci. U. S. A.* **100**, 12349–54 (2003).
105. K. E. Michaelsen, V. Krishnaswamy, A. Shenoy, E. Jordan, B. W. Pogue, and K. D. Paulsen, "Anthropomorphic breast phantoms with physiological water, lipid, and hemoglobin content for near-infrared spectral tomography.," *J. Biomed. Opt.* **19**, 26012 (2014).
106. R. Cubuk, N. Tasali, B. Narin, F. Keskiner, L. Celik, and S. Guney, "Correlation between breast density in mammography and background enhancement in MR mammography," *Radiol med* **115**, 434–441 (2010).
107. J. R. Weber, D. J. Cuccia, W. R. Johnson, G. H. Bearman, A. J. Durkin, M. Hsu, A. Lin, D. K. Binder, D. Wilson, and B. J. Tromberg, "Multispectral imaging of tissue absorption and scattering using spatial frequency domain imaging and a computed-tomography imaging spectrometer.," *J. Biomed. Opt.* **16**, 011015 (2011).
108. A. Mazhar, S. Dell, D. J. Cuccia, S. Gioux, A. J. Durkin, J. V Frangioni, and B. J. Tromberg, "Wavelength optimization for rapid chromophore mapping using spatial frequency domain imaging.," *J. Biomed. Opt.* **15**, 061716 (2010).
109. D. Thayer, M. B. Unlu, Y. Lin, K. Yan, O. Nalcioglu, and G. Gulsen, "Dual-contrast dynamic MRI-DOT for small animal imaging," *Technol. Cancer Res. Treat.* **9**, 61–70 (2010).
110. S. A. Carp, T. Kauffman, Q. Fang, E. Rafferty, R. Moore, D. Kopans, and D. Boas, "Compression-induced changes in the physiological state of the breast as observed

through frequency domain photon migration measurements," *J. Biomed. Opt.* **11**, 064016 (2006).

111. Y. Lin, H. Gao, O. Nalcioglu, and G. Gulsen, "Fluorescence diffuse optical tomography with functional and anatomical a priori information: feasibility study," *Phys. Med. Biol.* **52**, 5569–5585 (2007).
112. N. Kosaka, M. Ogawa, P. P. L. Choyke, and H. Kobayashi, "Clinical implications of near-infrared fluorescence imaging in cancer," *Futur. Oncol.* **5**, 1501–1511 (2009).
113. L. E. Kelderhouse, V. Chelvam, C. Wayua, S. Mahalingam, S. Poh, S. A. Kularatne, and P. S. Low, "Development of tumor-targeted near infrared probes for fluorescence guided surgery," *Bioconjug. Chem.* **24**, 1075–1080 (2013).